SUPER RESOLUTION MEASUREMENT OF FLUORESCENT DIPOLES VIA LINEAR DICHROISM

A Dissertation
Presented to
The Academic Faculty

by

Hao Zhang

In Partial Fulfillment
of the Requirements for the Degree
Ph.D. in the
Biomedical Engineering Department

Georgia Institute of Technology
Emory University
Peking University
August 2017

SUPER RESOLUTION MEASUREMENT OF FLUORESCENT DIPOLES VIA LINEAR DICHROISM

Approved by:

Dr. Peng Xi, Advisor
School of Biomedical Engineering
Peking University

Dr. Changhui Li
School of Biomedical Engineering
Georgia Institute of Technology

Dr. Cheng Zhu, Co-advisor
School of Biomedical Engineering
Georgia Institute of Technology

Dr. Juntao Gao
School of TNLIST
Tsinghua University

Dr. Tianyu Xie
School of Biomedical Engineering
Peking University

Date Approved: June 7, 2017

ACKNOWLEDGEMENTS

I would like to thank all the advisors, lab mates, collaborators and those who helped me during the five years of graduate studying. As my main advisor, Dr. Peng Xi cares much about my study and my life. At the very beginning of my experiments, Dr. Xi taught me the required basic skills. During the research, he encouraged me to keep on my research plan and provided me with as much support as he can. My main project, super resolution fluorescence polarization microscopy, is also supervised by two other PIs, Dr. Juntao Gao from Tsinghua University and Dr. Dayong Jin from Sydney University. I learned not only knowledge of other fields but also the skills to do research from them. As a student of the joint Ph.D. program of PKU/GT/Emory, I also spent one year studying in my second campus, Georgia Tech in Atlanta. I joined Dr. Cheng Zhu's lab during the year. Dr. Cheng Zhu designed a joint research plan with me and supported me for the experiments. He also provided valuable suggestions for my life in the United States. It is the luckiest thing to meet with so many great advisors and I want to express my gratitude to them.

Besides, I want to thank my cooperators in the SDOM experiment. As a senior lab member, Mr. Xusan Yang helped with the system setup and generously offered his help to me continuously. Miss Miaoyan Wang helped with the biological experiments; Mr. Long Chen helped with the mathematical problems; Mrs. Shujuan Ge and Mrs. Chunfeng Song helped with the preparation of biological sample. I want also thank Mr. Qian Su and Miss Rongqin Li for the help on the single molecule imaging experiments.

I would like to thank my committee members Dr. Changhui Li, Dr. Tianyu Xie and other PIs who gave me valuable advices on my research, including Dr. Yujie Sun, Dr. Kuangshi Cheng, Dr. Liangyi Chen and Dr. Pingyong Xu.

I would like to thank my lab mates Hao Xie, Zhiping Zeng, Amit Lal, Kun Zhao, Zhaoyang Wu and Meiqi Li. I really enjoyed the life together with them.

The last but not the least, I would like to thank my parents and my fiancée Jeiyou Chen. Jieyou Chen and I would get married in this summer. The summer in 2017 is not only the graduation of my graduate study but also our love. I am grateful for the joys brought by she. My parents keep supporting me with my research and caring for my happiness and healthiness. I wouldn’t have completed my degree without them.

Finally, I would like to thank everyone who come to my life who has supported and helped me to be what I am today. Thank you!

TABLE OF CONTENTS

LIST OF TABLES

LIST OF FIGURES

LIST OF SYMBOLS AND ABBREVIATIONS

AOTF	Acoustic-Optic Tunable Filter
DOPI	Defocused Orientation and Position Imaging
DPR	Defocused Pattern Recognition
EMCCD	Electron-Multiplying Charge Coupled Device
FA	Fluorescence Anisotropy
FCCS	Fluorescence Cross-Correlation Microscopy
FCS	Fluorescence Correlation Microscopy
FISTA	Fast Iterative Shrinkage Thresholding Algorithm
FPM	Fluorescence Polarization Microscopy
FRAP	Fluorescence Recovery After Photobleaching
FRET	Forster Resonance Energy Transfer
FWHM	Full Width at Half Maximum
GFP	Green Fluorescence Protein
HWP	Half Wave Plate
LC	Liquid Crystal
LD	Linear Dichroism

LFM	Light Field Microscopy
MAP	Maximum A Posteriori
N.A.	Numeric Aperture
OLID	Optical Lock-In Detection
OUF	Orientation Uniform Factor
PALM	PhotoActivated Localization Microscopy
PolScope	Polarization Microscope
PSF	Point Spread Function
sCMOS	scientific Complementary Metal-Oxide-Semiconductor Transistor
SDOM	Super-resolution Dipole Orientation Mapping
SIM	Structured Illumination Microscopy
SLB	Supported Lipid Bilayer
SLIDOM	Super-resolution Lock-In Dipole Orientation Mapping
SPoD	Super-resolution Polarization Demodulation microscopy
STED	STimulated Emission Depletion
STORM	STochastic Optical Reconstruction Microscopy
TIRFM	Total Internal Reflection Fluorescence Microscopy

SUMMARY

Because of its specific labeling and high imaging contrast, fluorescent microscopy has played a more and more important role in imaging sub-cellular organelles. Fluorescence contains four attributes: intensity (labeling density), wavelength (absorption and emission spectrum), time (fluorescence lifetime), and polarization (related to fluorescent dipoles). Fluorescence polarization could measure the dipole orientation of fluorophores from the absorption (linear dichroism) or the emission (fluorescence anisotropy) of fluorophores. Since the orientation of fluorescent dipoles is related to the structure of labeled samples, fluorescent polarization microscopy has been applied extensively. Whereas similar to other optical imaging methods, fluorescence polarization microscopy is barricaded by the diffraction limit.

Super resolution fluorescence microscopy is able to achieve sub-diffraction resolution, whose key lies in the modulation of the fluorescence intensity. Such modulation could be either in a structured illumination manner, for example, STimulated Emission Depletion (STED) or Structured Illumination Microscopy (SIM); or in a stochastic blinking/fluctuation manner, for example, PhotoActivated Localization Microscopy (PALM)/STochastic Optical Reconstruction Microscopy (STORM). In this dissertation, the intensity modulation is based on the linear dichroism of fluorophores. Applying super resolution technique to fluorescence polarization microscopy, both the intensity and the orientation of fluorescent dipoles could be measured in super resolution. Optical lock-in is implemented to further improve the detection of polarization modulation, 3D super resolution imaging has also been realized by z-scanning of the sample.

The main contents of the dissertation are as follows:

Chapter 1 includes the introduction of the research background. Fluorescence polarization of fluorophores is firstly introduced, including the absorption and emission characteristics. Then, three different fluorescence polarization microscopy is introduced: Defocused Patter Recognition, Fluorescence Anisotropy, and Linear Dichroism. After that, various super resolution fluorescence imaging techniques are discussed as well as the application in fluorescence polarization microscopy.

Chapter 2 introduces the principle of super resolution dipole orientation mapping (SDOM), together with its system setup and reconstruction algorithm. SDOM is compared to a similar technique (SPoD) and is verified by simulation, imaging samples of fluorescent beads, fixed cells and live cells.

Chapter 3 contains further improvements of SDOM. The first section includes the application of optical lock in on SDOM. Thanks to the natural periodical intensity modulation of SDOM, optical lock in could be used for signal detection, which greatly improves the signal-to-noise ratio and increases the imaging resolution. The second section extended SDOM to 3D super resolution imaging, by z-scanning of the sample.

Chapter 4 includes my other research during graduate. The first section is about light field microscopy. Two different setups are applied to fast volumetric imaging of neuronal activities and to 3D single molecule localization respectively. The second section is to use complementary optical imaging methods to study binding kinetics of proteins on the cell membrane, including biological specimen preparation, Fluorescence Recovery After Photobleaching (FRAP), and Fluorescence Correlation Spectroscopy (FCS).

Chapter 5 is the discussion and conclusion of the dissertation.

CHAPTER 1. INTRODUCTION

Light is a kind of electromagnetic waves which are described as transverse waves. Transverse waves have their polarizations. Natural light from many sources, such as sun, flames and incandescent lamps are unpolarized light. Reflected sunlight from the surface of a lake is partially polarized because of Brewster's law, or polarized light can also be produced by passing unpolarized light through a polarizing filter. Most common optical materials (such as glass) are isotropic and do not affect the polarization of light passing through them. However, some materials, those that exhibit birefringence, dichroism, etc., can change the polarization of light, some of which could be used to make polarizing filters. Light is said to be partially polarized when there is more power in one polarization mode than another. At any particular wavelength, partially polarized light can be statistically described as the superposition of a completely unpolarized component and a completely polarized one. There are several types of polarized light, including linear polarization, circular polarization, and elliptical polarization.

When the electric field vector of a light is confined in one plane which is perpendicular to the direction of propagation, the light would be said as linear polarized. The orientation of a linear polarization is defined by the direction of the electric field vector. Any combination of two or more linearly polarized light will still lead to a polarized light when the phase of the polarization remains the same. However, when a phase shift is introduced, one would generally obtain elliptical polarization in most cases or circular polarization under specific conditions. A pair of orthogonal polarization states could be used for basic functions and to describe any type of polarization. Besides linear polarization, right and left circular polarization could also be taken as basic functions and may simplify the solution of problems in some cases.

Fluorescence (but not lasers) generally produce light described as incoherent and unpolarized, because radiation is produced independently by a large number of atoms or molecules whose emissions are uncorrelated and generally of random polarizations. However, it implies that the polarization changes so quickly in time that it will not be measured or relevant to the outcome of an experiment. What’s the situation when single chromophores or uniformly distributed chromophores are taken?

1.1 FLUORESCENCE POLARIZATION OF CHROMOPHORES

Fluorescent microscopes could provide specific labeling and high contrast, which plays an important role in visualizing cellular and subcellular structures. The fundamental physical dimensions of fluorescence include intensity (which reflects the fluorescence concentration), wavelength (absorption and emission spectrum), time (fluorescence decay lifetime) and polarization. To study the polarization of the fluorescence, we should better start from the polarization of single chromophores or uniformly distributed chromophores.

Optical properties of most chromophores are anisotropic, with transition moments along a specific direction in the molecular structure. Fluorescent dipoles could be used to model excitation absorption or fluorescence emission of chromophores, which may differ in some cases. When excited by polarized light, the dipoles with their orientations aligned parallel to the electric vector of the polarized excitation would have the highest probability of absorption. The distribution of absorption probability on polarized excitation is proportional to $\cos^2\theta$, where θ is the intersecting angle between absorption dipole orientation and polarization direction. Two-photon absorption is described by an absorptivity tensor, and effects of molecular orientation are generally complex[1,2]. The emitted fluorescence from dipoles is also polarized, with the highest intensity component of polarization along the emission dipole orientation. The distribution of intensity probability on emission polarization is proportional to $\cos^2\theta'$, where θ' is the intersecting angle between emission dipole orientation and the polarization direction of the polarized component of emitted fluorescence. According to the anisotropy in fluorescent absorption or emission, the dipole orientations of chromophores could be measured. In real condition, the linker between fluorescent probes and the structure attached is not absolutely firm, which makes the dipoles wobbling at a speed much faster than the imaging speed. Thus, the real fluorescent dipoles are modeled with average azimuth and wobbling angle in many types of research[3-5].

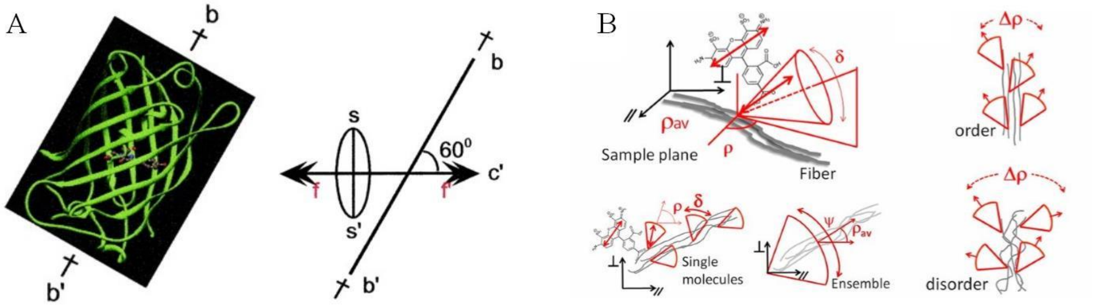

Figure 1 – Schematic illustration of fluorescent dipoles.
(A) Structure of Green Fluorescence Protein (GFP) molecule based on X-ray crystallographic analysis (left) and its schematic structure with f-f' (c-c') referring fluorescent dipoles. (B) Fluorescent dipoles labeled on bio-structures (here, Alexa Fluor 488 labeled on actin, upper-left). Each molecule has its own average orientation and wobbling angle, while the ensemble behaviors a different property (lower-left).

The statistics about neighboring dipoles reflect order or disorder of the system. Figures adapted from [3,6].

Early research suffers from limitations because the observation volume usually addresses a bundle of chromophores. In this case indeed, the description of the system cannot be given by a single orientation value and needs to introduce a geometrical model and a complete set of parameters, for instance, the average orientation for the fluorophores and the width of the orientation distribution of the ensemble. Hence, it is limited to chromophore in solution or uniformly distributed samples for FA measurement.

1.1.1 Fluorescence Anisotropy

Fluorescence anisotropy is a type of early research started from the 1950s, which aims at studying the fluorescence polarization of samples consisting of organized chromophores. A typical setup of fluorescence anisotropy is to detect the p and s component of emitted fluorescence, which could be achieved by a polarizer, a polarization beam splitter (PBS) or a Wollaston Prism.

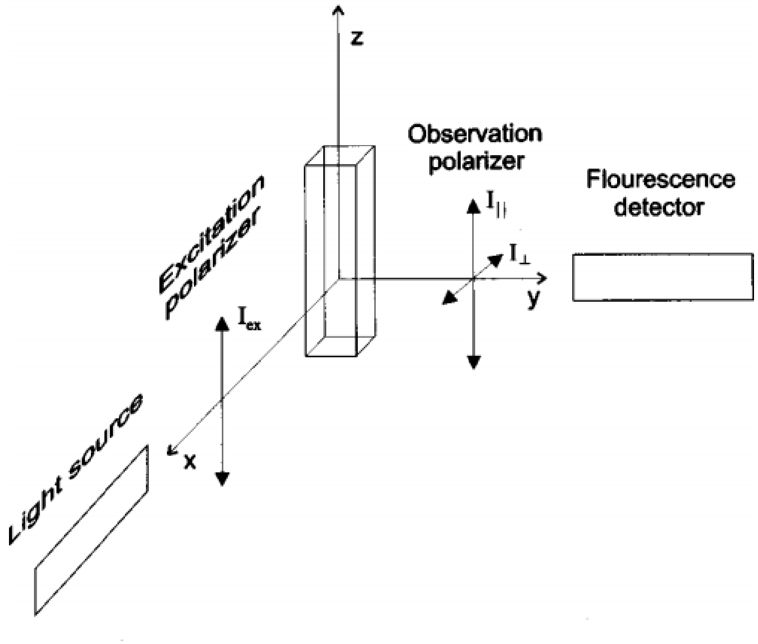

Figure 2 – Schematic diagram for measurement of fluorescence anisotropies. The sample is excited by a linearly polarized light source with the direction along the z-axis. The detector is placed on y-axis with parallel polarization and perpendicular polarization of the fluorescence detected separately. Figures adapted from [7].

When excited by polarized light, the sample consisting of uniform chromophores would emit anisotropic fluorescence, which could be analyzed as the result of three independent sources of polarized light along three perpendicular axes x, y, z (Figure 2). The intensities along these axes could be defined as: I_x , I_y and I_z. The intensity of the emission is measured through a polarizer, which is either oriented parallel ($||$, the observed intensity as $I_{||}$) or perpendicular ($\perp$, the observed intensity as $I_{\perp}$) to the direction of the polarized excitation. The fluorescence anisotropy is proportional to the intensity different $I_{||} - I_{\perp}$. To get rid of the influence of the sample intensity, fluorescence anisotropy is normalized by the total intensity of fluorescence, which is $I_T = I_x + I_y + I_z = I_{||} + 2I_{\perp}$. The definition of fluorescence anisotropy r is:

$$r = \frac{I_{\parallel} - I_{\perp}}{I_{\parallel} + 2I_{\perp}} \qquad \textbf{Eq. 1}$$

Sometimes the fluorescence anisotropy is also described by the term polarization ratio p, which is defined by:

$$r = \frac{I_{\parallel} - I_{\perp}}{I_{\parallel} + I_{\perp}} \qquad \textbf{Eq. 2}$$

The polarization and anisotropy contain the same information and their values can be interchanged using:

$$p = \frac{3r}{2+r}$$

$$r = \frac{2p}{3-p} \qquad \textbf{Eq. 3}$$

1.1.2 Factors Affecting Fluorescence Anisotropy

The emitted fluorescence could be depolarized by a number of processes, during which the fluorophore motion is one of the most important factors, especially rotational diffusion[8]. Rotational diffusion changes the direction of the transition moments. If the excited fluorophore rotates during its excited-state lifetime, the emitted fluorescence is depolarized. The favored orientation of emitting molecules at time zero is affected by the rotational motions. This happens when the fluorescence lifetime τ_f is longer than the rotational correlation time τ_{rot}. For instance, a protein with a molecular weight of 25 kD can be expected to have a rotational correlation time near 10 ns, which is comparable to the lifetime of many fluorophores. In this case, after absorption of a photon, the molecule has enough time to rotate before its fluorescence emission. Therefore, the absorption and emission orientations are uncorrelated, and the polarization information is lost. The relation between the rotational correlation time τ_{rot}, fluorescence lifetime τ_f, the fundamental anisotropy r_0 and measured anisotropy r is described by the Perrin equation:

$$\frac{1}{r} = \frac{1}{r_0}(1 + \frac{\tau_f}{\tau_{rot}}) \qquad \textbf{Eq. 4}$$

Since the rate of rotational diffusion depends on the viscosity of the solvent, the size and shape of the rotating molecules, and temperature. The rotational rate of fluorophores in solution is dependent upon the viscous drag imposed by the solvent. For biomolecules, the anisotropy is decreased due to both rotational diffusion and internal flexibility. As examples, fluorescence anisotropy measurements have been used to quantify protein denaturation, which usually results in increased flexibility of the peptide backbone, and protein association with other macromolecules, which changes the overall rate of rotation.

Besides molecular motion, Förster Resonance Energy Transfer (FRET) would affect fluorescence anisotropy as well. FRET describes energy transfer between two chromophores: one donor chromophore, initially in its electronic excited state, may transfer energy to an acceptor chromophore through the non-radiative dipole-dipole coupling. The efficiency of this energy transfer is inversely proportional to the sixth power of the distance between donor and acceptor, which makes FRET extremely sensitive to small changes in distance. Since the additional angular displacement of the absorption transition moment and emission transition moment, FRET between fluorophores would decrease the fluorescence anisotropy of fluorescence. The effects of rotational diffusion and energy transfer are easily separated by selection of the experimental conditions. For example, rotational diffusion is more sensitive to solution viscosity and temperature, which could be negligible in less viscose solutions and low temperature, while FRET only occurs in concentrated solution where the average distance between the fluorophore molecules is comparable to a characteristic distance called Förster distance R_0 .

Attention needs to be paid to the factor that, previously mentioned “fluorescence anisotropy” and the Perrin equation (Eq. 4) are used to describe samples of homogeneous fluorophores, either in solution or crystals. When it comes single chromophores, things become quite different. To avoid misunderstanding, the term “fluorescence polarization” is used to describe single chromophores instead of the term “fluorescence anisotropy”, which would be discussed in context below.

1.2 FLUORESCENCE POLARIZATION MICROSCOPY (FPM)

Based on its great analytical power, the polarized light microscope has found numerous applications in fields such as biology, mineralogy, metallography, chemistry and for forensic studies. In biology, the polarized light microscope has the unique potential to measure submicroscopic molecular organization dynamically and non-destructively in samples that, in general, can be kept in native environmental conditions.

There are mainly three categories of methods to measure the fluorescence polarization of chromophores. The first two are utilizations of the polarized absorption and emission of fluorescence, which are named linear dichroism (LD) and fluorescence anisotropy (FA) accordingly. Here, the same term of “fluorescence anisotropy” is used because both of them are based on the principle of polarized fluorescence emission. The third method is to determine dipole orientation of chromophores according to their diffraction pattern in a high numerical aperture (N.A.) imaging system, which is termed as defocused pattern recognition (DPR) in the thesis. This is because the diffraction pattern of dipoles would appear much more different when they are more defocused in several hundred nanometers. According to the difference of the measuring principle, Fluorescence Polarization Microscopy (FPM) could be categorized accordingly.

1.2.1 Diffraction Pattern Recognition Method

The emission of a fluorescent dipole is anisotropic, which would bring differences in acquired image after collected by the objective. The intensity distribution of the blurred image contains information about the molecule’s emission-dipole orientation. The defocusing method (referred as DPR in this thesis) was firstly proposed in 1997 by Sepiol et al. and experimentally demonstrated for an immersion mirror objective used for imaging within a cryostat at low temperature[9]. The orientation could be retrieved from the asymmetric image via pattern analysis or pattern recognition. The orientational information within the defocused pattern is not only limited to in plane angle but also out-of-focus tilting angle[10]. In 2003, Bohmer et al. applied the concept to image surface-bound molecules using a conventional CCD-imaging epi-fluorescence wide field microscope with laser illumination[11] and later a pattern recognition algorithm under noisy low-signal conditions was developed[12].

The principle of the DPR method is as follows. Fluorescent molecules are taken as ideal electric dipole emitters. When placed within a dielectrically homogeneous environment, the dipoles exhibit the classical angular distribution of radiation proportional to $\sin^2\theta$, where θ is the angle between the direction of observation and the dipole's axis. When the dipole is placed close to an interface separating two media with different refractive indices, the angular distribution of radiation changes dramatically due to self-interaction of the emitting dipole with its back-reflected electromagnetic field. The final defocused pattern could be given by the vector diffraction theory and validated by the experiments.

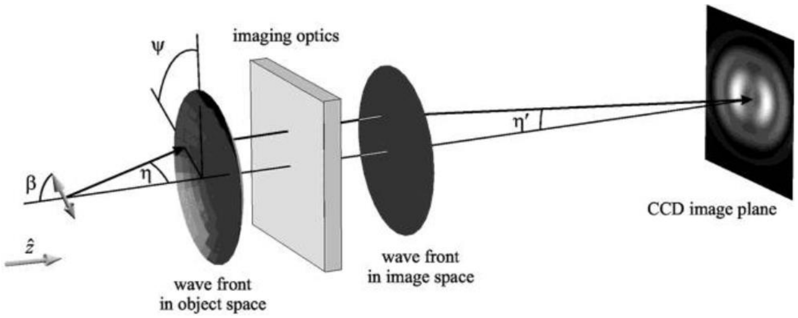

Figure 3 – General geometry of defocused imaging.
Figure adapted from [12].

In 2006, Toprak et al. developed defocused orientation and position imaging (DOPI) by combining DRP with single molecular tracking[13]. 3D orientation and stepping behavior of myosin V was measured as myosin V moves along actin. The myosin V is labeled with single functional rhodamine probes attached to one of the calmodulins of the light-chain domain (LCD). The fact was uncovered that the probe angle relative to the barbed end of the actin averaged 128° while LCD was in the leading state and 57° in the trailing state.

The angular difference of 71° represents the rotation of LCD around the bound motor domain and is accompanied with a 37-nm forward step size of myosin V.

1.2.2 Fluorescence Anisotropy Method

Early fluorescence anisotropy based FPM (FA-FPM) is similar to the fluorescence anisotropy analysis of samples, with analyzers of detect orthogonal polarized fluorescence. A typical FA setup consists of linearly polarized excitation and two polarized detections of fluorescence, which are parallel or perpendicular to the direction of the polarized excitation. The parallel and perpendicular detection could be achieved sequentially by changing analyzers in the emission path or simultaneously by polarization beam splitter (PBS)[14], a Wollaston prism[3] or a Thompson prism[15]. The anisotropy and azimuth could be calculated through two relating pixels. Early FA research started from studying the fluorescence polarization of chromophores in solutions[16], which didn't include an objective to collimate the fluorescence. An objective would greatly improve collected signals but may influence the fluorescence polarization when numeric aperture (N.A.) is high. A general theory for epi-illumination observation of FA through high N.A. objectives was presented by Axelrod in 1979[17] and was applied to measure diI – a kind of membrane probes – on erythrocyte ghosts. FA was later implemented with total internal reflection fluorescence microscopy (TIRFM)[18], fluorescence recovery after photobleaching (FRAP)[19], etc. Four detection channels could enable 3D orientation detection of fluorescent dipoles instead of only in-plane measurement[20] or could provide an unbiased measurement of dipole orientations[21].

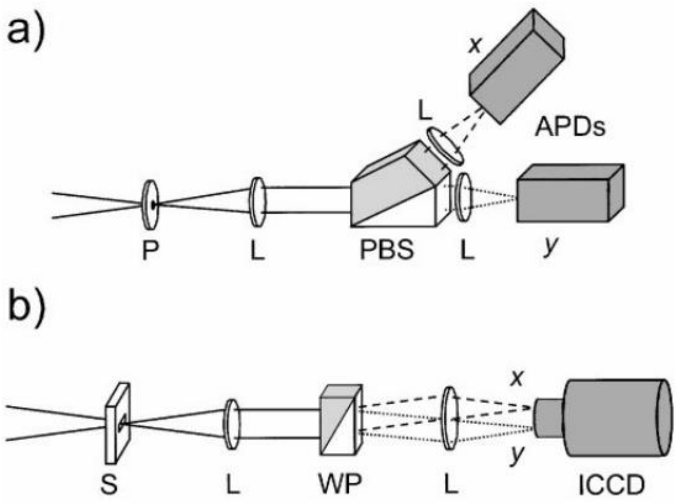

Figure 4 – Fluorescence Anisotropy detection schemes.
(a) Emitted fluorescence is resolved into its two orthogonal components with a polarizing beam splitter and focused onto two separate detectors (photodiodes, APDs). (b) Emitted fluorescence is split by a Wollaston prism and imaged onto two halves of the detector area of a CCD camera. Figure adapted from [15].

When polarization is quantitatively analyzed, a coordinate system frequently used relates to the plane of incidence. This is the plane made by the incoming propagation direction and the vector perpendicular to the plane of an interface, in other words, the plane in which the ray travels before and after reflection or refraction. The component of the electric field parallel to this plane is termed p-like (parallel) and the component perpendicular to this plane is termed s-like. Hence, the parallel polarization component and the perpendicular polarization component are also termed as p-light and s-light respectively.

1.2.3 Linear Dichroism

Linear dichroism was firstly applied to the polarized microscope, which was much earlier than its application on fluorescence polarization microscope. One of the most famous setups is PolScope, which was designed to overcome the limitations of the traditional polarized microscope by switching different polarizers. In PolScope developed by Oldenburg et al. in 1995[22,23], a precision universal compensator made of two liquid crystal variable retarders was incorporated. The two variable retarders are computer controlled and replace the traditional compensator, which could provide fast measurements of specimen anisotropy at all points of the image constituting the field of view.

Though PolScope isn't for measurement of fluorescence polarization, the design of a precision universal compensator consisting of two liquid crystal variable retarders and a polarizer is also important for FPM, including both linear dichroism and fluorescence anisotropy. The LD-FPM is categorized based their incorporation with different types of microscopes and introduced as follows.

1.2.3.1 Wide Field based LD microscopy

Excitation polarization is easy to understand in epi-illumination of wide field microscope[24-26]. In 2006, Vrabioiu et al. applied linear dichroism to an epi-illumination wide field fluorescent microscope by inserting two different polarizers sequentially into the excitation beam[27]. With the compact setup, important facts were revealed that the septin filaments rotate through 90° in the membrane plane during the cell division process, which has great significance in the study of septin filament organization and dynamics in living yeasts. As mentioned before, the method of recording the polarized fluorescence required the step-by-step rotation and image acquisitions of the sample located between fixed, parallel polarizers. Subsequently, the images were registered by hand and analyzed for fluorescence anisotropy. The slow nature of the image acquisition and analysis method limited its application to relatively static processes and a limited number of cells.

The development of FluoPolScope continued this work[28,29]. A global compensator of liquid crystal variable retarders was used to rapidly and comprehensively record the quasi-static patterns of anisotropy due to the binding of fluorophores to a molecular scaffold that remains static over a timescale of seconds, but might dynamically remodel over minutes and longer. For optimizing the efficiency, the excitation light used trans-illumination without a polarization filter in the imaging path. The image arithmetic operations generate maps of anisotropy at a spatial resolution commensurate with the microscope optics used.

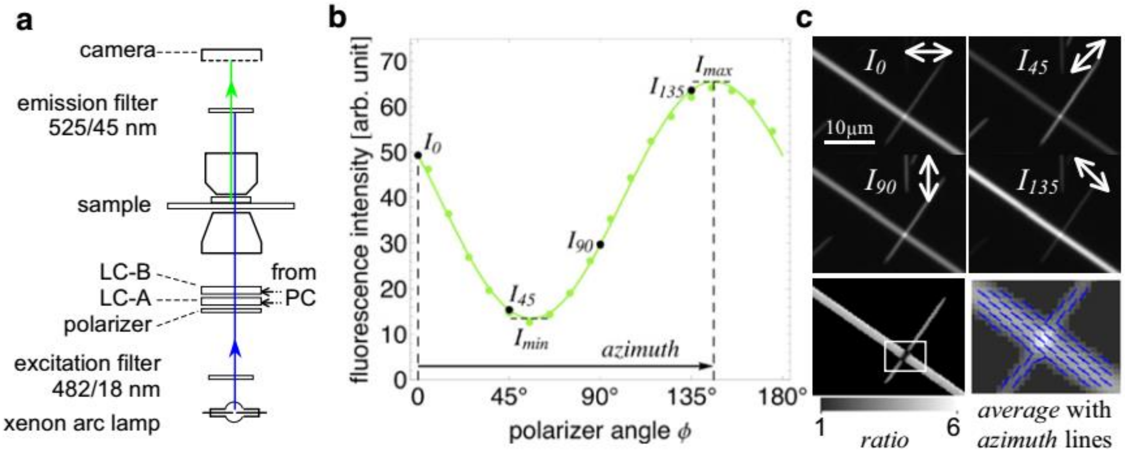

Figure 5 – Schematic of Fluorescence PolScope.
(a) Schematic setup of FluoPolScope. LC-A, LC-B, and the polarizer form the universal polarizer. (b) Graph of fluorescence intensity measured in an image point of a GFP crystal versus the angle of linear polarization of the excitation light. (c) The fluorescence intensity image of GFP crystal at different polarizations (upper panel) and polarization ratio and azimuth images (lower panel). Figure adapted from [29].

Each pixel of the image contains four polarization related values, which could be used to calculate the azimuth and polarization ratio as follows.

$$
\begin{gathered}
a = (I_0 - I_{90}), b = (I_{45} - I_{135}), c = (I_0 + I_{45} + I_{90} + I_{135}), \\
anisotropy = \frac{\sqrt{a^2 + b^2}}{c}, ratio = \frac{I_{\max}}{I_{\min}} = \frac{1 + 2anisotropy}{1 - 2anisotropy}, \\
azimuth = \frac{1}{2}\arctan(\frac{b}{a}).
\end{gathered}
\qquad \textbf{Eq. 5}
$$

In 2015, FluoPolScope was combined with Multi-Focus imaging techniques with light field image. Simultaneously 3D imaging was achieved, together with dipole orientation measurement based LD[30].

In 2014, Hafi et al. developed super resolution by polarization demodulation (SPoD) with excitation polarization angle narrowing (ExPAN)[31]. In 2016, Zhanghao et al. extended the work of SPoD to super resolution dipole orientation mapping (SDOM), which achieved super-resolution in both fluorescence intensity and polarization. These techniques are all based on LD-FPM with super resolution imaging and will be discussed later.

1.2.3.2 Confocal Microscopy with Linear Dichroism

Linear Dichroism was also applied to Confocal and Two-Photon microscopy[2,4,5,32-35]. The polarization of the focal point of confocal illumination is linearly polarized in the plane if the excitation is polarized[5]. In the work, fluorescence polarization was studied in organized cells, such as spherical cells or cylindrical cells. The assumption was made that all the fluorophore moieties attached to the cell membrane were at a fixed angle θ with respect to the cell membrane or modeled as a Gaussian distribution with a mean of θ and a wobbling range $\Delta\theta$, to consider protein dynamics, conformational flexibility, and nanoscopic membrane roughness. The appearance of fluorescently labeled cells and the amount of observed different fluorescence polarization could be used to describe θ . When the wobbling range is relatively large, two-photon polarized excitation would remain high sensitivity over single-photon excitation since two-phone absorption rate is proportional to the cosine to the fourth power of the angle (in simple cases).

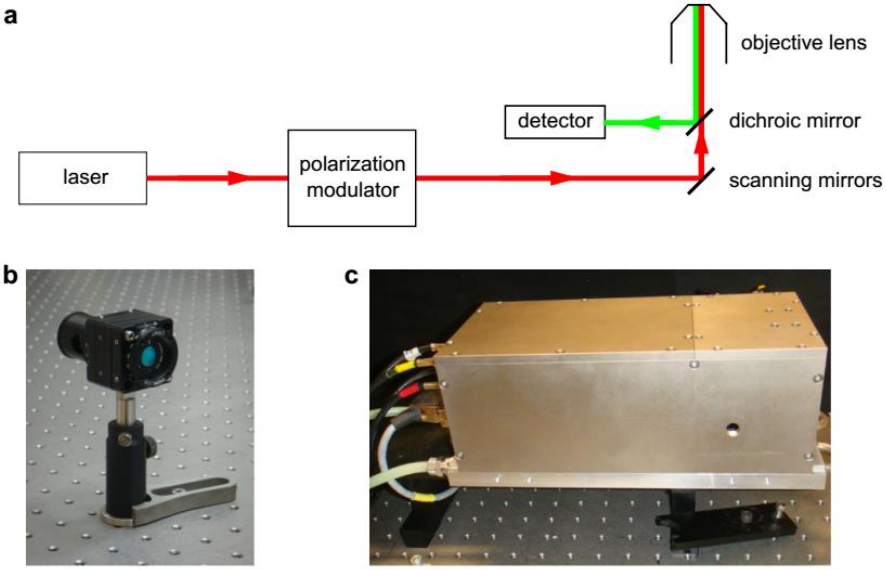

Figure 6 – Setup for two-photon polarization microscopy.
(a) Schematic diagram of a two-photon polarization microscope. (b) A simple polarization modulator composed of a Glan-laser polarization beam splitter and a manually rotatable half wave plate. (c) a rapid polarization modulator based on a Pockels cell, driven in synchrony with the scanning of the microscope. Figure adapted from [5].

Point-by-point scanning for image acquisition and mechanical control of the input polarization is highly time-consuming and, therefore, limited to static samples. To capture highly dynamic processes, Wang et al. developed high frame-rate fluorescence confocal angle-resolved microscopy[34]. A dramatic improvement of the acquisition speed of angle-resolved LD was achieved by a high-speed spinning disk confocal unit, allowing acquisition rates up to several hundred frames per second. In addition, fast switching of the polarization state is provided by an electro optical modulator placed in the excitation path. This technique could provide real-time monitoring of molecular order in dynamic specimens.

1.2.3.3 Linear Dichroism with TIRFM and Other Imaging Modality

LD with epi-illumination couldn’t provide axially polarized excitation, which, however, exists in TIRF illumination. Such design could be achieved by a rotary combination of a half wave plate and a prism[36], or polarization modulation with a Pockel cell via TIRF illumination, as in polTIRF setup[18,37,38].

Total Internal Reflection Fluorescence Microscopy (TIRFM) is an axial super resolution technique based on near field imaging. A TIRFM uses an evanescent wave to selectively illuminate and excite fluorophores in a restricted region of the specimen immediately adjacent to the glass-water interface, and thus penetrates to a depth of only approximately 100 nm into the sample medium. The penetration depth is related the incident angle of the excitation laser. TIRFM is a perfect imaging tool to study cell membranes or other samples attached to the cover glass since its axial super resolution and removal of out-of-focus background.

In 2003, Forkey et al. applied linear dichroism with total internal reflection microscopy (TIRFM)[18]. In their work, the molecules were excited by an evanescent wave with four different polarization states, together with FA detection. The fluorescence was resolved into its components linearly polarized along the x and y axes and was detected by two photon-counting avalanche photodiodes. The study represents the first direct time-resolved measurement of tilting in an actively translocating motor protein sufficient to explain the observed mechanical step. The head–tail junction of a myosin V molecule travels 36–37 nm for each major tilting motion. The setup was further extended by Sun et al. for 3D orientation detection[37,38].

Fluorescence Recovery After Photobleaching (FRAP) has also been combined with LD. In 1988, Velez and Axelrod combined linear dichroism and fluorescence anisotropy with FRAP[39]. According to the different absorption ratio of differently oriented dipoles when excited by a polarized laser, a flash of polarized laser creates an anisotropic distribution of unbleached fluorophores. Then FA is applied to study the fluorescence polarization relaxed by rotational diffusion, which leads to a time-dependent post-bleach fluorescence. They also compared two different FRAP probes and validated their setup on small latex beads with a variety of diameters, common fluorophore labels, and solvent viscosities.

1.2.4 Summary of different FPM methods

DPR method and parallel LA method have the power to measure dipole orientation at one shot. However, DPR requires defocused imaging at a specific distance (several hundred nanometers), which increases its difficulty in real application. Besides, the point spread function of the emitter would be much larger so that the spatial resolution would be decreased, making it impractical for imaging complex structures.

Both FA and LD are based on the analysis of the fluorescence polarization, either in excitation or in emission. FA setup seems to be more simple and could achieve simultaneous observation. However, the number of detection channels is usually limited by the total fluorescence signal. FA would also be affected by depolarization processes, such as resonance energy transfer, rotational diffusion, et al. Though these properties could provide FA with capabilities to image related phenomenon, they would bring errors in measuring the transition moments of dipoles. In contrast, LD is weakly affected by depolarization processes. It could have more sampling points within one modulation period, though it needs multiple frames for final results. Since FA and LD are separately placed in the detection path and in the excitation path, they are complementary other than conflict to each other. In some cases, LD and FA are implemented in the same instruments for specific purposes[18,37,38].

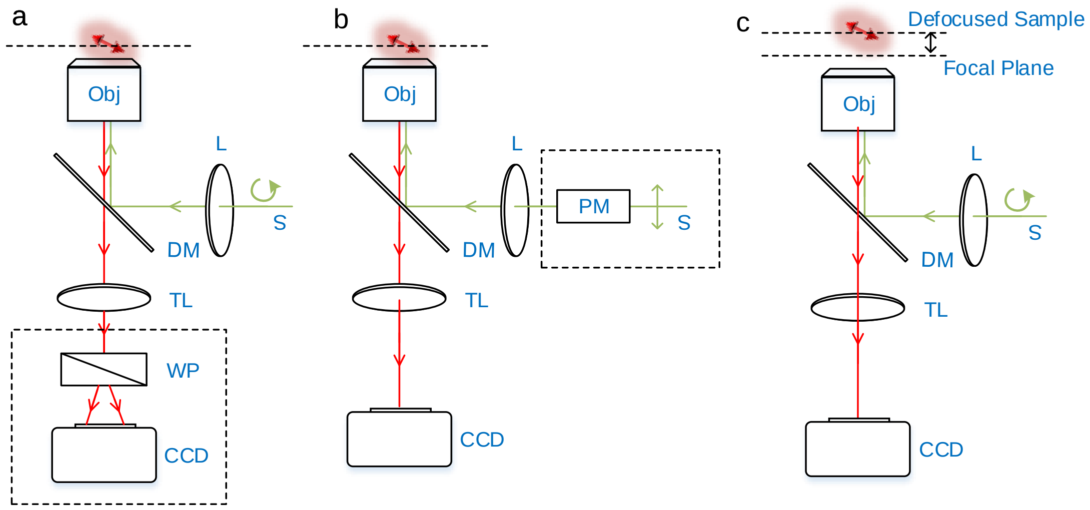

Figure 7 – Schematic setup comparison of different types of FPM.
(a) A typical setup of fluorescence anisotropy (FA). Circularly polarized light source is used, with either epi-illumination (displayed in the figure) or confocal illumination (together with point detectors, not displayed). Wollaston Prism (WP) could allow simultaneous detection of two polarization channels utilizing two halves of the camera. (b) A typical setup of linear dichroism (LD). The linearly polarized light source passes a polarization modulator (PM), resulting in varying polarizations of excitation light. The time trace images of fluorescence intensity changing with the excitation polarization would be recorded. Both epi-illumination or confocal illumination could be used and the polarization modulator could be a rotary half wave plate, an electro-optical modulator, etc. (c) A typical setup of defocused pattern recognition (DPR).

The sample is usually defocused with several hundred nanometers away from the focal plane of the objective. The diffraction pattern of the dipoles would be recorded and be used for orientation measurement. Circularly polarized light source is used for effective excitation of all the dipoles. Abbreviations: S – light source; L – collimating lens; DM – dichroic mirror; Obj – objective; TL – tube lens; CCD – CCD camera; WP – Wollaston Prism; PM – polarization modulator.

1.3 SUPER-RESOLUTION FLUORESCENCE MICROSCOPY

In 1873, Ernst Abbe proved that the resolution of optical microscopes would be limited by the optical diffraction[40], which is about 250 nm in lateral resolution for far-field optical imagine. The Abbe's diffraction limit ruled the optical resolution for more than one century, hindering the investigation of sub-cellular structures such as cellular organelles, proteins, DNA, and so on. The situation began improving since the development of super-resolution techniques. In 1989, W. E. Moerner and Kador successfully observed the fluorescence from single fluorophores[41]. Afterward, Stefan Hell proposed 4pi microscopy in 1992[42] and Mats Gustafson proposed I5M in 1995[43], which employed two opposing objectives to enhance the axial resolution to 100 nm. In 1994, Stefan Hell et al. proposed stimulated emission which could break the diffraction resolution limit. aiming at breaking the diffraction barrier by virtue of stimulated emission[44] (Hell and Wichmann, 1994), which was first demonstrated experimentally by Stimulated Emission Depletion microscopy by Stefan Hell in 2000[45]. Meanwhile, Eric Betzig et al. proposed a method for achieving super-resolution through single molecule localization in 1995[46], which was demonstrated experimentally by PhotoActivated Localization Microscopy (PALM) in 2006[47]. Almost at the same time, Xiaowei Zhuang developed Stochastic Optical Reconstruction Microscopy (STORM) utilizing ON/OFF switching of fluorescent dyes[48].

Hereafter, a variety of super-resolution techniques and their variants rapidly emerge, remarkably facilitating the investigations into complicated biological phenomena in life sciences. As a consequence, three major contributors and pioneers of optical super resolution microscopy, Eric Betzig, Stefan W. Hell, and W. E. Moerner, were awarded the Nobel Prize in Chemistry in 2014.

To summary, there are currently two main categories of far-field fluorescence microscopy techniques which have been developed to overpass the diffraction limit. The first type relies on the photoswitching fluorescence probes. This type includes PhotoActivated Localization microscopy (PALM)[47], Stochastically Optical Reconstruction Microscopy (STORM)[48], direct Stochastically Optical Reconstruction Microscopy (dSTROM)[49], Fluorescence PhotoActivation Localization Microscopy (fPALM), and other methods using similar principles. The extension of utilizing blinking or fluctuation of fluorophores is grouped in this category as well.

The second type includes the techniques that use patterned illumination to sharpen the excitation point spread function, possibly combined with the nonlinear response of the emission behavior of the molecules, such as Stimulated Emission Depletion, Ground State Depletion, Reversible Saturable Optical Fluorescence Transitions, Structured Illumination Microscopy and Saturated Structured Illumination Microscopy.

1.3.1 Single Molecular Localization Microscopy: PALM / STORM

PALM/STORM uses two different lasers to switch the fluorescent proteins (PALM) or fluorescent dyes (STORM) between ON state and OFF state. Usually, the sample is densely labeled with fluorophores and fixed. On each frame, only a sparse set of fluorophores are switched ON, which enables every single molecule to be localized at very high accuracy by Gaussian fitting. After the few bright molecules go to the OFF state, another statistically different set of fluorophores is activated and localized. This process is repeated continuously until the structure of interest is appropriately sampled. The final super-resolution image is reconstructed by plotting the localizations obtained from all switching cycles or by rendering them as a 2D Gaussian peak.

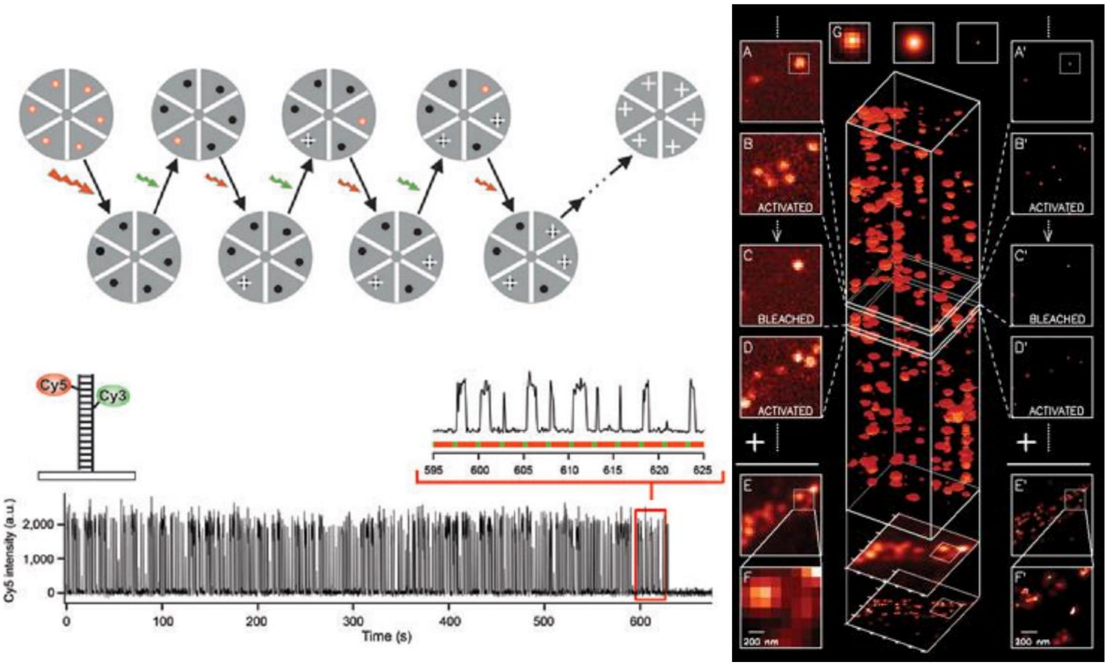

Figure 8 – The principle of PALM/STORM.
(left) The cy3-cy5 fluorophores can be switched between a fluorescent and a dark state by a red and green laser. In each imaging cycle, a green laser pulse switches on only a small fraction of optically resolvable fluorophores. The overall image is reconstructed from the fluorophores obtained from multiple imaging cycles. (right) PhotoActivated fluorescent proteins are attached to the proteins of interest and fixed within a cell. With a brief laser pulse of 405 nm laser, only a sparse subset of PA-FP molecules is activated and then imaged under 561 nm laser until most of them are bleached. The process is repeated many times until the population of inactivated, unbleached molecules is depleted. Fitting the expected molecular image given by the

PSF of the microscope and summing them across all frames, the actual molecular image could be plotted. Figure adapted from [47,48].

Instead of switching the fluorophores between ON/OFF states by controlling of two different lasers, dSTROM promoted the photoswitching of small organic fluorophores (Alexa Fluor and ATTO dyes) by adding milli-molar concentrations of reducing agent, such as β - mercaptoethylamine (MEA)[49]. The reversible photoswitching of Alexa Fluor and Atto dyes is due to the presence of thiols. The excitation laser would bleach the fluorophores of ON state while a laser of 405 nm promotes recovery of the fluorescent form[49].

Though the original images of PALM/STORM are still limited by the optical diffraction, the limit is of less importance when it comes to determining the location of a single, isolated sub-resolution particle. What matters is the precision and accuracy of localization. When every single is approximated by a Gaussian function and only shot noise is considered, the limit on the localization precision is given by[50]:

$$\sigma_x \geq \frac{s}{\sqrt{N}} \qquad \textbf{Eq. 6}$$

Where N is the total number of detected photons and s is the standard deviation of the Gaussian function. Real cases are more complex, even including cases of anisotropic emitters. When the fluorophore is rigidly linked to a stationary structure, it can be rotationally immobile, which could be taken as a dipole. The image of a dipole may exhibit asymmetry with increasing out-of-focus distance relating to the dipole orientation.

Complementary optics would be beneficial to achieve accurate localization in this situation[51].

The temporal resolution is mostly determined by the time accumulating enough single molecule so that adjacent localization points can be closer than one-half of the desired spatial resolution (Nyquist criterion)[52]. Achieving a 50-70 nm spatial resolution usually requires tens of thousands of frames or tens of minutes. A number of methods try to improve the speed of PALM/STORM by efficiently retrieving single-molecule positions when the single fluorophore signals overlap. Hence, the number of detected molecules increases as higher labeling density. The DAOSTROM are based on fitting clusters of overlapped spots with a variable number of system PSF with maximum likelihood estimation[53]. The Bayesian statics is also used to estimate clusters of overlapped molecules[54]. Bo Huang et al. applied global optimization using compressed sensing to even higher molecular densities and demonstrated live cell imaging of fluorescent protein-labeled microtubules with a 3-s temporal resolution[55].

There also some other super-resolution techniques not directly depending on single molecular localization but relying on the fluctuation property of the fluorophores, including Super resolution Optical Fluctuation Imaging (SOFI), Bayesian analysis of the blinking and bleaching (3B) method, and so on.

SOFI is based on the analysis of independent stochastics fluorescence fluctuations of emitters and does not require controlled or synchronized photoactivation. Super-resolution image could be achieved by SOFI with simply taking a movie of the sample within several seconds. To achieve successful SOFI imaging, the fluorescent label should have at least two different emission states and switch between states repeatedly and independently in a stochastic way. The pixel value of a SOFI image could be obtained by calculating the cumulant of the original pixel time series. Compared to the signal from different nearby emitters of conventional wide field microscopy, the cumulant, which is calculated from the correlation function of fluctuated signals would remain only highly correlated fluctuations. In practice, the remitting signal is limited to emitters within the pixel, while the fluorescence signal contribution of these emitters to neighboring pixels will nonlinearly yield lower correlation values, leading to an increased resolution[56].

The 3B microscopy has lower requirement of the microscope setup, which uses a xenon arc lamp instead lasers for illumination. The method fully utilizes the data from overlapping fluorophores as well as information from bleaching events, blinking events and changes caused by fluorophores being added or removed in the cell. To fully model the complimentary information, a Bayesian technique is used to model the resulting high-density fluorophore image data as arising from a number of fluorophores, each of which can emit light but which do not necessarily emit light in every frame. By modeling the whole dataset as arising from a number of fluorophores, we were able to use all of the fluorophore reappearances, even those in non-adjacent frames, and thus use all the photons collected from a fluorophore to improve the determination of its position. 3B microscopy could achieve localization microscopy with a spatial resolution of 50 nm and a temporal resolution of 4s on podosomes in living cells[57].

1.3.2 STimulated Emission Depletion (STED)

STED setup uses two synchronized trains of laser pulses: a train of visible pulses is used for excitation and another near-infrared one for stimulated emission depletion. Each excitation pulse is immediately followed by a STED pulse. The duration of the excitation pulse is ultrashort to excite the fluorophore from ground state S0 to the excited state S0. Another STED pulse is stretched to a longer pulse compared to the relaxation time of the vibrational substate of the ground state into which the molecule is quenched. The long period of STED pulse allows the quenched molecules to escape re-excitation by the same beam through vibrational relaxation. A $0 - 2$pi optical phase plate is used to achieve a special doughnut shape of the STED beam, which is intense around the focal point, but dark within it in 3D. The x-z distribution of the STED beam is displayed in Figure 9d. Compared confocal microscopy, STED further reduce the illumination volume in all dimensions by the depletion beam, bringing an increased lateral and axial resolution.

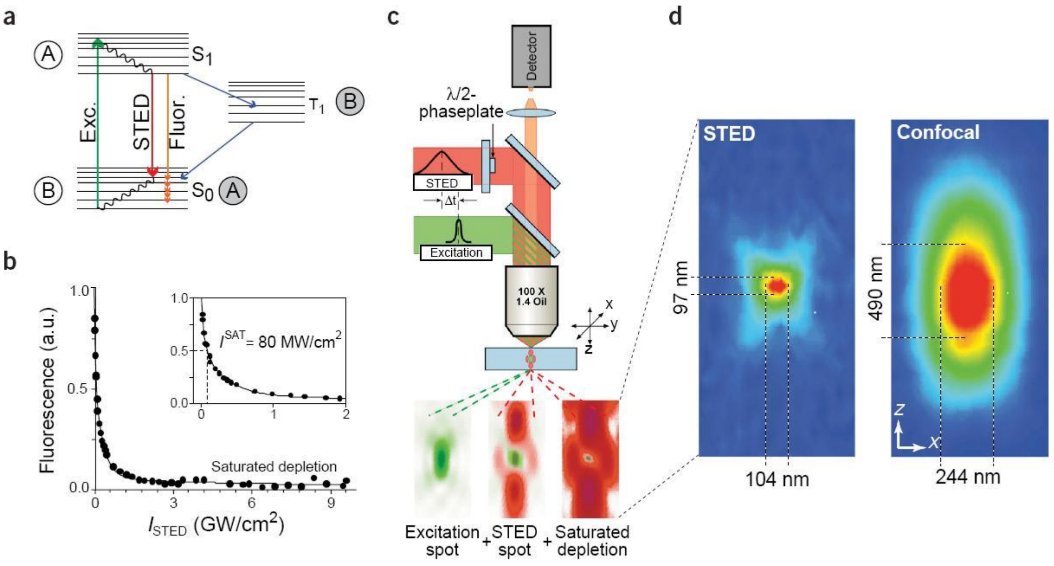

Figure 9 – Principle of STED.
(a) Jablonski diagram of STED progress; (b) Profile of left fluorescent intensity vs depletion power intensity; (c) System setup of STED; (d) Comparison of the PSF between confocal and STED. Figure adapted from[45,58].

When the power of the depletion beam goes higher, more fluorescence would be quenched, which brings smaller PSF. The resolution of STED, i.e. the FWHM of the PSF, is proportional to the inverse of the square-root of the depletion laser power:

$$\delta = \frac{\Delta}{\sqrt{1 + \frac{I_{dep}}{I_{sat}}}} \qquad \textbf{Eq. 7}$$

where δ denotes the system resolution, Δ denotes the FWHM of the excitation laser spot, and I_{dep} is the laser power of the depletion beam.

For imaging speed, STED is based on point-scanning scheme, which is limited by the scanning speed, which, however, has been improved via various techniques. In 2013, nanoscopy with more than 100,000 ‘doughnuts’ was achieved by two incoherently superimposed orthogonal standing light waves. The intensity minima of the resulting pattern act as ‘doughnuts’, providing isotropic resolution in the focal plane and making pattern rotation redundant. This parallelized acquisition could image live cells in 120 um * 100 um-sized fields of view in less than 1 second[59]. Utilizing the ultrafast scanning speed of electro-optical instruments, STED could achieve an imaging speed of more than 1,000 frames per second. Under such imaging condition, the pixel dwell time is on the order of the lifetime of the fluorescent molecular state so that the image becomes assembled ‘one photon at a time’, in a temporally stochastic manner. The ultrafast STED modality has an obvious potential to detect dynamic processes at higher imaging rates and provides increased photon yield in standard fluorophores compared to slow scanning[60].

Until now, STED has been reported with the highest resolution of 5.8 nm in imaging nitrogen-vacancy centers under the depletion power of 3.7 GW/ cm^2[61]. For biological samples, STED could achieve a resolution of 20 nm using organic dyes[62] and 50-70 nm using fluorescent proteins[63,64]. STED could also achieve ultra-fast imaging speed with biological samples[60,65,66].

1.3.3 Structured Illumination Microscopy (SIM)

Structured Illumination Microscopy (SIM) achieves super resolution imaging based on wide field epi-illumination. The structured illumination utilizes the moiré fringes to reveal high-frequency details which couldn’t be recorded before[67]. Non-linear response of the fluorophores could further provide more information of higher frequencies[68].

In optical microscopic systems, the highest spatial frequency k_0, which could be measured under the traditional resolution limit, is described by the formula:

$$k_0 = 2N.A./\lambda_{em} \qquad \textbf{Eq. 8}$$

where λ_{em} is the wavelength of the emitted fluorescence and $N.A.$ is the numeric aperture of the objective. In the diffraction-limited microscope, the information with the frequency higher than k_0 couldn't be observed. The increase of resolution equals to extend the higher frequency of observation. In structured illumination, laser incidents through a grating to form the moiré fringes. If the spatial frequency of illumination is k_1, the sample with spatial frequency k contributes to the moiré fringes of frequency $k - k_1$, thus revealing higher spatial frequencies than k_0 in recorded images. Added frequency brings higher imaging resolution. To maximum the added resolution, a higher frequency k_1 of illumination is needed. Unfortunately, the spatial frequency of the illumination is limited by the diffraction pattern and cannot exceed k_0. Hence, the maximum frequency achieved by SIM is $k_1 + k_0 \leq 2k_0$, so that SIM could double the imaging resolution at most. Nonlinear SIM is later developed to further improve the resolution[68]. The principle is similar with STED, which utilizes the nonlinear response of the fluorescent probes. Nonlinear SIM could achieve theoretically unlimited resolution. However, the improvement of resolution would be limited by the experimental limitation of SNR, the stability of the probes, etc.[69]. Recently, advanced SIM and nonlinear SIM techniques keep developing[70,71]. High NA TIRF-SIM has achieved spatial resolution of 84 nm and patterned activation nonlinear SIM

(PA NL-SIM) has reached 45 nm to 62 nm resolution, also at sub-second acquisition, over ∼10 to 40 time points.

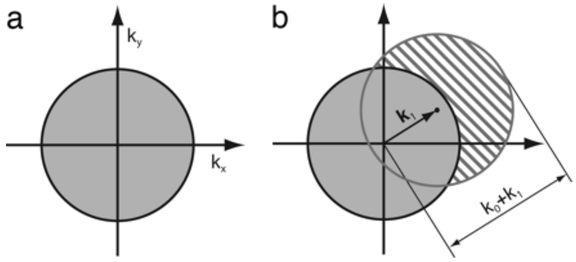

Figure 10 – Schematic principle of SIM.
(a) The spatial frequency field of detection in wide field microscope. (b) Extended spatial frequency field of detection for in SIM.

RESEARCH OVERVIEW

Though a large variety of super resolution techniques have been developed for fluorescence intensity imaging, super resolution FPM is still in its infancy. The spatial resolution is not only critical for distinguishing the biological structures, but also highly related to the accuracy of the measurement of dipole orientation, since the measured fluorescence anisotropy is contributed by all the dipoles within the diffraction limited area. To achieve super resolution with dipole orientation measurement, one simple thought is to combine FPM with existing super resolution techniques, such as STED, SIM, PALM/STORM, etc. The other thought is to exploit the intensity modulation of LD, which modulates the excitation laser and gets a sinusoidal response of the sample. The work in this dissertation chooses the second approach, which focuses on the developing super resolution measurement of dipole orientations via linear dichroism.

The dissertation is organized as follows. Chapter 1 introduces the research background, including the basics of fluorescence polarization, FPM based on DPR, FA and LD, and various super resolution techniques. Chapter 2 illustrates the principle and setup of super-resolution dipole orientation mapping (SDOM), followed by the derivation of its reconstruction algorithm. SDOM imaging results contain a comparison with SPoD, simulation verification, fixed sample results and live cell results. The limitation of SDOM is also discussed and a comparison between SDOM and other SR-FPM is included. Chapter 3 includes two further improvements of SDOM: (1) using optical lock-in detection to improve signal-to-noise ratio and resolution; (2) achieving 3D super resolution of SDOM. Chapter 4 includes my other work during graduate study., including light field microscopy and binding kinetics of proteins of the cell membrane. The last chapter is a summary and conclusion of the dissertation.

CHAPTER 2. SUPER-RESOLUTION DIPOLE ORIENTATION MAPPING

Super-resolution techniques break the diffraction barrier through intensity On-Off modulation. The modulation could be in a structured manner, such as STED or SIM, or in a stochastic manner, such as PALM/STORM. The polarization modulation devices in LD system could naturally provide cosinusoidal intensity fluctuation of fluorescent. To exploit the intensity modulation of LD, potential super resolution techniques have been proposed. In 2014, Hafi et al. developed super resolution by polarization demodulation (SPoD) and excitation polarization angle narrowing (ExPAN) which achieved super resolution with neither structured illumination nor special switchable or blinking fluorescent probes. Though SPoD with ExPAN achieved super resolution through polarization demodulation, the information of dipole orientations is lost during the deconvolution process. Hence, SPoD couldn't be strictly taken as a form of FPM. There also has been an interesting debate on whether polarization modulation adds super resolution or not.

To achieve super resolution imaging in both dipole intensity and orientation, we developed super resolution dipole orientation mapping (SDOM), extending SPoD with measurement of dipole orientations. Instead of the SPEED algorithm in SPoD, SDOM establishes a polarization-variant model, in which the intensity determines the super-resolution microscopic image using sparsity-enhanced deconvolution, while the phase determines the effective dipole orientation of each super-resolved focal volume using least squares estimation, thus fully exploiting the polarization modulation information.

This chapter illustrates the principle of SDOM①, system setup of SDOM and SDOM imaging results. The part of SDOM principle includes the theory of how polarization modulation brings super resolution, modeling of the SDOM optics, and reconstruction algorithm of SDOM. The part of SDOM system setup includes microscope setup, polarization modulation via rotary half wave plate, polarization distortion and system calibration. The part of SDOM imaging results includes simulation verification, and imaging results including fixed samples and live cells. The last section concludes the discussion of SDOM, including the Orientation Uniform Factor (OUF), a comparison between SDOM and SPoD, and limitation of SDOM.

2.1 PRINCIPLE OF SDOM

2.1.1 Super resolution via polarization modulation

The image of a single emitter is an Airy disk when observed by optical microscopes, or a spot with approximate 2D Gaussian distribution. The spot is also termed as the point spread function (PSF) of the microscope. The typical size of PSF is ~ 250 nm, which is the full width at half maximum (FWHM) of the Gaussian distribution. When two emitters are getting closer and closer, within the FWHM of PSF, they may appear as a single spot and could hardly be distinguished (Figure 11 c, upper panel). STED and SIM try to resolve the two emitters by creating a system PSF whose size is even smaller than the distance between

---

① The majority of the work in this chapter has been published in [[72] Zhanghao, K., Chen, L., Yang, X.-S. *et al.* Super-resolution dipole orientation mapping via polarization demodulation. *Light: Science & Applications* **5**, e16166, 2016. The system modeling and reconstruction algorithm is equally contributed by Mr. Long Chen and me. The system setup and experiments is mostly done by myself, with the help of Mr. Xusan Yang and Miss. Miaoyan Wang. For detailed contribution, please refer to the published article.

two emitters. PALM/STORM try to resolve them by switching the two emitters ON or OFF stochastically, thus in some frames, only one emitter is ON and localized. SDOM thinks in a different way, from the perspective of fluorescence polarization.

When the additional dimension of fluorescence polarization is introduced, each emitter could be taken as a dipole. The attributes of the dipole include intensity and orientation. When two neighboring dipoles have different orientations, they could be distinguished even appearing as a single spot in the intensity image. The dipole orientation could be measured by FA and LD. Here, we choose LD because it provides more sampling points in one modulation cycle, while FA is limited to two or four detection channels. When LD is applied, the fluorescence of each emitter behaves cosinusoidal response to the rotary polarized excitation. The phase of the sine curves is different, or the peak of the responses appears at a different time. Via different dipole orientation the diffraction limited emitters could be resolved (Figure 11 c, lower panel).

Things become complicated when there may exist multiple dipoles in the corresponding focal volume. The detected anisotropic fluorescent response consists of a contribution from all the chromophores. As proved in next section, the integration of fluorescence response in each pixel from various dipoles is still sinusoidal, which could be equivalently taken as an effective dipole. Though polarization demodulation and image reconstruction, super resolution dipole measurement of intensity and orientation could be achieved. In the conventional FPM, the neighboring fluorescent emitters cannot be distinguished if the distance is smaller than the optical diffraction limit. However, with super-resolution imaging power, SDOM analyzes polarization data from several fluorescent emitters under polarization excitation modulation. The sub-diffraction structure could be revealed by analyzing the distinct periodic fluorescence responses (Figure 11 c).

To simultaneously observe dipole intensity and orientation, the effective dipole is represented by an arrow. The direction of the arrow reflects the dipole orientation and the length of the arrow reflects the orientation uniform factor (OUF, which will be illustrated in next section). The arrows are superimposed on top of the super-resolution image. Besides, both intensity image and dipole orientations could be demonstrated simultaneously in a (X, Y, θ) coordinate system. In (Figure 11 d, e), we simulate two crossed lines with a dipole orientation difference of 90 degrees for instance. The image of orientation mapping and the (X, Y, θ) coordinate image are displayed respectively. The two densely-labeled intersecting lines have a uniform dipole orientation on each line, which is consistent with simulation settings. The super resolution intensity image shows a resolution of ~ 130 nm. When shown in a (X, Y, θ) coordinate system, two lines with different dipole orientations could be further separated.

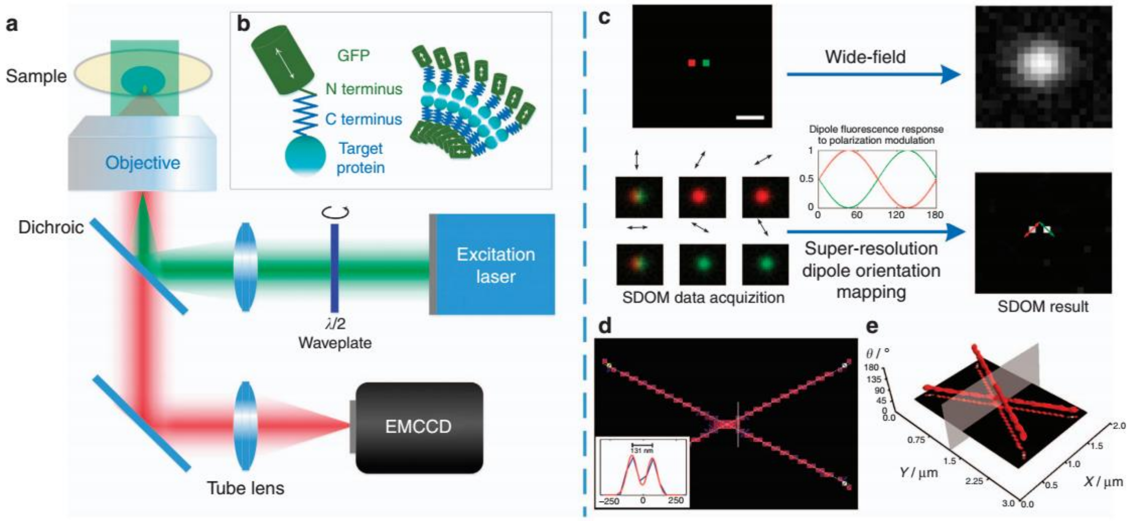

Figure 11 – Schematic diagram of SDOM.
(a) Setup of SDOM. Based on an epi-fluorescence illumination wide field microscope. The rotary linear polarized excitation is realized by continuously rotating a half-wave plate in front of a laser. (b) the fluorophores (such as GFP) linked to the target protein via the C-terminus (connected to GFP's N-terminus). (c) Illustration of the principle of the SDOM super-resolution technique via two neighboring fluorophores with 100 nm distance and different dipole orientations. Two emitters (pseudo color in red and green) emit periodic signals excited by rotating polarized light. Super resolution dipole orientation mapping is achieved by SDOM. (d) The SDOM result of two intersecting lines, with arrows on top of the super-resolution image, illustrating the dipole orientation and OUF. (e) The corresponding data are represented in (X, Y, θ) coordinates, in which the XY plane is the super-resolved intensity image. Scale bar: 200 nm.

2.1.2 SDOM system modeling

The epi-illumination wide field microscope usually detects the image via Electron-Multiplying Charge Coupled Device (EMCCD) or scientific Complementary Metal-Oxide-Semiconductor Transistor (sCMOS) camera. When the photons arrived are measured by the detector, the output signal is disturbed by the Poisson noise.

$$I(r,\theta) \sim Poisson\left(\mu(r,\theta)\right), \qquad \textbf{Eq. 9}$$

Here, θ is the polarization direction of incident laser, r is the position of the pixel. $\mu(r,\theta)$ is the number of photons which arrive at the sensor and $I(r,\theta)$ is the image acquired by the camera.

The *i*th emitting dipole at the position r_i is described by intensity $g_0(r_i)$ and orientation α_i . The photons emitted from each dipole are modulated by the polarization angle of illumination with a cosine-squared function $f(\theta,\alpha_i)=\cos^2(\alpha_i-\theta)$, which is blurred by the PSF $U(r)$ of the system. The background $b(r)$ is modeled as a polarization invariant with a shot time. A polarization-dependent periodic correction factor $I_0(\theta)$ is defined for the non-uniform response of the entire optical system. Since the imaging process is a convolution of the original sample and the PSF, the model of entire SDOM system can be described by:

$$\mu(r',\theta)=I_0(\theta)\left[\sum_i U(r'-r_i)g_0(r_i)f(\theta,\alpha_i)+b(r')\right] \qquad \textbf{Eq. 10}$$

The purpose of the SDOM algorithm is to estimate both the intensity $g_0(r_i)$ and the orientation α_i of each dipole. We denote $g(r_i,\theta)$ as the effective intensity under the illumination of polarization angle θ, which leads to $g(r_i,\theta)=g_0(r_i)f(\theta,\alpha_i)$. Thus, we can obtain

$$\mu(r',\theta)=I_0(\theta)\left[\sum_i U(r'-r_i)g(r_i,\theta)+b(r')\right] \qquad \textbf{Eq. 11}$$

The orientation α_i could be extracted from the polarization-variant effective intensity $g(r_i,\theta)$ using least squares curve fitting. Before that, because it is meaningless to calculate orientation in pixels without any dipoles, pixels containing no fluorescence signal can be marked on the super-resolution intensity image $g_0(r_i)$. For pixels containing dipoles, each pixel could be affected by more than one dipole. Assume there are *n* dipoles influencing pixel *i*, with orientation α_j ($\alpha_j \in [0,\pi]$) and the maximum number of photons M_j reaching pixel i. The polarization-variant intensity could be expressed as:

$$g(r_i,\theta) = \sum_{j=1}^{n} \frac{M_j}{2} \cos(2\alpha_j - \theta) + \sum_{j=1}^{n} \frac{M_j}{2} \qquad \textbf{Eq. 12}$$

Through further calculation, the equation could be re-written in the form of:

$$g(r_i,\theta) = A\cos\left(2\bar{\alpha}_i - 2\theta\right) + B \qquad \textbf{Eq. 13}$$

For each pixel *i*, least squares curve fitting could be applied to Eq. 13 to estimate $\bar{\alpha}_i$. Instead of obtaining the orientation of each dipole, we calculated the $\bar{\alpha}_i$, which represents the average dipole orientation in pixel *i*. Dipoles with similar orientations show a strong mutual dipole, whereas when they distribute homogeneously, the mutual dipole degrades such that it has a strong dc component. Adjusted R square (adjusted-R^2) is used to describe the quality of curve fitting and involves calculating R^2 after normalizing the fitted data to [0, 1]. To guarantee the correctness of orientation mapping, only pixels with relatively large adjusted-R^2 are orientation-mapped on the image.

Moreover, in Eq. 12 and Eq. 13, A and B have the following analytic forms:

$$A = \sqrt{(\sum_{j=1}^{n} \frac{M_j}{2} \cos 2\alpha_j)^2 + (\sum_{j=1}^{n} \frac{M_j}{2} \sin 2\alpha_j)^2}, B = \sum_{j=1}^{n} \frac{M_j}{2}, \qquad \textbf{Eq. 14}$$

where A is referred to as the orientation amplitude, which contains the dipole orientation signal; and B, as the super-resolution translation, which contains the super-resolution signal. We define $OUF = A / B$ to evaluate our result. OUF describes the orientation uniformity of dipoles within a PSF area. Simulation in SI describes how the divergence in the orientation of dipoles can influence the OUF. In our orientation-mapped images, OUF is represented by the length of the arrow whose direction indicates the dipole orientation.

Because the effective intensity $g(r_i, \theta)$ considers polarization modulation information, additional information is included in this model, which allows additional polarization resolution, resulting in a much sparser representation.

2.1.3 Polarization Demodulation Algorithm for Image Reconstruction

To estimation the super resolution dipole intensity $g_0(r_i)$ and orientation α_i, we first demodulate $g(r_i, \theta)$ from the Poisson statistical imaging model (Eq. 10 and Eq. 11). Maximum a posteriori (MAP) is utilized for estimation. For better-converged iteration and accelerated computation, $\tilde{b}(r)$ replaces $b(r)$ in Eq. 11, which is the cosine transform of $b(r)$. All the variables $g(r_i, \theta)$ and $\tilde{b}(r)$ are independently and identically distributed, respectively. The blurred background usually varies slowly in space, the property of which can be achieved by requiring the sparsity of $\tilde{b}(r)$. Laplace (exponential) distribution can be applied to describe the prior sparsity of $g(r_i,\theta)$ and $\tilde{b}(r)$. The variables should be optimized to obtain the maximum of the target function, which is as below after applying log,

$$\underset{g,b}{argmin}\ L\left(g,b,I\right), \text{ where}$$

$$L(g,b,I)=\sum_{\theta}\sum_{r}(\mu-I\log\mu)+\lambda_1\left|g\right|_1+\lambda_2\left|\tilde{b}\right|_1 \qquad \textbf{Eq. 15}$$

After discretization, L is a multivariate function consisting of a convex smooth part and a convex non-smooth part. The FISTA algorithm can be applied to achieve fast minimization.

The whole reconstruction software is written in MATLAB. The FISTA function is firstly written in python code by Hafi et al.[31] and adapted by us into home-written MATLAB code. The first part is software synchronization between polarization modulation and EMCCD acquisition. The images are labeled with polarization directions and deconvolved by FISTA program. After reconstruction, the program reads the output and extracts dipole orientations via LSE. In the end, the orientation mapping images are displayed and could be checked via the home-written GUI. The whole software is introduced in Appendix A.

2.2 SYSTEM SETUP OF SDOM

2.2.1 Microscopy Setup

The system is based on a commercial inverted microscope (Nikon Ti-E), which is equipped with motorized TIRF illumination module. Two continuous-wave lasers (OBIS, Coherent) are used with the wavelength of 488 nm and 561 nm. Different wavelengths are selected by the Acoustic-Optic Tunable Filter (AOTF, AA Corp.). Since the output laser of the AOTF is linear polarized. The half wave plate is mounted behind AOTF. The laser is coupled to a polarization-maintaining optical fiber that is installed on a Nikon Ti-E motorized system. The dichroic mirror and emission filter with multiple wavelength bands passing are purchased from Chroma. To block other wavelengths of excitation light from the laser, an additional excitation filter is placed directly after the laser. The image is acquired by an electron-multiplying charge-coupled device (EMCCD, Evolva Delta 512, Photometrics). A 60X oil-immersion objective (NA=1.4, ApoPlan, Nikon) is used for epi-illumination and imaging. An additional 4X relay lens (Nikon VM4X) is used together with the Nikon 1.5 inner magnification to make the pixel size equal to 44.4 nm.

When the laser is used to excite the sample, two things should be checked. One is that the laser should transmit the sample upright, providing an in-plane polarization direction. This could be achieved by adjusting the x, y position of the collimating lens in the TIRF module. The other thing is that the excitation laser should be parallel instead of collimated. This requires the laser be focused on the back focal plane of the objective, which could be done by adjusting the z position of the collimating lens in the TIRF module.

SDOM doesn’t require a high intensity of excitation laser. However, the power of laser should be strictly constant, otherwise, the fluctuation of the laser power would influence the polarization modulation. The power of lasers used is usually constant with < 0.1% fluctuation based on our measurement. The typical excitation laser power is 20

W/cm^2 for actin samples and 100 W/cm^2 for live yeast samples. The exposure time of each image is 20 ms for actin samples and 100 ms for live yeast samples

For image acquisition, the motorized Nikon Ti-E microscope, the AOTF, and the EMCCD are controlled by Micro-Manager ($\mu Manager$). $\mu Manager$ is a software package for control of automated microscopes, which is based on the image processing application of ImageJ①. Experiments with polarization modulation, sometimes together with time series imaging and z-stack acquisition, are controlled via $\mu Manager$ and home-written scripts. Lasers are blocked by the AOTF timely to prevent photobleaching when the EMCCD is not imaging.

2.2.2 Polarization Modulation

Polarization modulation is achieved through another with LabVIEW programed controlling. The HWP is placed on a motorized rotary mount (G065117000, Qioptiq), which is driven by a stepping motor. The rotation speed is controlled by the voltage applied to the motor. The rotation speed varies from 0 ~ 120 r.p.m as the voltage is applied from 0 ~ 10 V. Accurate monitor of the HWP rotation is measured by the infrared LED and sensor. The infrared LED emits light to the rotary mount, which is marked by stripes of silver film. The reflected signal is monitored by the infrared sensor and transferred into a

---

① For more information, please refer to their website: https://micro-manager.org/.

voltage signal. The voltage signal is monitored by MyDAQ of National Instruments①. Though MyDAQ is a student data acquisition device, it has two 16-bit analogy inputs with 200 kS/s sampling rate which is enough for monitoring. MyDAQ in the system also contains another digital input which is the exposure output signal of the EMCCD.

Usually, the rotation speed of the half wave plate is adjusted for 10 acquisitions during a polarization modulation cycle of 180 degrees. It may contain more sampling points for the sample with low signal-to-noise ratio. For example, the total number of measurements is 10 for actin samples and 20 for live yeast samples. Since the polarization direction rotates at a double speed of the HWP rotation, it contains four polarization modulation cycles with one rotation of HWP. Thus, we usually implement 40 EMCCD acquisition during one rotation of HWP. Hence, the rotation speed of the mount should be adjusted to the exposure time and imaging speed of the EMCCD accordingly. The rotation speed is controlled by the supply voltage, which is hard to achieve a specific speed accurately. Instead, we adjust an approximate rotation speed of 40 acquisition per rotation and calculate the precise polarization direction by acquiring the rotation information and the EMCCD simultaneously. It’s a software based synchronization for the polarization modulation and the EMCCD imaging.

The synchronization data is recorded by MyDAQ and analyzed by home-written MATLAB code. Each single frame is labeled with the polarization direction at the time of

---

① MyDAQ is a cheap data acquisition and signal controlling device for educational purpose, provided by the National Instruments company. For more information, please refer to the website: http://www.ni.com/mydaq/.

acquisition. Since the HWP keeps rotating during the acquisition, the polarization direction is actually a mean one. The averaging of polarization would reduce the accuracy of orientation measurement and could be avoided by electro optic modulators, which remains to be our future work. Besides, the polarization direction here is a relative one and the absolute polarization direction needs still to include the actual axis of the HWP using a polarizer.

2.2.3 Polarization Distortion and System Calibration

Polarization Distortion is a general issue in FPM, which requires special attention. Optical elements like lenses, reflection mirrors, etc. wouldn't bring any distortion, while most polarization distortion is from the dichroic mirror. Other devices like the spinning disk unit, fibers are alternative sources. The polarization variant devices in our system include the AOTF, the beam splitter, the optical fiber, and the dichroic mirror.

The AOTF maintains a polarized output of laser due to its principle. What we need to do is to place the rotary HWP after the AOTF in the optical path. Polarization maintaining single mode optical fibers (PM fibers) usually have slight polarization distortion, which could be taken together with the dichroic mirror. Polarization distortion of the dichroic mirror could be approximately compensated by a quarter wave plate[35] or be accurately handled via a Berek's polarization compensator or the Soleil Babinet compensator[34].

Before polarization compensation, the system polarization distortion should be firstly measured. The system polarization could be described by a general elliptical polarization state with fast axis, slow axis, and their phase difference. In our system, a Berek's compensator (New Port) is used for compensation. The fast axis of the Berek's compensator is placed at the direction of the slow axis of the polarization distortion while the slow axis of the Berek's compensator is placed at the direction of the fast axis of the polarization distortion. The phase of the Berek's compensator is set to be the phase difference between the two axes of the polarization distortion.

Imaging System calibration of the polarization distortion could be measured by a polarizer placed on top of the objective when epi-illumination is used. Standard samples with known dipole orientation, such as fixed single molecules, GFP crystals[6], in vitro fluorescent labeled actin samples[73], are perfect for calibrating the system.

2.3 RESULTS OF SDOM

2.3.1 Simulation Verification of SDOM

To demonstrate the resolution of SDOM, two neighboring emitters with increasing dipole orientation difference $\Delta\alpha$ and increasing distances are simulated (Figure 12). Here two aspects have been considered: fluorescence intensity (without considering the dipole orientation in SDOM), and orientation mapped SDOM image. The spatial resolution of ~50 nm in the SDOM intensity image could be achieved with larger orientation difference, with pixel size of 25 nm (Figure 12 a-c). Horizontal profile plots declare ~50 nm resolution when $\Delta\alpha > 70°$ (Figure 12c). With orientation mapping to bring additional dimension for resolution enhancement, ~50 nm resolution can be obtained with pixel size of 50 nm. Orientation could be mapped within the error of 11° where the error refers to the angular difference between the ground-truth one and the mapped one. With background noise intensity 0.1% of the sample signal, SDOM reconstruction yields larger OUFs than the wide-field image, especially for increasing orientation difference, shown as longer arrows.

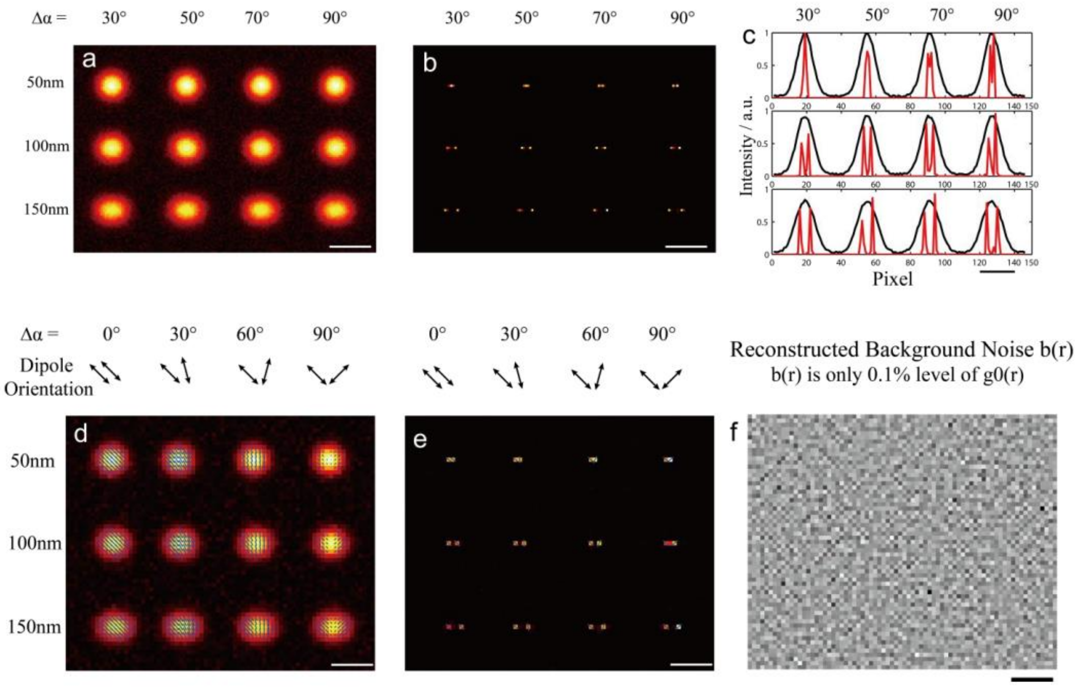

Figure 12 – Simulation of single-emitter pairs with different distances and dipole orientations for resolution and orientation mapping accuracy analysis.
(a-c) Intensity resolution analysis with pixel size = 25 nm. Images with 10 different excitation polarization angles are simulated, and the average intensity images are displayed for wide-field (a), and the SDOM reconstructed image is shown in (b). Intensity distribution indicates ~50nm resolution with phase difference greater than 70° (c). (d-f) Orientation mapping accuracy and resolution analysis with pixel size = 50nm. Average intensity image for wide-field (d) and corresponding SDOM result (e) with mapped orientations are demonstrated. (f) The SDOM reconstructed background b(r), which is only 0.1% of $g_0(r)$ for average signal intensity. The FWHM of the wide-field PSF is set to 250 nm. Scale bar: 500 nm.

Next, we verify the reliability of the orientation mapping of SDOM super-resolved images. Two neighboring emitters with a distance of 100 nm are simulated in large numbers and statistically analyzed (Figure 13). After 100 repetitions, we can see from the diagram that the angle detection error is within 5 degrees when two neighboring emitters have a 90-degree orientation difference. The angle detection error becomes larger when the difference of orientation becomes smaller. Overall, the angle detection error is within 10 degrees when the neighboring emitters have a dipole angle difference of $\geqslant$30 degrees.

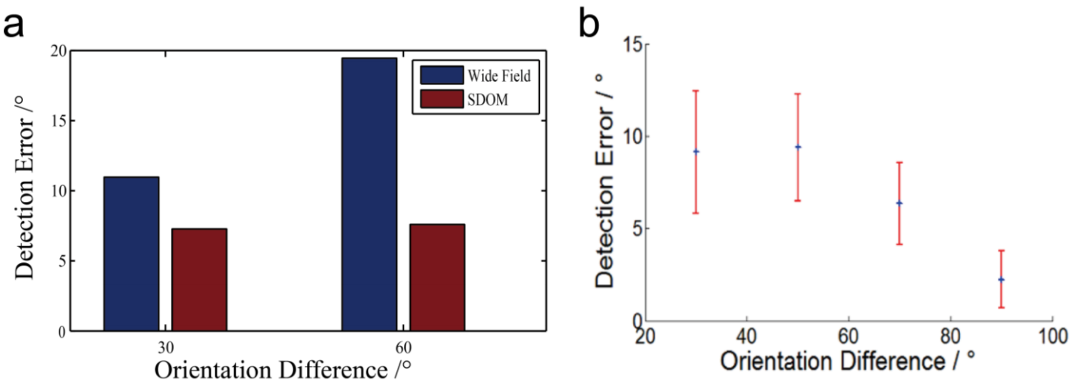

Figure 13 – Orientation mapping accuracy Analysis.
(a) Orientation mapping error in wide field is significantly larger than that in SDOM mapping result. (b)The orientation mapping error in the simulation of two neighboring fluorophores whose distance is 100 nm with various orientation differences.

We also generate a pattern of a 200 nm diameter circle for simulation (Figure 14). In the wide-field image, the circle looks solid, while the SDOM reconstructed image reveals a hollow circle shape. The reconstructed dipole orientation map clearly recovers the radial arrangement, with a much larger OUF than the wide-field counterpart. The simulation is further validated by the experiments of fluorescent beads with a diameter of ~500 nm in next section.

2.3.2 SDOM Imaging of Fixed Samples

In comparison with the simulation of 200 nm circle, we image fluorescent beads with a diameter of ~500 nm (F8888, Molecular Probes, Eugene, OR, USA). The bead sample is prepared following the protocol provided by the company. The rotational symmetric distribution of orientation mapping of fluorescent dipoles on the surface of 500 nm beads is also consistent with previous studies[31] (Figure 14).

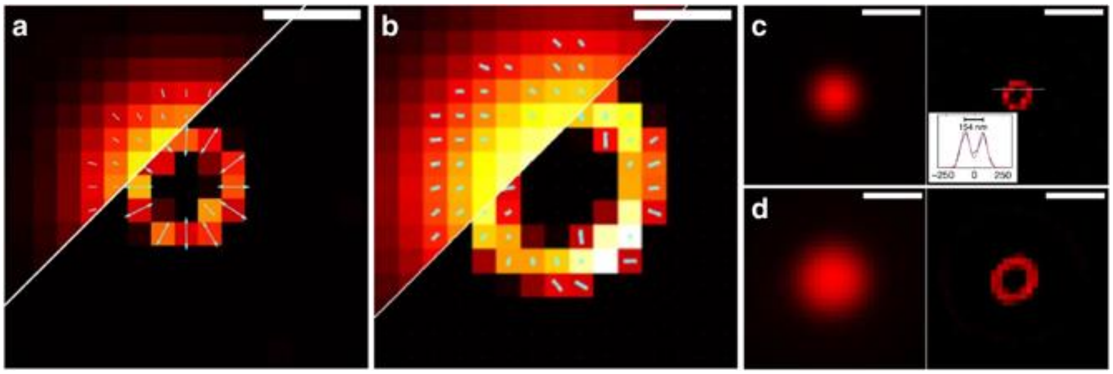

Figure 14 – SDOM images of simulated data and fluorescent bead.
(a) Wide-field (left) and SDOM result (right) of a simulated ring structure with 200 nm diameter. The orientation of the fluorescent emitters is normal to the ring. (b) Experimental images of 500 nm hollow fluorescent beads using wide-field microscopy (left) and SDOM super-resolution microscopy (right). In comparison, the wide-field and SDOM fluorescence intensity results of the simulated 200 nm ring (c) and 500 nm diameter beads (d) are also shown. Scale bar: (a, b) 200 nm, (c, d) 500 nm.

For imaging complicated cell samples, the actin of a mouse kidney tissue slice labeled with Alexa Fluor 568 phalloidin (F-24630, Molecular Probes, Eugene, OR, USA) is investigated using the SDOM method, whose fluorescence shows strong polarization (Figure 15). In the raw data, actin filaments of the same direction reach peak simultaneously, while filaments of different directions reach peaks at different polarization angles of the incident laser. The average intensity of 10 different fluorescence polarization-modulated images is equivalent to that in the traditional wide-field image. Several neighboring filaments, indicated by arrows, could not be resolved by conventional microscopy but are distinguished by the super-resolved intensity image of SDOM (In the intensity profile of Figure 15b, two filaments with a distance of 240 nm can be separated by SDOM, with 82 and 80 nm FWHM of each filament, calculated by double Gaussian fitting. Orientation mapping images using wide-field images and SDOM images are also compared. Because each single filament can be resolved in the SDOM images, the dipole orientation calculated is mostly influenced by fluorophores on the local filament. Thus, the fluorescent molecules with the same dipole orientation, or an isolated single-molecule, usually have a larger OUF, indicated by the lengths of the arrows. Because of the OUFs in Figure 15 c, e are very small, we have to magnify the OUF two-fold (which is proportional to the lengths of arrows labeled in the image), compared with the OUF in Figure 15 d, f, so that it can be shown properly. We also find that in the SDOM images, the dipole orientation of fluorophores is mostly perpendicular to the direction of actin filaments, while in the wide-field images the orientation is nearly canceled by the different directions of actin filaments. This fact is consistent with the definition of OUF and strongly demonstrates the importance of super resolution in fluorescence polarization imaging.

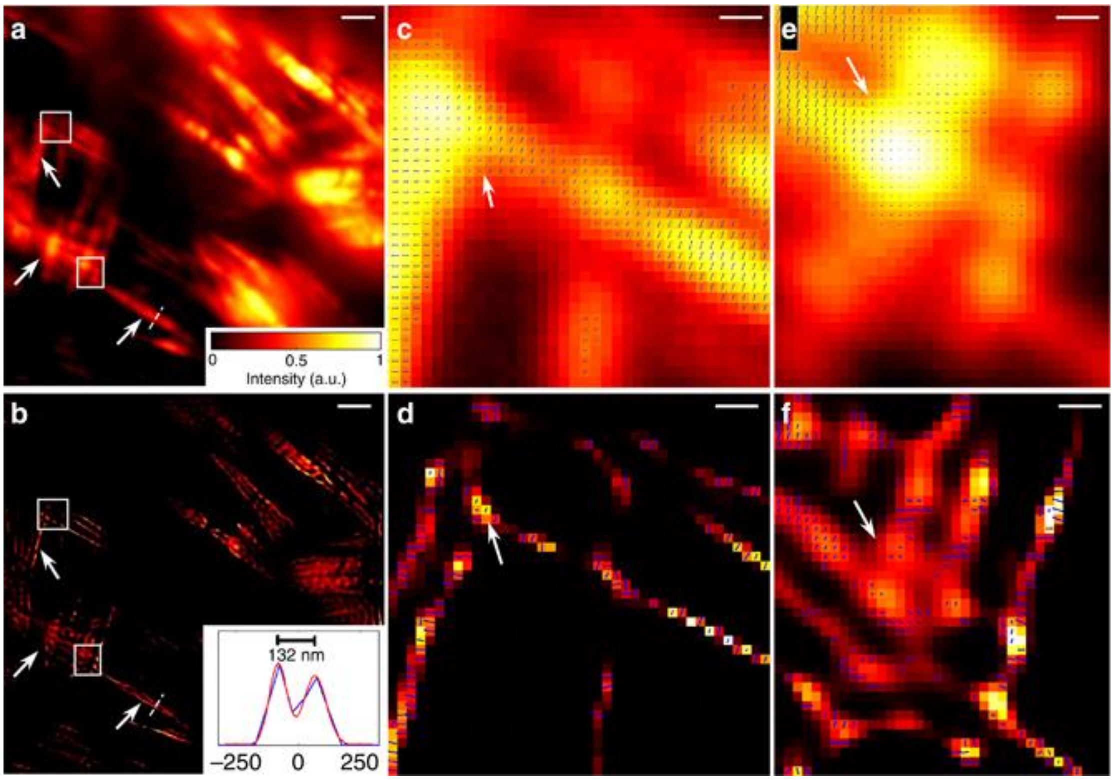

Figure 15 – SDOM imaging of actin in fixed mammalian cells.
Wide-field image (a) and SDOM image (b) of Alexa Fluor 568 phalloidin-labeled actin in fixed mouse kidney tissue cells. The diagram in b shows the intensity profile of the corresponding line indicated in a, b. (c, e) are zoomed-in wide-field orientation

mapping images and (d, f) are zoomed-in SDOM images. Scale bar: (a, b) 2 µm, (c–f) 200 nm.

2.3.3 SDOM Imaging of Live Cell Samples

To test how well SDOM can be used in live cell imaging, the GFP-labeled septin protein (Cdc12) in S. cerevisiae cells is imaged. Septin is regarded as the fourth type of cytoskeleton[74] and shows strong fluorescence polarization as well. The cross-sectional view image and top-view image are orientation mapped with both wide-field images and SDOM reconstructed images (Figure 16 a,b), both of which are consistent with PolScope results[28] but with higher resolution and higher OUF. The typical double-ring structure of the septin can be seen in the SDOM image; it cannot be distinguished in the wide-field image. The orientation mapped on the hourglass structure is consistent with PolScope results. To further illustrate how well SDOM can perform to detect the nucleus structure of live cells, the nuclear pore complex protein (Nic96) of S. cerevisiae cells, labeled with GFP, is also imaged using SDOM (Figure 16c); its fluorescent anisotropy was reported elsewhere[75].

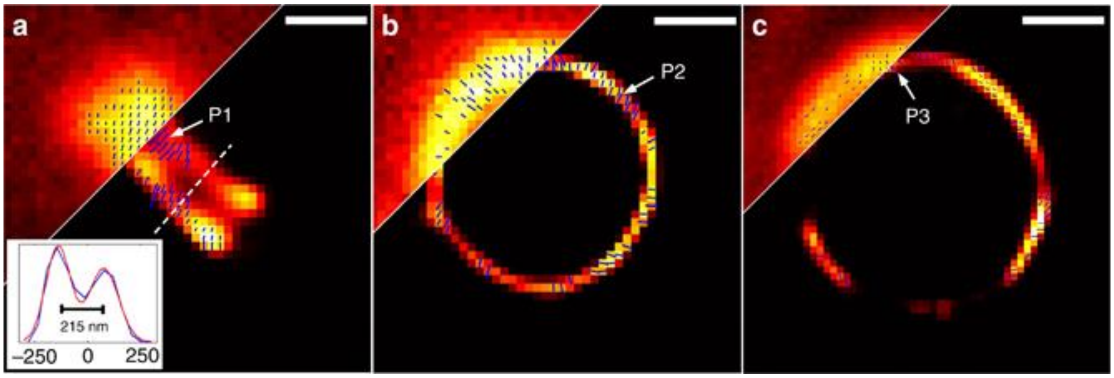

Figure 16 – SDOM imaging of septin and nuclear pore complex protein in live yeast cells.
(a) Orientation mapping images of GFP-labeled Cdc12 proteins in S. cerevisiae live cells (top view) with wide-field (upper-left) and SDOM (lower-right). (b) Cross-sectional view of GFP-labeled Cdc12. (c) Orientation mapping image of GFP-labeled nuclear pore protein, Nic96, in S. cerevisiae live cells. Scale bar: 500 nm.

The S. cerevisiae yeast strain AGY169-pRS416-ScCdc12-conGFP:GEN(4D4) was a generous gift from Prof. Amy Gladfelter's lab; it has 4 amino acids removed from the 3' end of the septin Cdc12 and 4 amino acids removed from the 5' end of the GFP with no linker between them. The S. cerevisiae yeast strain, with GFP-tagged nuclear pore protein Nic96, was obtained from a GFP-tagged budding yeast protein library33 purchased from Invitrogen.

To obtain the series of polarized fluorescence images for SDOM analysis, S. cerevisiae cells were grown in 3 ml of YPD in 10-ml conical tubes and shaken at 30 °C for 10 h. The cells were refreshed for two hours, and OD600 was checked before the cells were collected via 1000 rpm of centrifuge. Then, the collected cells were re-suspended in YPD, transferred to a slide, covered with a coverslip, sealed with VALAP, and imaged.

2.4 DISCUSSION

2.4.1 Orientation Uniform Factor

The less divergent the dipole orientations are, the larger the OUF is. We take n =5 fluorescent dipoles with equal maximum intensity M_i as an example to show that OUF is increasing to 1 as the phase difference $\Delta\alpha$ decreases (Figure 17 a, b). Figure 17 c demonstrates how OUF will change with respect to orientation difference, with two emitters in a pixel. Figure 17 d compares the wide-field OUF and SDOM OUF in the simulation in Figure 12 d, e. In Figure 17 e, f, OUFs of orientation-mapped images between wide-field and SDOM experimental data in Figure 16 are compared. Orientation mapping using wide-field data is equivalent to conventional linear dichroism methods such as PolScope. In comparison, SDOM not only creates orientation-mapping images with a higher resolution and accuracy but also has a larger OUF. The increase of OUF is mainly accredited to the improvement of resolution, which decreases the number of dipoles in the detection area, making the dipole orientations less divergent. SDOM algorithm also models unmodulated background noise into b(r), which reduces B and increases OUF (OUF = A / B). However, the latter one is the minor reasons since the detection area is reduced to a fraction of the wide-field detection area, and the background noise b(r) is usually much smaller than dipole signal g_0(r). Figure S1f shows the background b(r) whose average noise is 0.1% level of the signal of g_0(r) . As described before, larger OUFs give more accurate information for dipole orientation and are more robust to noise

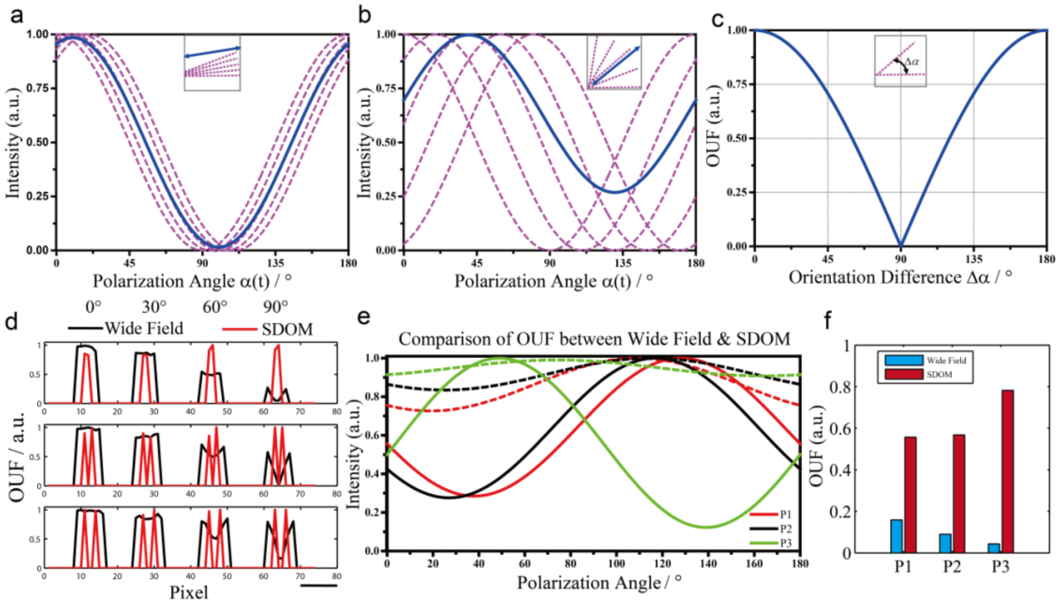

Figure 17 – Precision analysis of dipole orientation.
(a, b) The intensity of five simulated fluorescent dipoles with orientation difference of Δα= 5° (a) and 20° (b) respectively, and their average intensity with respect to polarization angle α(t) . In the gray box, the orientations of five molecules (magenta dotted lines) and average orientation (blue solid line) are presented respectively. (c) The analytic relationship between OUF and orientation difference for a two-molecule pixel. The gray box shows the orientations and orientation difference of the two fluorescent dipoles. (d) OUFs in wide field decrease with increasing phase difference, while OUFs in SDOM image keep large. (e) The intensity profile of polarization modulation data of diffraction limited and SDOM (P1, P2, P3 are indicated in Figure 16). The dotted lines display wide-field data with smaller OUFs and the solid lines reveal SDOM data with larger OUFs. (f) The blue bins demonstrate wide-field OUFs while the red bins show SDOM OUFs. a.u., arbitrary units.

2.4.2 Comparison between SDOM and SPoD

SPoD achieves super resolution imaging by detecting the periodic signals emitted with different phases from different nano areas under rotary polarized excitation. The rotary polarization of both excitation and stimulated beams is done by passing them through the same rotary half wave plate. The polarization modulation data contains 10 sampling point during each cycle and is demodulated by the SPEED (sparsity penalty-enhanced estimation by demodulation) deconvolution algorithm. The algorithm models each nano area as a mean dipole and distinguish neighboring emitters within the diffraction limited area through the different phases of cosinusoidal response to rotary polarized excitation, i.e. through different orientations of the mean dipoles. To achieve this, a model of the polarization modulated system is built and penalized maximum likelihood estimation is utilized to estimate original sample information. Fast iterative shrinkage-thresholding algorithm (FISTA) solves the deconvolution problem.

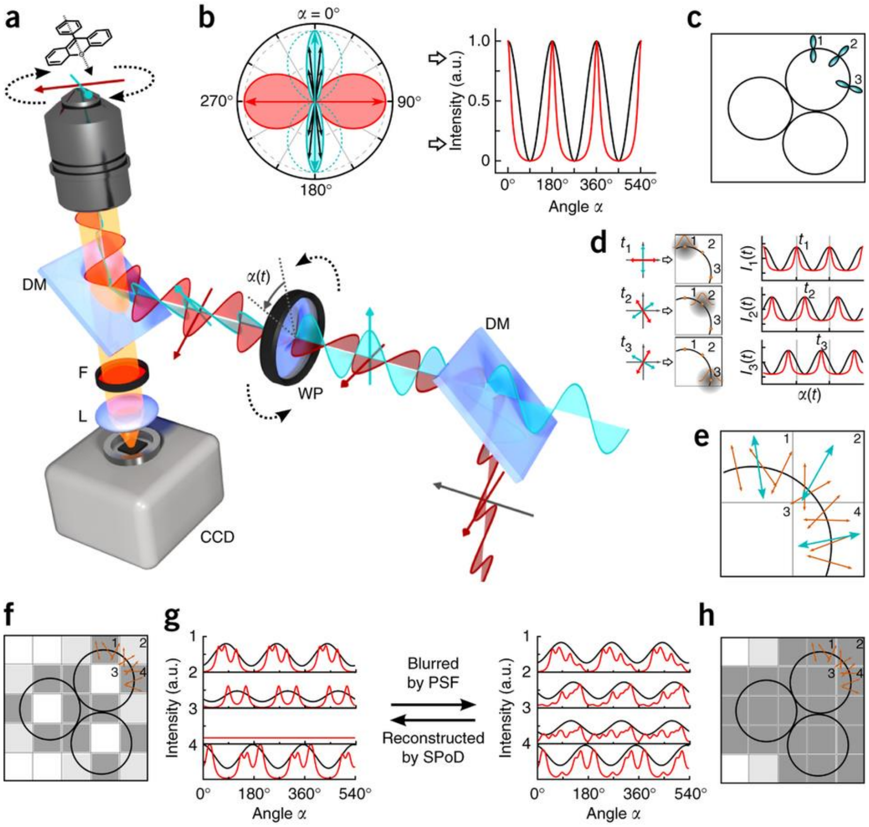

Figure 18 – Setup and principle of SPoD and ExPAN
(a) Schematic setup of SPoD. (b) Fluorescence response to polarized excitation and ExPAN. (c) Dipoles with different orientations. (d) Periodic responses of SPoD and ExPAN. (e) Simulation settings of the dipoles. (f-h) The fluorescence response blurred by PSF and reconstructed image by SPoD.

Though SPoD with ExPAN achieved super resolution through polarization demodulation, the information of dipole orientations is lost during the deconvolution process. Hence, SPoD couldn't be strictly taken as a form of FPM. There also has been an interesting debate on whether polarization modulation adds super resolution or not[73,76]. Super resolution dipole orientation mapping (SDOM) extended SPoD with measurement of dipole orientations, which adds promptly evidence to the debate[72]. Instead of the SPEED algorithm in SPoD, SDOM establishes a polarization-variant model, in which the intensity determines the super-resolution microscopic image using sparsity-enhanced deconvolution, while the phase determines the effective dipole orientation of each super-resolved focal volume using least squares estimation, thus fully exploiting the polarization modulation information.

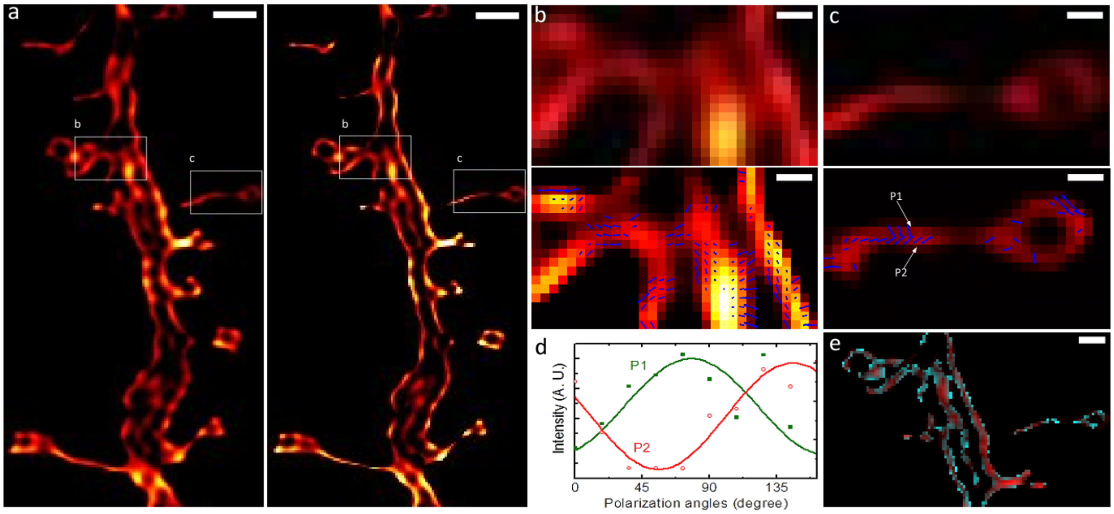

Figure 19 – SPoD and SDOM comparison using the same neuron dataset.
(a) Comparison of SPoD (left) and SDOM (right) images of dendritic spine neck in fEGFP membrane-labeled hippocampal neurons. (b, c) A close-up of the orientation mapping of dipoles from the corresponding boxed areas (upper panel, lower panel) in (a); the directions of the dipoles are illustrated using arrows. (d) Fluorescence response to the polarization modulation of P1 and P2 in (c), showing that these two points are almost perpendicular to each other with respect to dipole orientation. (e)

Composite image of OUF (pseudo color mapped in cyan) and fluorescent intensity data (pseudo color mapped in red). Scale bar: (a) 1 μm, (b, c) 200 nm, (e) 500 nm.

Though mathematically both Walla's SPoD method and SDOM approach provide similar intensity results, to unleash the full potential of polarization modulation in super resolution microscopy, the solution lies in the extraction of the orientation data of the emission dipoles of the fluorophores. More interestingly, we try to recover the dipole orientation in SPoD through the deconvolution of SPoD data in θ axis by Fourier analysis and find that the dipole orientation can also be determined, yet it requires much more iteration times than the deconvolution in (x, y) plane. Typically, after more than 520 iterations, the angle of polarization modulation may be deconvolved but the intensity data has already been well converged. This incoherent pace between spatial deconvolution and polarization deconvolution makes SPoD hard to obtain the super-resolved dipole orientation, and it becomes impossible to check the estimation accuracy for the data after multiple iterations. Though both SDOM and SPoD can extract the dipole orientation (angle information) to resolve the orientation of protein that a fluorescent label is attached to, and therefore indirectly adds super-resolution value, SDOM is based on a two-step orientation mapping process and more quantitative by using Fourier analysis to give the confidence in its resolved dipole orientations, indexed by OUF.

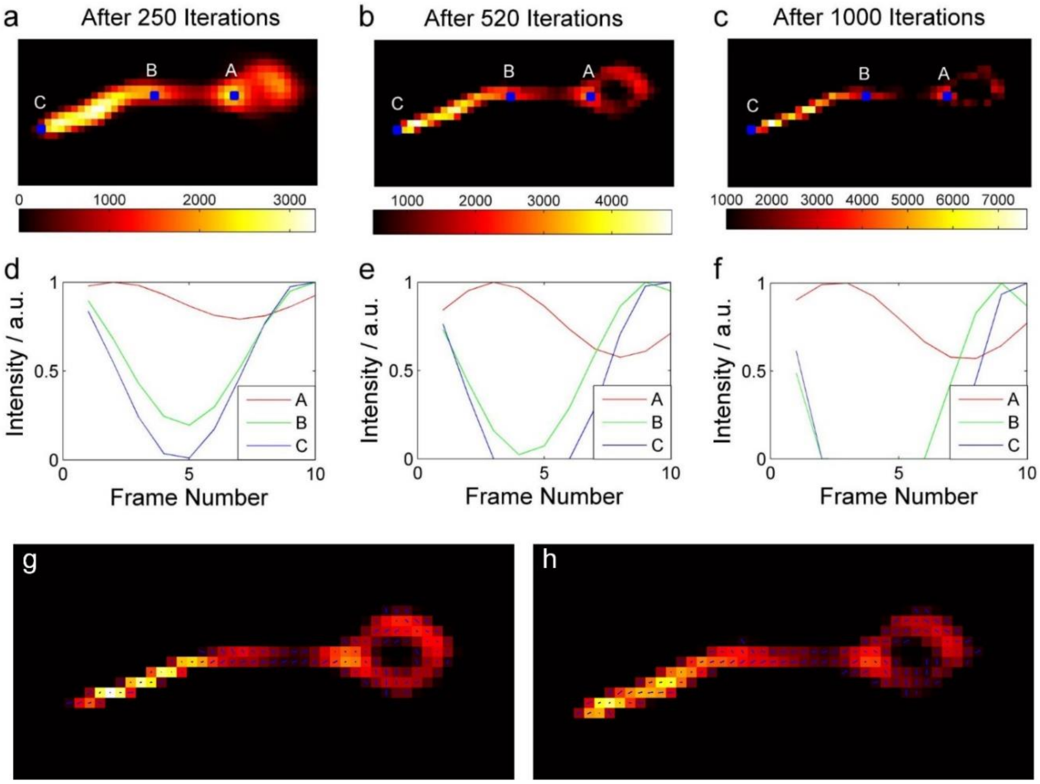

Figure 20 – Analysis of SPoD algorithm.
(a-c) Intensity image of SPoD after 250, 520, 1000 iterations. Deconvolved fluorescence polarization response of pixels A, B, C are shown in (d) with 250 iterations, (e) with 520 iterations and (f) with 1000 iterations. (g) Orientation mapping image of SDOM. (h) Orientation mapping image achieved by SPoD with Fourier analysis. The dipole orientation can be obtained with Fourier analysis to the SPoD result, after 1000 iterations. However, SPoD can only obtain the dipole orientation, but not the OUF which determines the confidence of orientation angle.

Compared to SPoD, SDOM can provide a super imposition of dipole orientation information on the super-resolved intensity images. This advance not only brings an additional optical dimension that can be used to resolve sub-diffrational details but also provides a rich set of biological structural information and functional discernment of subcellular organelles with details that could not be seen before.

2.4.3 Limitation of SDOM

Although SDOM yields super-resolution information with orientation mapping, it has some limitations. For the SDOM results of S. cerevisiae live cells and the neuronal spine, some pixels containing a fluorescence signal cannot be mapped with orientation because the adjusted-R^2 is relatively small. Ideally, every pixel can be fitted with sinusoidal equations, even with a chaotic orientation distribution of dipoles within a PSF area. However, non-mapping can happen when the dipole orientation rapidly changes at a scale similar to that of image acquisition time or a high level of system noise (such as polarization distortion of the dichroic mirror, fluctuation of laser power and so on) buries the polarization modulation information. Moreover, in the SDOM algorithm, because the super-resolved orientation is mapped in two steps, that is, estimation of dipole intensity followed by estimation of dipole orientation, the error of the intensity estimation may be transferred to the orientation estimation. One-step orientation mapping may reduce the intermediate fitting error but will cause difficulty in formulating some criteria, such as OUF, to select robust orientations. Designing and establishing other algorithms to solve the orientation or orientation distribution at the super-resolution level will be part of our future work.

SDOM is widely applicable to all the organic dyes, fluorescent proteins, and other inorganic dipole emitters such as gold nanorods, quantum rods, etc. However, SDOM could achieve super resolution only when the fluorescent emitters behave fluorescence anisotropy. When the fluorescent dipoles keep rotating or wobbling randomly during the imaging time window, the fluorescence anisotropy would be greatly reduced, making SDOM inapplicable, which usually happens to free fluorescent dipoles in solutions. When labeled to biological structures, the fluorescent dipoles are relatively fixed. Whereas the wobbling motion of the dipoles would still happen and it depends on how rigid the linker is between the fluorophores and labeled structures. The fluorescence anisotropy would also be small if large wobbling motion of the dipoles happens. We should also note that the resolution of SDOM is related to the local distribution of dipole orientations. With densely labeled, homogeneously orientated samples, SDOM can hardly resolve the polarization angle information due to the average of dipoles.

When only weak fluorescence anisotropy exists under the conditions such as large wobbling angle or densely homogenously labeled samples, the amplitude of polarization modulation would be small, compared to the noise level. To achieve super resolution dipole orientation mapping under such conditions, we further developed optical lock in detection with polarization modulation. In addition, to reduce the calculation errors during the two-step orientation mapping algorithm, a novel reconstruction algorithm is also proposed together with optical lock in detection, which is described in next chapter in detail.

CHAPTER 3. FURTHER IMPROVEMENTS WITH SDOM

3.1 SDOM WITH OPTICAL LOCK-IN DETECTION

Lock-in amplifiers are originally used in the area of signal processing, which extracts a signal with known frequency from a noisy environment. The input signal is multiplied by the reference signal and the output is integrated for over several periods, resulting in the detection signal with the same frequency and the same phase of the reference signal. Optical lock-in detection (OLID) utilizes optical control of the fluorescent and non-fluorescent states of the fluorophores and subsequently applying a lock-in detection method to isolate the modulated signal of interest from non-modulated background signals[77], which requires specifically designed probes and complicate synchronization.

Since the polarization modulation of SDOM provides a naturally periodical intensity modulation, OLID could be easily applied. Combining SDOM with OLID, super resolution lock-in dipole orientation mapping (SLIDOM) is developed. SLIDOM is applicable to all available fluorescent dyes and proteins and needs no additional hardware setup based on linear dichroism system. In this section, we will demonstrate the ability of SLIDOM to reduce stochastic noise like photon counting noise and thermal noise. As for other background signals like auto-fluorescence, scattering light and so on, SLIDOM is also applicable since these signals are mostly polarization invariant. SLIDOM is demonstrated to not only enhance the signal-to-noise ratio but also provide deeper insights into the results.

3.1.1 Optical Lock-In Detection with Improved SNR

The SLIDOM data is acquired by recording several periods of polarization modulation data. Lock-in detection is applied to the time series signal of each signal (Figure 21). The frequency of reference signal could be known from the recorded rotary information of the HWP. Various reference signals of different phases are applied, resulting in a sinusoidal lock-in output, which is the de-noised polarization modulation signal. The lock-in output is an ac signal I_{ac}, which contains the polarization variant signals. I_{ac} contains both positive and negative values, which couldn't be taken as an image. The polarization invariant signal I_{dc} could be retrieved by an average of the time series data. The addition of I_{dc} and I_{ac} could be proved to be positive, resulting in the outcome the de-noised lock-in output I_{LI}. I_{LI} could replace the originally acquired noise polarization modulation data and be reconstructed by the SDOM demodulation algorithm. Whereas, a new SLIDOM imaging model is established for reconstruction, which provides further super resolution and insights of the results.

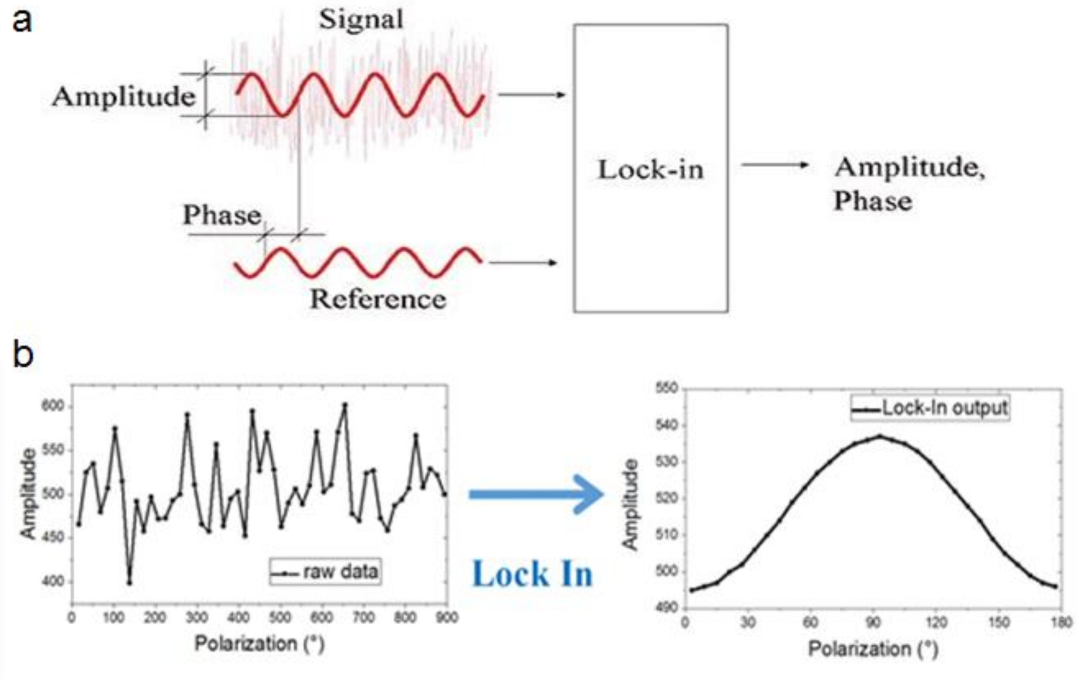

Figure 21 – Principle of Optical Lock-In Detection (OLID).
(a) Schematic illustration of Lock-In Amplifier. The noisy signal is multiplied by the reference signals and integrated. Lock-in output is part of the signal which has the same frequency and phase of the reference signal. The noise with other frequencies is attenuated. (b) Application of OLID to polarization modulation data. Five periods of polarization modulation data are recorded with low SNR ratio. OLID is applied to the time series signal on each pixel, with various reference signals of different phases. The OLID output is the de-noised sinusoidal response to the polarization modulation.

The original work on super-resolution by polarization demodulation (SPoD) technique[31] reported by Walla's lab has generated a rigorous debate on whether polarization excitation modulation adds substantial value to super resolution microscopy. Keller et al suspected the existence of polarization modulation in a diffraction limited area and demonstrated a similar improvement in super-resolution images using a sparsity penalty deconvolution approach, but without polarization demodulation[76], and Walla's lab provided further evidence to show that raw modulation information alone can provide sub-diffraction details[78]. With enhanced signal-to-noise ratio, one key concern of Keller et al. could be answered that the polarization modulation signal is mostly buried under the system noise.

Keller et al. find each pixel region contains an insufficient amount of fluorescence signal from polarization modulation comparing with Poisson noise that fluctuates at the same amplitude. When OLID is applied to each pixel of the noisy data, the noise is attenuated and the polarization modulation signal is extracted. Almost all of the spine head areas show significant polarization modulation, clearly distinguishable from the background area. Though the polarization modulation data contains only one period of data, the de-noising effect is obvious. Another dataset from Hafi et al. [78] is also tested, which contains 20 periods of polarization modulation. The ability of de-noising is compared between averaging and lock-in, the latter of which achieves more than twice higher SNR and five times better than the original data with sufficient periods.

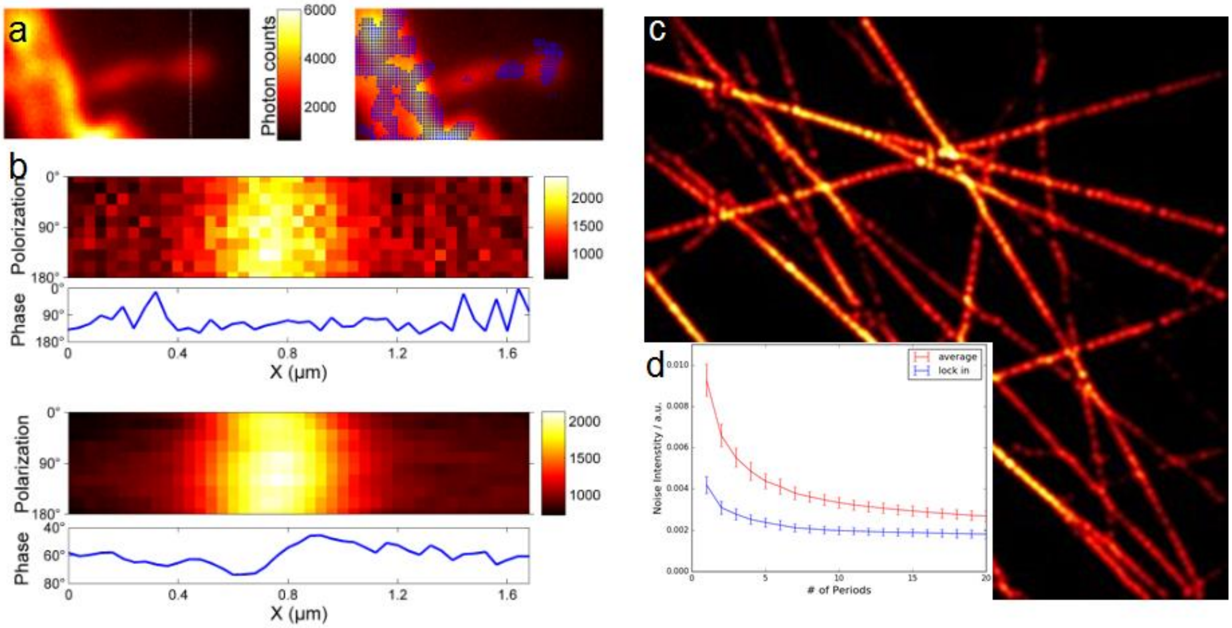

Figure 22 – De-noising effect of OLID.
(a) Polarization modulation raw data provided by Hafi et al. [31] Original data is on the left and OLID output is on the right. The marked pixels with blue dots contains significant polarization modulation amplitude than the background. (b) Modulation data on the line indicated on (a). Raw data is on the upper panel whose phases on each pixel is buried under the noise while OLID data is on the lower panel which contains disciplinary phase distribution. (c) Reconstruction results of in-vitro actin samples, with 20 periods of polarization modulation. (d) The amplitude of noise decreases as the increasing number of periods when lock-in is applied. Lock-in performs much better than averaging method, which provides five times higher SNR than the original signal with sufficient periods.

OLID could decrease not only the Poisson noise but also the out-of-focus noise The out-of-focus point spread function would spread along z axes, which would be influenced by a larger number of dipoles, reducing the polarization signal (i.e. OUF). As a result, the out-of-focus background signal would be mostly polarization invariant (i.e. ac signal). Since optical lock-in could specifically detect the ac signal, the out-of-focus background would be largely reduced. The out-of-focus signal of a ring structure with 200 nm diameter is simulated to illustrate this (Figure 23).

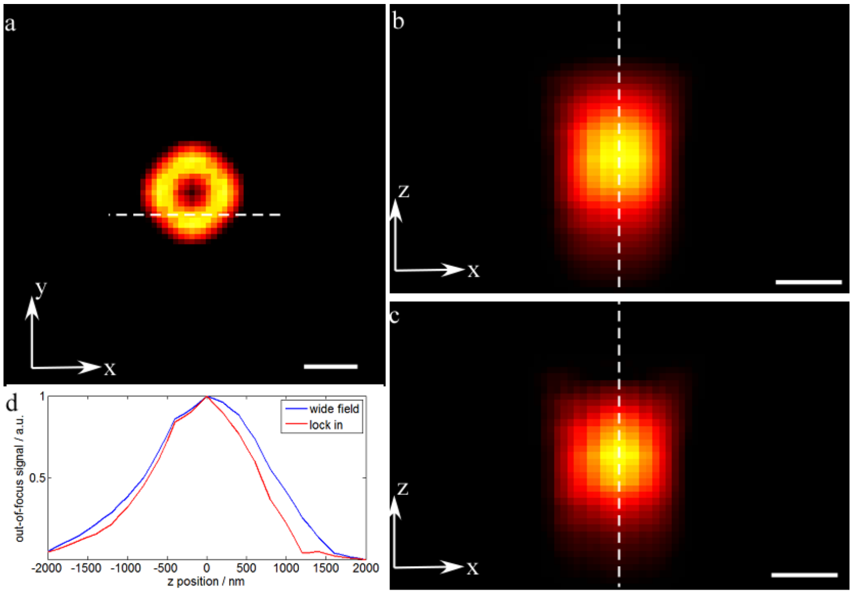

Figure 23 – OLID de-noising ability of out-of-focus noise.
(a) Wide filed image of the simulated ring structure. xz section images of the dashed line in (a) are shown in (b, wide field image) and (c, lock in image). (d) is the intensity profile of the dashed line in (b) and (c), which shows smaller out-of-focus signal in lock-in image than wide field image. Scale bar: 500 nm.

3.1.2 Further Super Resolution with SLIDOM

The other key concern of Keller et al. focused on comparable results achieved by pure deconvolution of average images, to which OLID provides a quantitative answer. The output of OLID separates the ac signal containing all the polarization modulation information and the dc signal of the average image: $I = I_{dc} + I_{ac}$. Since the point spread function (PSF) or system transfer matrix H also contains polarization related part and polarization non-related part, the reconstructed image G is also composed of dc image and ac image. The ac image is actually the additional super-resolution information brought by polarization modulation, while the dc image is the demodulation results of the average image.

The polarization modulation image could be seen as a convolution of the point spread function and each effective dipole in the pixel: $I(r',\theta)=\sum_i U(r'-r_i)g_i(\theta)$. The effective dipoles are usually not 100% modulated, which can be represented as: $g_i(\theta)=a_i+b_i\cos^2(\theta-\alpha_i)$. a_i denotes the dc signal, b_i denotes the ac signal, and α_i denotes the orientation of the effective dipole. Thus, the imaging model could be expressed as:

$$\begin{aligned}I(r',\theta)&=\underbrace{\sum_i U(r'-r_i)\bullet a_i}_{I_{dc}}+\underbrace{\sum_i U(r'-r_i)\bullet b_i\cos^2(\theta-\alpha_i)}_{I_{ac}}\\&=\sum_i\underbrace{U(r'-r_i)}_{H_{dc}}\bullet\underbrace{a_i}_{G_{dc}}+\sum_i\underbrace{U(r'-r_i)\cos^2(\theta-\alpha_i)}_{H_{ac}}\bullet\underbrace{b_i}_{G_{ac}}\end{aligned}$$

Eq. 16

or in the form of matrix:

$$I=I_{dc}+I_{ac}=\begin{bmatrix}H_{dc} & H_{ac}\end{bmatrix}*\begin{bmatrix}G_{dc}\\G_{ac}\end{bmatrix}$$

Eq. 17

When only average image is used for reconstruction, the imagine model would be:

$$I_{ave}(r')=\sum_i U(r'-r_i)\bullet g_{dc}=I_{dc}$$

Eq. 18

When lock-in process is applied, the results would be:

$$I_{ac}=\sum_i U(r'-r_i)\left[b_i\bullet 2\cos(2(\theta-\alpha_i))\right]=\sum_i\left[U(r'-r_i)\cos(2(\theta-\alpha_i))\right]\bullet 2b_i$$

Eq. 19

$$I_{dc}=\sum_i U(r'-r_i)\left[a_i+b_i\right]$$

If only average image is used, then dc image I_{dc} is obtained. The added resolution of polarization modulation lies on ac image I_{ac}. In some case, dc signal is much larger than ac signal so that the reconstructed images seem similar.

For the imaging model in Eq. 16, we could maximize the posterior with:

$$\Pr(a_i, b_i, \alpha_i \mid I(r', \theta)) \qquad \textbf{Eq. 20}$$

And fast iterative shrinkage-thresholding algorithm (FISTA) is used to achieve fast optimization. Then the super resolution results of SLIDOM is achieved.

An imaging process of a DNA origami Nano ruler (120 nm) sample is taken to illustrate the theory of SLIDOM①. When OLID is applied to raw data of multiple modulation periods, the noisy polarization curve in each pixel comes out with perfect sine shapes. The average (dc) image and the polarization (ac) image could be achieved separately, which adds up to de-noised output image (Figure 24). After SDOM analysis of the lock-in output, the super-resolution image with orientation mapping G is achieved, which is composed of dc and ac results. The G_{dc} image (left) is identical to the deconvolution results of the average image, in which the two emitters with a difference of 120 nm couldn't be resolved. However, in the demodulation results of G_{ac} image (middle),

---

① The experiments of DNA origami are performed by Miss Miaoyan Wang and the data is analyzed by me. The DNA origami sample is purchased from GATTA quant Inc.

two emitters are resolved, which could also be observed by dipole orientation in the orientation mapping image (right).

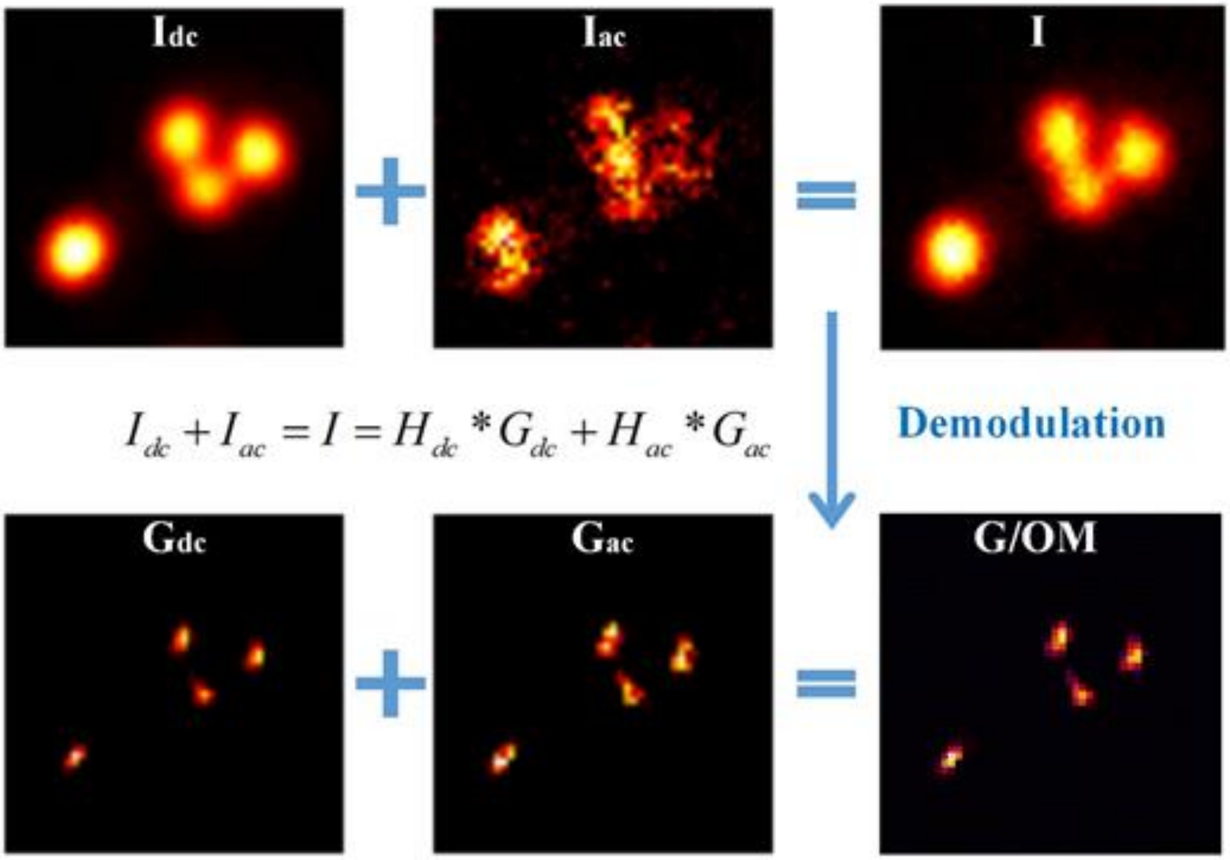

Figure 24 – SLIDOM results of 120 nm DNA origami.
The upper panel contains the OLID output of raw modulation data. I_{dc} is the average image; I_{ac} is the polarization variant image after lock-in; I is the addition of I_{dc} and I_{ac} for reconstruction. The demodulated super resolution results are in the lower panel. The polarization invariant reconstruction results G_{dc} couldn’t distinguish two neighboring emitters while the polarization variant reconstruction results G_{ac} could. The neighboring emitters could also be distinguished from the orientation mapping image (G/OM).

3.2 ACHIEVING 3D IMAGING OF SDOM

3.2.1 3D imaging of fluorescent beads

Polarization modulation could not only bring lateral super resolution but also enhance axial resolution. The underlying principle remains the same: dipoles with different orientation have a periodic response to polarization modulation with different peaks, which could be utilized to distinguish them. To implement 3D super resolution with SDOM/SLIDOM, 3D polarization modulation data should be firstly acquired, as well as the 3D PSF of the system.

The 3D polarization modulation data is acquired by z-scanning of the sample. At each z position, a polarization modulation data is acquired which contains 20-50 images. The stepping distance between each slice is 200 nm and a stack of 2.0-5.0 um thickness is acquired. 3D PSF measurement is also critical for good reconstruction results. The measurement is performed on 100 nm fluorescent beads. A z-stack with stepping distance of 100 nm is acquired. The acquired image is analyzed automatically by particle detection and image interpolation. The system PSF is obtained by averaging of multiple beads.

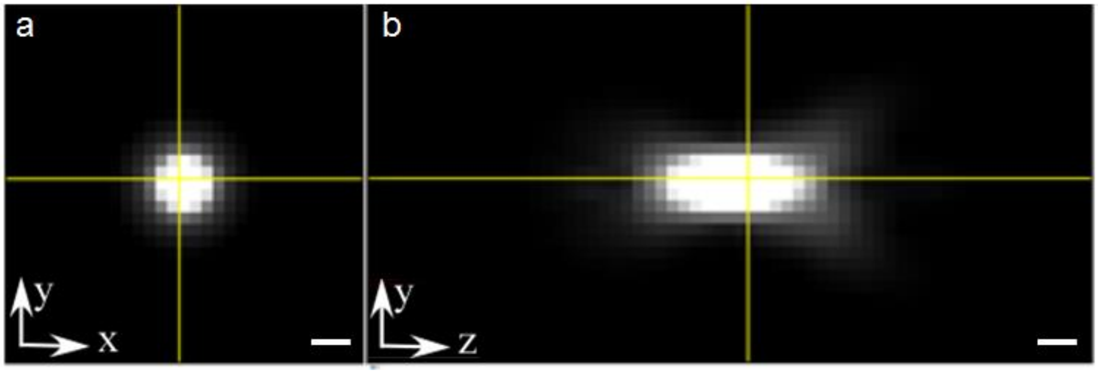

Figure 25 – 3D PSF of the system.
(a) x-y section of the system PSF. (b) x-z section of the system PSF. Scale bar: 500 nm.

Then, the imaging model of the system should be extended to 3D sample imaging. The same reconstruction algorithm could be applied. Since 3D polarization modulation dataset is very large, usually small areas are cropped during computation in case of memory issues of the computer.

To demonstrate the ability of 3D super resolution, the samples of 1 um fluorescent beads and actin in fixed cells are imaged. Firstly, 3D-SDOM imaged fluorescent beads sample with the size of 1 um. The fluorescent beads consist of a silicon core and surrounding dyes, which should appear to be a fluorescent shell. However, the shell structure couldn't be observed by wide field microscopes due to its dense 3D structure and the diffraction limit. With 3D-SDOM, we demonstrate the shell images of the fluorescent beads with the size of 1 um, which shows its super-resolution power in z axes. The sample preparation is the same with that in chapter 2.

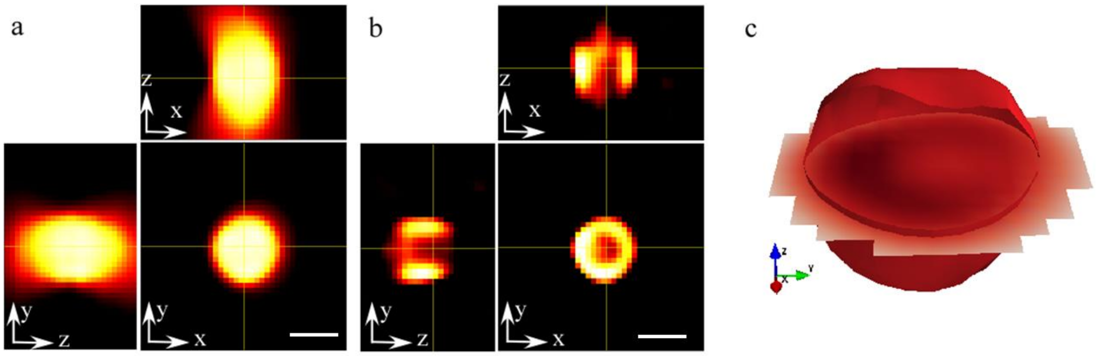

Figure 26 – 3D-SDOM imaging results of 1 um fluorescent beads.
(a) Wide field images, including x-y, x-z and y-z orthogonal views. The images appear solid due to dense 3D structures. (b) Orthogonal views of SLIDOM results, which reveals the shell structure of the fluorescent dyes. (c) 3D demonstration of the shell structure. Scale bar: 1 um.

3.2.2 3D imaging of actin in fixed cells

The sample of actin in fixed cells is a commercial one from ThermoFisher (FluoCells Prepared Slide, F36924). The F-actin is stained with Alexa Fluor 488 phalloidin. The laser intensity is controlled to avoid severe photobleaching and is switched off during z-scanning of the stage. The exposure time for each frame is 50 ms and 20 frames for each slice. A total depth of 2 um is scanned while only the inner part of 1 um is reconstructed since the boundary artifacts of the 3D deconvolution. The total acquisition time is about 2 min. The final results are shown in Figure 27.

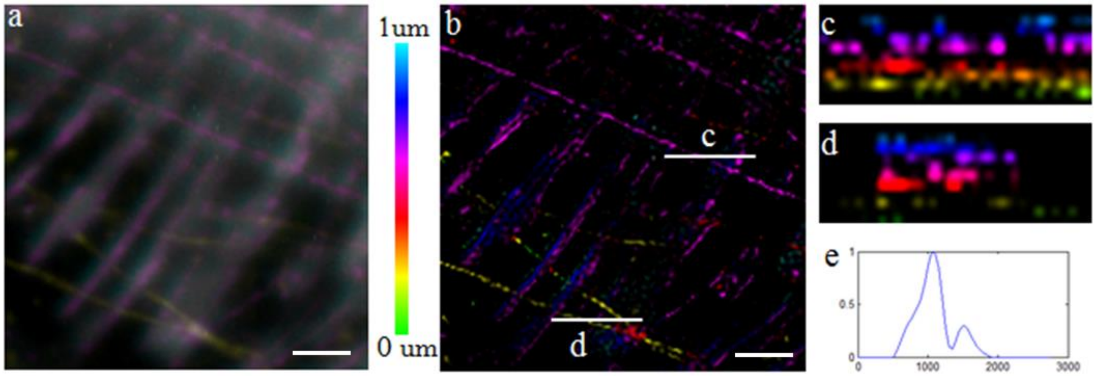

Figure 27 – 3D-SDOM imaging results of actin in fixed cell sample.
(a) 3D wide field image with depth coded pseudo color. (b) 3D-SDOM super resolution image with depth coded pseudo color. (c, d) Cross-sectional image of the line indicated in (b). (e) z-axis intensity profile plotted on (c), which shows 400 nm axial resolution. Scale bar: 2 um.

3.3 DISCUSSION

Applying optical lock-in detection with SDOM, SLIDOM improves the power of fluorescence polarization measurement in the situation of low signal-to-noise ratio. Compared to conventional OLID with on-off modulation of the fluorophores, SLIDOM is easier to set up due to natural modulation of linear dichroism. However, this makes SLIDOM not applicable for samples which have polarization variant background. Similar to SDOM, SLIDOM couldn't be applied to samples with a homogeneous distribution of fluorescent dipoles or densely random labeled samples.

For 3D-SDOM technique, the 3D polarization modulation data is acquired by z-scanning, which requires a much longer time (~min). Since the imaging model hypothesizes static dipole orientation of the fluorophores, the application of 3D-SDOM is quite limited for live cell imaging. Simultaneous 3D imaging techniques would be introduced in the future, including the multi-plane imaging[79] or multi-focus imaging[30].

Currently, 3D-SDOM only achieves 3D imaging of intensity image, while the dipole orientation remains 2D measurement. The technique could be termed as 'true 3D SDOM' only if the out-of-plane tilting angle of the dipole is measured together with 3D imaging of the sample, which also remains to be future work.

CHAPTER 4. OTHER WORK DURING GRADUATE PERIOD

This Chapter includes my two side projects during graduate: Light Field Microscopy (LFM) and protein binding kinetics on cell membranes. LFM is a technique inspired by the compound eye the insects, which enables one-shot 3D imaging. Two setups of LFM were built for different purposes, as shown in the following context. I spent my time from 2016.01 to 2017.01 at Georgia Institute of Technology, U.S., as a joint Ph.D. student. I was under the guidance of Dr. Cheng Zhu there, who is a famous expert in cell mechanics. My study was to measure protein binding kinetics utilizing optical imaging methods. Fluorescence Recovery After Photobleaching (FRAP) and Fluorescence Correlation Spectroscopy (FCS) are applied.

4.1 WORK RELATED TO LIGHT FIELD MICROSCOPY

The light field is a vector function which contains both the intensity and propagation direction of the light at every point in space. The 5D plenoptic function could fully describe a light field with rays in space parameterized by spatial coordinates x, y, z and angular variables θ, ϕ[80]. The 5D plenoptic function consumes much computational power and is hard to apply. 4D light field reduces the plenoptic function to four dimensions, which describes a light ray by two points on two separate planes[81]. Light field technique could be easily applied to imaging and microscopy with the use of a micro lens array[30,82-96] or other setups[97]. A micro lens array is an optical element mimicking the compound eye of the insects. It contains thousands to millions of small lenses, which are arranged disciplinary. The Light Field Microscope could be built based on a wide field microscope by incorporating a micro lens array at the intermediate plane and placing the camera on the focal plane of the micro lens array[93,98]. LFM was applied to both bright field with transmitted illumination and fluorescence imaging with epi-illumination[91,98]. Though its capacity to record 3D imaging at one shot, the major drawback of LFM is its low resolution, which is balanced against the imaging depth[90]. 3D deconvolution with wave optics theory of LFM could be applied to improve the resolution, with the same imaging depth reserved[82]. Alternative methods for the resolution improvement of LFM have been proposed as well[92,95]. In 2014, LFM was applied to simultaneous whole-animal 3D imaging of neuronal activity[93]. The technique achieved the power to capture neuronal activities in volumes of ~700 um * 700 um * 200 um at 20 Hz at single neuron resolution. It was demonstrated in imaging the neuronal system in a whole body of C. Elegans and in the head of a zebrafish. Fast 3D imaging speed and easy accessibility make LFM an attractive tool for neuronal imaging. During my work, two different LFMs were set up. The first one aimed at fast volume imaging at the resolution of single neurons. The second one is a high-resolution LFM setup with only ~ 2 um imaging depth. The high-resolution LFM is combined with STochastic Optical Reconstruction Microscopy (STORM), for 3D super resolution single molecule imaging and tracking.

The re-focusing process based on the plenoptic function is limited to geometric optics and its resolution and imaging depth is decided by both the objective and the MLA. The resolution (R_{xy}) of the light field is limited by the sampling rate and determined the pitch size (P) of the MLA and the magnification (M) of the objective: $R_{xy} = P / M$. The imaging depth of field D_z is related the number of resolvable spots within each micro lens array:

$$D_z = \frac{(2 + N_{uv}^2)\lambda n}{2NA^2} \qquad \textbf{Eq. 21}$$

where λ is the wavelength of emitted fluorescence, n is the refraction index of the medium and NA is the numeric aperture of the objective. N_{uv} is the number of resolvable spots, which could be calculated by:

$$N_{uv} = \frac{P * NA}{0.47\lambda * M} \qquad \textbf{Eq. 22}$$

4.1.1 System Setup and Calibration

The setup is implemented on a commercial Nikon Ti-U inverted microscope. The Nikon objective is 40 X 0.6 N.A.. The micro lens array is placed on the intermediate image plane. The focal plane of the micro lens array is imaged by a Nikon micro lens and conjugated with the detector. The detector is a scientific CMOS camera (Andor Zyla 4.2), which has the advantage of more pixels and larger field of view. LFM setup needs to pay special attention to the F number matching between the objective and the micro lens array[98]. The micro lens array here for fast volumetric imaging is purchased from Thorlab with 150 um pitch size and 5.2 mm focal length. The setup for single molecular imaging contains a different objective of Olympus 100X 1.4 N.A. objective and a micro lens array of 100 um pitch size and 5.1 mm focal length. The position of the micro lens array is critical for the performance of light field imaging. To guarantee the precise location of the micro lens array, a 5-xis kinematic mount[93] or well-designed cage system (Figure 28) could be used.

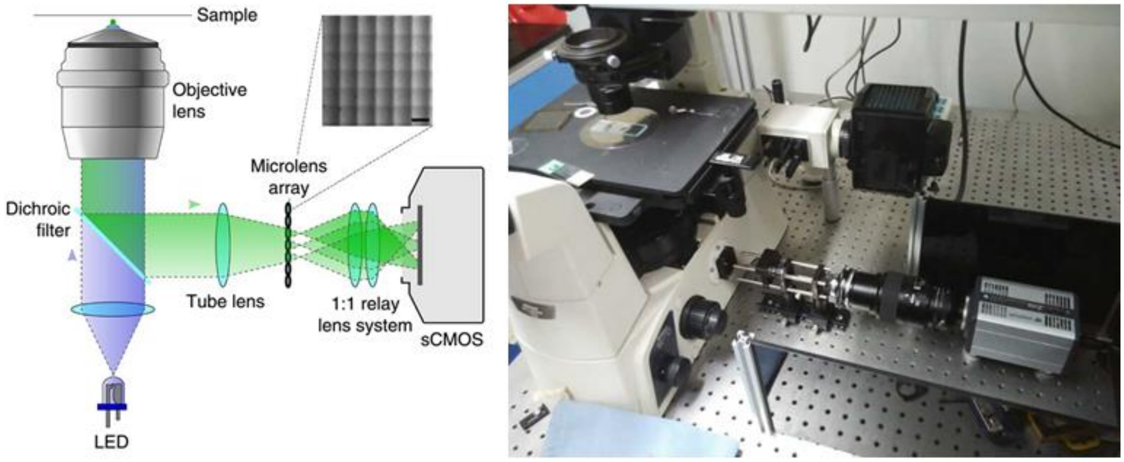

Figure 28 – Schematic setup and photo of home built light field microscope. (Left) Schematic setup of a light field microscope with a micro lens array. Figure adapted from [93] (Right) The photo of home-built light field microscope with cage structure.

The steps of system calibration are as follows. The first step is to calibrate the wide field imaging system with the relay lenses, by removal the micro lens array. The camera is then moved another distance of the focal length of the micro lens array. After that, the micro lens array is placed roughly on the focal plane of the relay lenses so that it will be imaged directly by the camera. The micro lens array would be roughly on the intermediate plane when moving a distance of its focal length toward the tube lens. To precisely locate the micro length array, a parallel light is applied by adjusting the Koller illumination path of the bright field imaging. A z-axis kinematic mount is used for finely adjusting the z location of the micro lens array until the focal spot of the micro lenses achieves the highest intensity. Finally, a fluorescent bead sample would be imaged and reconstructed, resulting in 3D PSF measurement of the light field system.

4.1.2 Reconstruction Algorithm of LFM

Before reconstruction, the light field images should be registered at first, since the micro lens array could be placed just right for every pixel of the camera. Sub-pixel registration of the light field image would convert it into the 4D light field data. Once the LFM is set up and calibrated, a special image is acquired for registration with over-exposure illumination. The grids of the micro lens array could be measured from the image and the parameters of x-y translation and image rotation for registration are obtained. For each light field image, the registration parameters are applied for image translation and rotation with bilinear interpolation.

The registered light field contains an array of sub images corresponding to the micro lenses. The whole intensity of every sub image is related to the intensity of a pixel in the x-y image, while every pixel in the sub image is related to the direction of light. Thus, the 4D plenoptic function $L(x, y, u, v)$ could be extracted from the registered image, which denotes a light ray passing the point (x, y) in the intermediate image plane with direction (u, v) has the intensity of L. The plenoptic function $L(x, y, u, v)$ contains full information of the 3D sample, from which orthogonal view image and re-focused image at different depth could be obtained. The re-focused image could be calculated by the following formula:

$$\begin{aligned} &L_{\alpha F}(x,y,u,v) \\ &= L_F(u+(x-u)/\alpha, v+(y-v)/\alpha, u, v) \\ &= L_F(u(1-1/\alpha)+x/\alpha, v(1-1/\alpha)+y/\alpha, u, v) \end{aligned} \quad \textbf{Eq. 4.1}$$

Where L_F denotes the light field on the plane of the focal plane and $L_{\alpha F}$ denotes the light field on the plane at the distance of αF. The image at the re-focused plane F' could be calculated by integrating the angular coordinate (u,v):

$$I_{F'} = \sum_u \sum_v L_{F'}(x,y,u,v) \quad \textbf{Eq. 4.2}$$

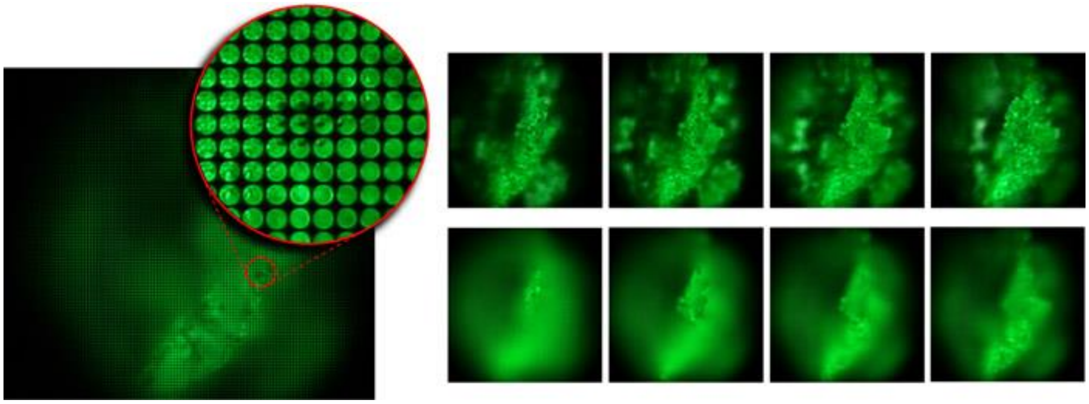

Figure 29 – Typical image results of light field microscopy.
(Left) A light field image of a speck of fluorescent crayon wax. The image consists of 170x170 sub images, one per micro lens, each depicting a different part of the specimen. An individual sub image contains 20x20 pixels, each representing a different point of the objective lens and hence a unique direction of view of the specimen. (Right) Perspective views of the specimen are shown at top-right, by extracting one pixel from each sub image. The sample could be the focus at different depths by summing the sub images after shearing the light field, as shown at the bottom-right. Figure adapted from [98]

The re-focusing method based on geometric optics is limited in resolution, barricading the application of LFM. To further improve resolution, a wave optics based optical model for LFM is presented, together with a 3-D deconvolution methods for higher spatial resolution of reconstruction volume. Dense spatio-angular sampling is taken advantage of, which is provided by a micro lens array at axial positions away from the native object plane.

$$h(x,p) = \mathrm{F}^{-1}\left\{ F\left\{ \Phi(x) U_i(x,p) \right\} \exp\left[-\frac{i}{4\pi} \lambda f_{mla} (\omega_x^2 + \omega_y^2 \right] \right\} \qquad \textbf{Eq. 4.3}$$

Maximum Likelihood Estimation could be used for estimation of the sample and background.

4.1.3 LFM with fast volumetric imaging

Fast speed LFM is equipped with micro lens array with 150 um pitch size and 5.2 mm focal length and 40X 0.6 N.A. objective. The sample rate of intensity image is $R_{xy} = P/M = 150um/40 = 3.75um$ and the imaging depth is ~ 100 um. Since the refocusing is achieved via 3D deconvolution based on wave optics modeling of the system, the resolution could be further improved by around three times. Hence, the final lateral resolution is ~ 1.5 um and the axial resolution is ~ 4 um at z=10 um according to the imaging results of fluorescent beads. The imaging resolution of LFM is not uniform and is related to the imaging depth. The resolution is lower at the focal plane or two far away from the focal plane.

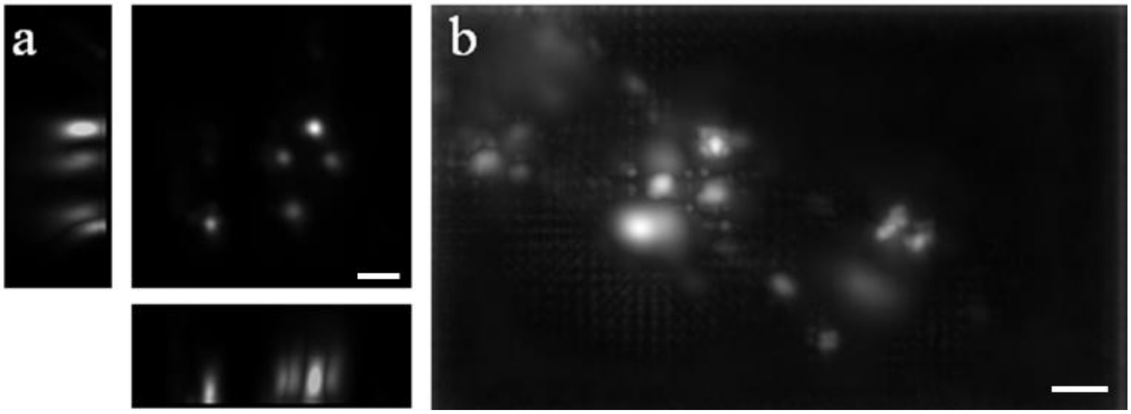

Figure 30 – Imaging results of high-speed LFM.
(a) 3D reconstruction results of fluorescent beads at z=10 um. Xy, xz, and yz sectional image is included. (b) 3D reconstruction results of GCaM labeled neurons of C. elegans with Maximum Intensity Projection (M.I.P). Scale bar: (a) 5 um; (b) 10 um;

Fast volumetric imaging with LFM is a power tool for real-time imaging of neuronal activities. To demonstrate this, we asked Dr. Tao Xu and Dr. Haining Zhang in Institute of Biophysics, Chinese Academy of Sciences for help with the sample preparation. Neurons of live C.elegans is labeled with GCaM fluorescent proteins, which will emit fluorescence at neuronal spikes. To keep the worm static for imaging, they are narcotized temporally. For better imaging resolution, the worm was placed ~ 30 um off the focal plane. The imaging results are displayed in Figure 30 b.

4.1.4 High Resolution LFM with 3D super resolution imaging

For high-resolution LFM, we chose micro lens array with 100 um pitch size and 5.1 mm focal length. The objective used is 100X 1.4 N.A. with oil immersion. An additional 2X optical relay lens is used to match the F number of imaging path and the micro lens array. The setup results in a final sampling rate of $R_{xy} = 500nm$ and the image depth of ~ 1.5 um. Since the typical imaging spot of a single fluorescent molecule would spread with a diameter of 600~1000 nm, it could be imaged by as many as four micro lenses, thus could be localized through the Gaussian fitting. The axial position could be decided by the intensity distribution within each micro lens. A 3D deconvolution method is utilized for 3D localization. The PSF of the light field imaging system is needed, which could be calculated by the wave optic model. Unlike wide field imaging systems, light field PSF is related with spatial coordinates x, y, z (Figure 31 a).

To test the system, single molecular samples of Alexa 647 is prepared. The dye is diluted to an appropriate concentration in PBS. An imaging channel is prepared and washed. During imaging, specific imaging buffer for single molecular imaging is added, which is a gift from Dr. Peter Q. Su and Miss. Rongqin Li from Biopic, Peking University. The excitation is a 647 laser with an objective power of 30 mW. 50 ms exposure time is taken and 1000 frames were acquired and localized. The reconstructed imaging is displayed in (Figure 31 b). Since light field based localization is based on a 3D manner, it allows higher labeling density of the fluorophores and has the potential to achieve fast 3D imaging speed.

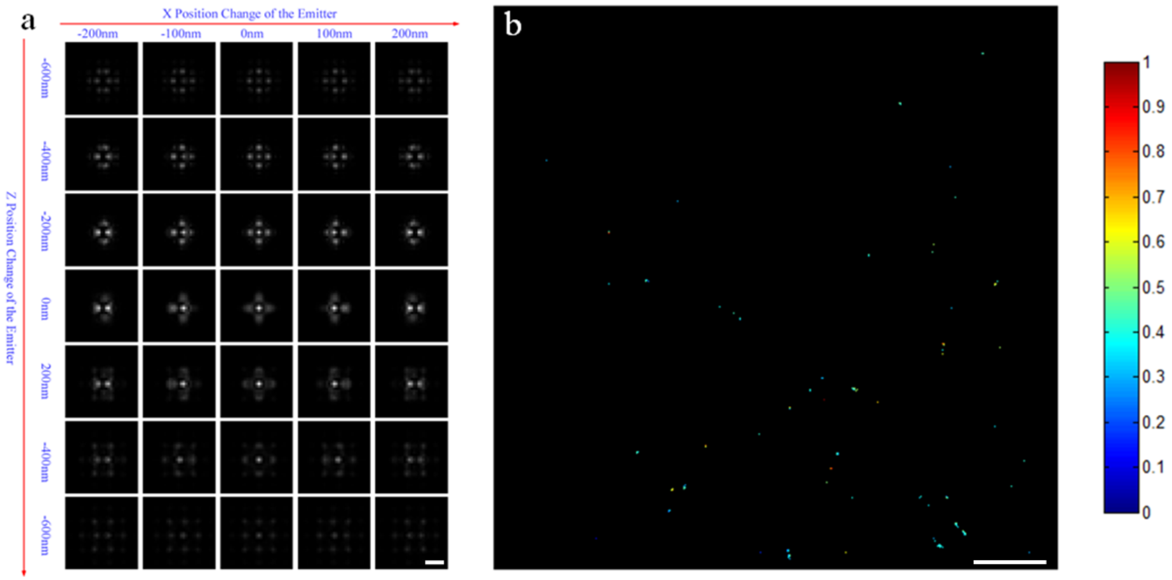

Figure 31 – 3D PSF of high resolution LFM and its imaging results of single molecules. (a) Calculated 3D PSF of the light field system at different positions. (b) 3D localization results of Alexa 647 single molecules, with the axial position represented in pseudo color. The total imaging depth is 1 um. Scale bar: (a) 1 um; (b) 5 um.

4.2 BINDING KINETICS OF PROTEINS ON CELL MEMBRANE

Binding kinetics of proteins on the cell membrane is highly related to cellular functions and dynamics, which is investigated by various techniques: single particle tracking, FRAP, FRET, etc. Fluorescence Correlation Spectroscopy (FCS) and Fluorescence Cross Correlation Spectroscopy (FCCS) are quantitatively and statistically, methods to measure diffusion coefficients and binding affinities of the fluorescent labeled proteins, either on the cell membrane or within the cell. The fluorescence intensity fluctuations are analyzed by FCS or FCCS to determine the molecular processes causing these fluctuations, which is typically diffusion of particles into and out of the focal region. The correlation functions could be used to analyze these random fluctuations, which is calculated using the intensity time trace I(t):

$$G(\tau) = \frac{\langle \delta I(t) \bullet \delta I(t+\tau) \rangle}{\langle I \rangle^2}$$ **Eq. 4.4**

where $\langle I \rangle$ is the time-averaged intensity, $\delta I(t)$ is the intensity fluctuation, and $G(\tau)$ is the correlation function. The diffusion coefficient D could be extracted from the half decay time τ_D of the correlation function by an empirical equation:

$$\tau_D = \frac{A_{eff}}{4D} \text{ with } A_{eff} = \frac{(\int\int MDE(x,y,0)dxdy)^2}{(\int\int MDE^2(x,y,0)dxdy)}$$ **Eq. 4.5**

where the molecular detection efficiency (MDE) describes the observation volume and A_{eff} is the area of a section through the center of the MDE.

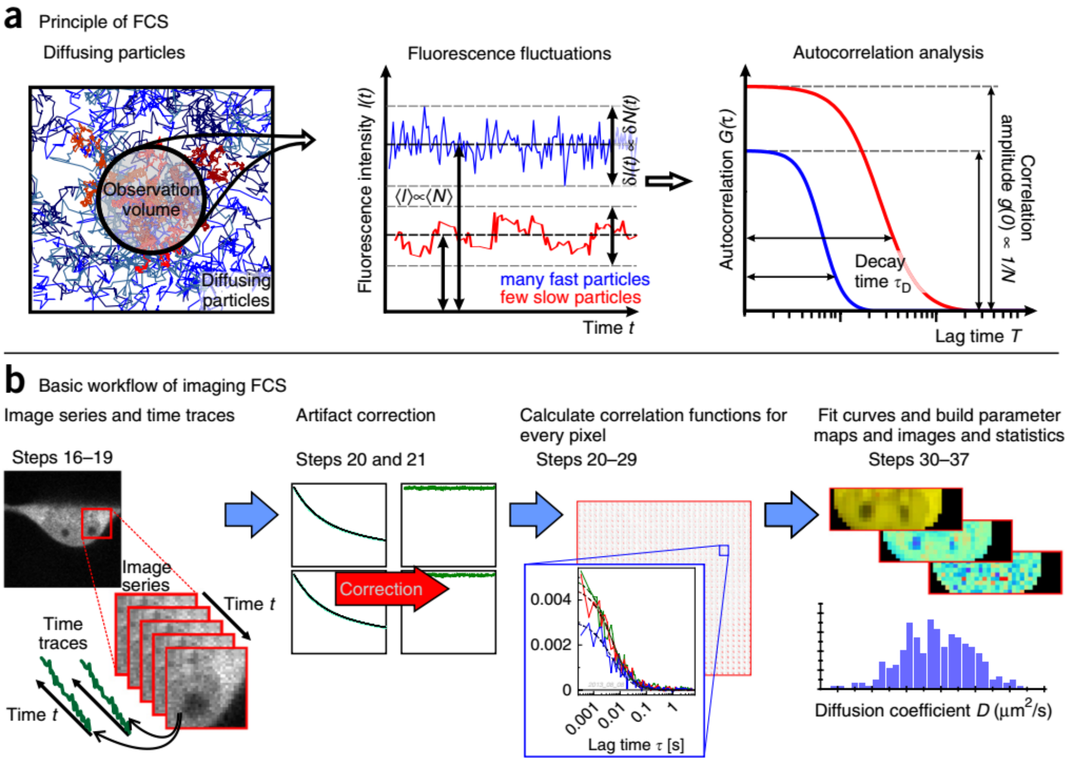

Figure 32 – Principle of FCS and imaging FCS.
(a) Particle diffusion through the observation volume causes the intensity fluctuation, which could be analyzed by the autocorrelation function. (b) Imaging FCS acquires a time series of the image stack. By applying autocorrelation analysis to each pixel, the diffusion coefficient is obtained in every pixel. Figure adapted from[99]

The FCCS is an extension of FCS, which analyzes the fluorescence fluctuations from two types of fluorophores with different emission wavelength. The cross correlation function G_{gr} is described as:

$$G_{gr}(\tau)=\frac{\langle \delta I_g(t)\bullet\delta I_r(t+\tau)\rangle}{\langle I_g(t)\rangle\bullet\langle I_r(t)\rangle} \qquad \textbf{Eq. 4.6}$$

where the subscripts g and r denote different fluorophores. The higher dependence between two types of fluorophores result in higher cross-correlation function, which could be quantitatively described by the equation:

$$G_{gr}(0) \propto \frac{N_{gr}}{(N_g + N_{gr}) \bullet (N_r + N_{gr})} \qquad \textbf{Eq. 4.7}$$

where N_{gr} is the number of bound g and r fluorophores, and N_g, N_r is the number of independently diffused fluorophores.

Earlier FCS/FCCS imaging is implemented on confocal based microscopes[100,101], which has no spatial resolution. Due to the increasing imaging speed of detecting cameras, imaging FCS has been invented. The time traces are measured in image series instead of a single point. After applying autocorrelation analysis, the parameter of the image could be achieved, including the diffusion coefficient, binding affinity, etc.

4.2.1 SLB and Cell Preparation

The binding kinetics between CD32A and IgG is studied in the research. The biological samples are firstly prepared. The CHO-CD32A-YFP cell line is a gift from other labs. The DNP and DOPC liposome is purchased from Avanti. The liposomes are extruded to get uniform sizes with a diameter of 50 ~ 200 nm. After that, they are put on the cover glass for incubation. When the supported lipid bilayer is formed, Anti-DNP labeled IgG is put on the supported lipid bilayer. Then, the Cy5 solution is used to label IgG. In the end, the cells are placed on the lipid bilayer for measurement.

The preparation of supported lipid bilayer (SLB) is critical for the experiment. It often happens that SLB contains immobile parts or fractions with low mobility. Since FCS measurement contains an integral of all the diffusion particles, these immobile particles will influence the results measured. The FRAP test in next section could test the mobility of the SLB. To guarantee the high quality of prepared SLB, the concentration of each reagent needs special attention. After trial and error, the portion of DNP in DOPC is 0.1% and the concentration is ~0.6 mg/ml in final incubation of SLB. The concentration of antibody is 0.1~10 uM.

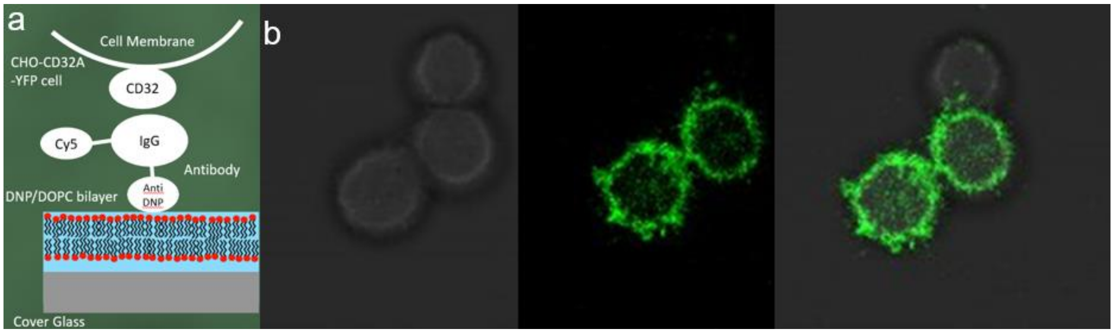

Figure 33 – Biological system of the research.
(a) Schematic illustration of the biological system used (not to scale). Supported lipid bilayer of DNP and DOPC is formed on cover glass. Anti-DNP labeled antibody IgG binds to the DNP component of the lipid bilayer. CHO-CD32A-YFP is put on the lipid bilayer, whose CD32A portion would bind IgG. The antibody IgG is also labeled with Cy5 for FRAP and FCS measurement. (b) The CHO-CD32A-YFP cell is put on the lipid bilayer and imaged. From left to right: wide field image, fluorescent image, and composite of them.

4.2.2 FRAP and FCS measurement of SLB

FRAP measurement is used to check the quality of the SLB. FRAP is performed by applying a strong bleaching laser to bleach the Cy5 in the area of interest, usually within a circle with a diameter of 10 um. Then the fluorescence recovery due to diffusion is recorded as an image stack. After photobleaching correction, the diffusion coefficient and immobile percentage could be extracted. The intensity trace of the fluorescence recovery could be fitted as an exponential curve, and the immobile percentage and diffusion coefficient could be calculated by the formula:

$$F_m = \frac{I_E - I_0}{I_I - I_0}\ ,\ F_i = 1 - F_m$$

Eq. 4.8

$$D = 0.224\frac{r^2}{\tau_{0.5}}$$ [102]

F_m and F_i is the mobile percentage and immobile percentage. I_E is the intensity of the recovered fluorescence, I_I is pre-bleach fluorescence intensity, and I_0 is the first post-bleach fluorescence intensity. D is the diffusion coefficient of IgG, r is the radius of the bleaching area, and $\tau_{0.5}$ is the half recovery time. A typical result of FRAP test is displayed in Figure 34.

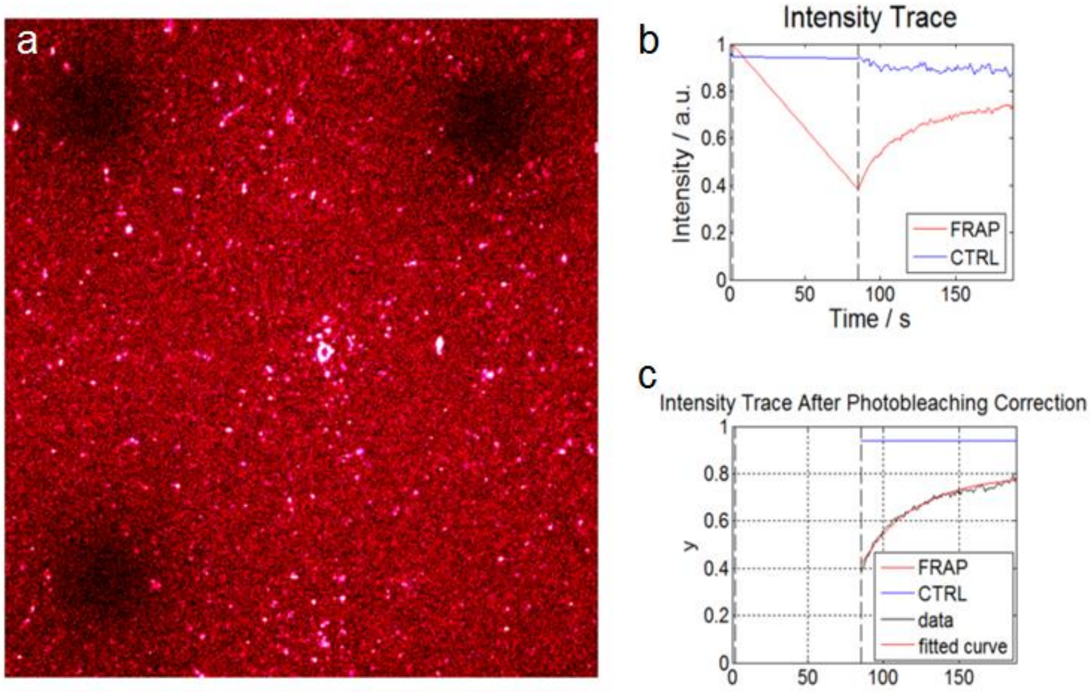

Figure 34 – FRAP measurement of SLB.
(a) Fluorescent image of Cy5-IgG on SLB after bleaching in three circular areas. (b) Intensity trace during the whole process. (c) Intensity trace after photobleaching correction and exponential fitting of the trace.

After the SLB of good quality is prepared, FCS is used to measure the diffusion coefficient of both the antibody IgG and the protein CD32A as well as their binding affinity. Unfortunately, only FCS measurement on IgG is performed. FCS requires an appropriate labeling density of 1-10 /um^2, which could be adjusted by changing the solution concentration of Cy5 dyes. The FCS experiments are performed on a commercial Nikon Ti-E system with motorized TIRF module. The time series image is acquired by an EMCCD. The objective used is 100X 1.49N.A. Nikon TIRF. Only a small area is imaged to achieve fast imaging speed of 200 f.p.s. The dataset is recorded as suggested by QuickFit

3① and analyzed by the same software to obtain the diffusion coefficient. Currently, the FCS outcome is inconsistent with FRAP measurement and troubleshooting of the issues remains to be future work.

---

① For more details, please refer to the website: https://www.dkfz.de/Macromol/quickfit/

CHAPTER 5. CONCLUSION

FPM could measure the dipole orientation of fluorophores, which is related to the structure and function of the biological macromolecules. Traditional FPM is barricaded by its resolution, which influences not only the intensity image but also the detection accuracy of the dipole orientation. The major part of the dissertation is to achieve super resolution dipole orientation measurement via polarization modulation or linear dichroism (chapter 2) and its further improvements (chapter 3). Compared to conventional diffraction limited FPM, SDOM improves the resolution to ~150 nm as well as a much more accurate dipole orientation measurement. Together with a novel OLID modeling of the system, the imaging resolution of SDOM is further improved. Since most biological samples contain 3D structures, 3D-SDOM is demonstrated in principle by z-scanning of the sample, with super resolution of axial intensity image. In this chapter, we would include a comparison between SDOM and other FPM techniques as well as its potential application. The future research plan is also proposed aiming at overcoming current limitations of SDOM.

5.1 COMPARISON BETWEEN SDOM AND OTHER FPM TECHNIQUES

Diffraction limited FPM techniques are generally applied to imaging bulk samples with organized distribution of dipole orientations. Taking the study of septin, for example, both early research and FluoPolScope could only reveal the 90° rotation of the filament direction[27-29]. As for the intermediate state, during which the filament direction transits, they could hardly do anything and requires higher resolution imaging[103]. What's worse, the results true for the bulk sample may be completely wrong for single fluorescent probes[3,72], making the measurement results unreliable.

Recently developed super resolution FPM techniques could be categorized into two group: one is based on intensity modulation of LD[31,72] and the other one is to combine FA with direct stochastic optical reconstruction microscopy (dSTORM)[3]. SPoD and SDOM belong to the first group and the other super-resolution technique is based on single molecular imaging.

Single molecular imaging of fluorescent dipoles in intensity and orientation has long been investigated[13,18,21,51]. For LD single dipole measurement, two or four polarization excitations are modulated for the balance of dipole orientation measurement and imaging speed[18,37]. Simultaneous imaging brings FA the advantage over LD of faster imaging. However, splitting the fluorescent signal into multiple detection channels would reduce the signal-to-noise ratio, thus limiting the number of detection channels. In most cases, two detection channels are used. Four channels could achieve 3D orientation detection[20] or unambiguous measurement of the dipole's average orientation and wobbling angle[21]. However, this only applies to the very diluted labeling of fluorophores and could hardly reveal complex bio-structures. This could be solved by polarization-resolved direct stochastic optical reconstruction microscopy (polar-dSTORM)[3], which measures single fluorescent dipoles in one frame, and switches to other dipoles on the ON state stochastically in other frames, accumulating a full picture of the samples from adequate frames.

To reserve high signal-to-noise ratio for single molecular localization, two emission detection channels were used, which allows in-plane orientation measurement only and omits the wobbling information of single dipoles. The designed algorithm estimates both the azimuth and the position of the single molecules in each frame, which provides accurate localization and orientation measurement. With single molecular detection in polar-dSTORM, the dipole information measured includes the average orientation of the dipole and the wobbling aperture angle. The average orientation of the dipole could be measured directly from the fluorescence anisotropy in each frame, while the wobbling aperture angle is statically calculated from nearby localized emitters. Previous FPM images could only offer an average of orientation information over many molecules, which would lose information on individual wobbling behaviors at some extent. It was found that the average orientation may remain the same in ordered and disordered system while their wobbling angle varies. Polar-dSTORM was applied to nanoscale orientational order imaging of biological filaments, including dsDNA, actin, and microtubule, providing quantitative results of point orientation and wobbling angle. Since the imaging time of polar-dSTORM takes 2-40 min and statistical calculation of molecules detected during the period is used, it fits better for stationary samples. The specific sample preparation of polar-dSTORM also limits the application of live cells.

In comparison with polar-dSTROM, SDOM still measures average dipoles and could not separate the signal of the wobbling of single fluorophores from the variation of orientation distribution of fluorophores with the resolvable area. A comparison of actin imaging results among SDOM, polar-dSTORM, and instantaneous FluoPolScope are displayed in Figure 35. However, the super resolution power of 150 nm allows SDOM a much better dipole orientation mapping ability than diffraction limited FPM techniques. Its sub-second temporal resolution make SDOM applicable to both fixed cell and live cell imaging, which shows great advantages polar-dSTORM.

As a general super resolution imaging technique, SDOM is competitive compared to the temporal resolution of PALM/STORM (at the level of several minutes) and the spatial resolution of SIM (>150 nm), which are not sufficient to fulfill expectations, and the power of STED (25-100 mW focused light) may potentially inflict photo damage on the specimen. Achieve dipole orientation information at sub-diffraction resolution and a speed of 5 frames per second, SDOM will attract immediate interest with regard to the super-resolution study of highly dynamic cellular processes.

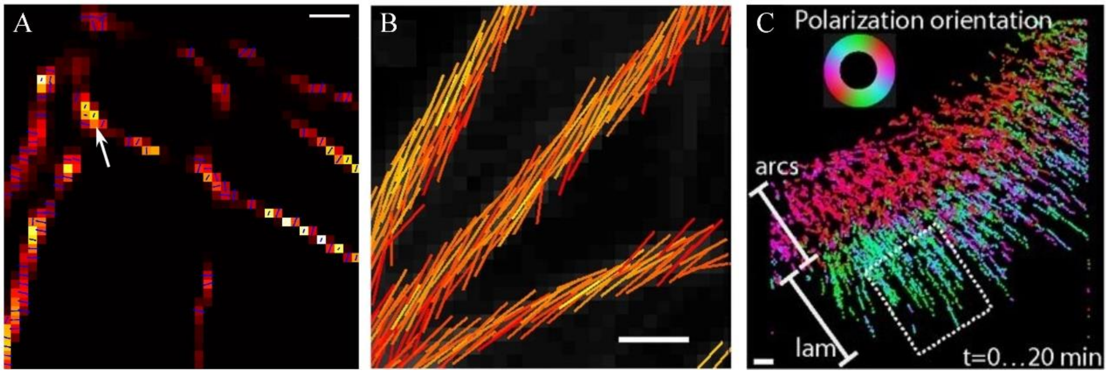

Figure 35 – Super resolution dipole measurement on actin samples.
(A) SDOM results of actin in fixed cells. The dipole orientation is marked with arrows on each pixel. (B) Polar-dSTORM results of actin in fixed cells. (C) Tracking results of instantaneous FluoPolScope of actin in live cells. Scale bar: A, 200 nm; B, 1.5 um; C, 1 um. Figure adapted from [3,21]

Table 1 – Comparison between selective fluorescence polarization microscopy techniques

SR-FPM techniques	Representative Literatures	Basic Principle	Advantages	Limitations
FluoPolScope	[29,30]	LD with wide field	Relative fast speed (0.2 f.p.s); 3D imaging with multi-focus imaging	Diffraction-limited imaging; Ensemble orientation;
polTIRF	[18,37]	LD and FA with Total Internal Reflection Fluorescence Microscopy	Combination of LD and FA; Fast imaging speed (25 f.p.s); Tilting angle measurement	Limited to dilute labeling (or diffraction-limited imaging)
2PPM	[5,32]	LD with two-photon confocal	Narrow polarization excitation via two-photon absorption; Optical sectioning of confocal	Diffraction-limited imaging; Ensemble orientation;
DOPI	[13]	DPR	3D orientation measurement; Fast tracking (1.5 f.p.s);	Limited to dilute labelling
Instantons FluoPolScope	[21]	FA	Unambiguous measurement of in-plane orientation; Fast tracking (10 f.p.s);	Limited to dilute labelling (or diffraction-limited imaging)
Polar-STORM	[3]	FA; SR via dSTORM	Super resolution imaging with localization precision of 30 nm; Measurement of single dipole orientation and wobbling;	Long imaging time (2-40 min)
SPoD with ExPAN	[31]	LD; SR via polarization demodulation	Narrow polarization excitation via stimulated depletion; Fast SR imaging (3 f.p.s);	Unable to measure dipole orientation
SDOM	[72]	LD; SR via polarization demodulation	Super resolution measurement of intensity and dipole orientation; Fast SR imaging (5 f.p.s.);	Ensemble orientation

5.2 POTENTIAL APPLICATIONS OF SDOM

FPM measures the dipole orientation, as well as the intensity of fluorescent probes, could be measured. Since the orientation of the fluorescent molecule is related with the tagged biostructures, structural information of cellular organelles or macromolecules can be revealed. Although X-ray crystallography or electron microscopy could elucidate ultra-high resolution of individual proteins or macromolecule assemblies, they require very complex sample preparation unsuitable for live cell imaging. Near field imaging techniques, such as Atomic Force Microscopy (AFM) could also achieve structural information, which, however, is limited only to samples on the surface. FPM is able to image orientations in dynamic samples at the time scale of seconds or milliseconds, thus it can serve as a complementary method for measurement of subcellular organelle structures. Recent decades have seen a variety of application of FPM in the area of the cell membrane, biological filaments including cytoskeleton and DNA filaments, and other macromolecule assemblies.

The research of the structure and dynamics of macromolecule assemblies demonstrate FPM as a complementary method with X-ray crystallography or electron microscopy. The nuclear pore complex (NPC) perforates the nuclear envelope to facilitate selective transport between nucleus and cytoplasm, whose structures remain unsolved. With FPM, the Y shaped NPC sub-complexes were studied and their relative direction according to the nuclear envelope plane could be inferred from imaging results[75]. F-ATPase is a kind of enzyme relating to ATP synthesis. F-ATPase consists of two domains, of which the F1 motor was found to display 120° stepping by FPM[24,36,104].

Lipid membrane is generally locally uniform and provides a quasi-static environment for the fluorescent probes, the orientation of which could be easily measured[17,25,105]. With polarized fluorescence recovery after photobleaching (FRAP), rotational diffusion of the probes could be revealed[19,39]. Molecular orientation disorder in cell membrane has been found due to cholesterol depletion[32] or cytoskeleton perturbation[35]. Monitoring membrane proteins could also be used to observe dynamic protein activation during molecular processes such as calcium flow or protein interaction[5].

Cytoskeleton provides mechanical support to maintain or deform the cell shape and involves in many cell signaling pathways during cytokinesis. It also provides a scaffold to organize the contents of a cell in space and for intracellular transport with the motor proteins. Actin was first to be found to have an organized distribution of probed dipole orientations[14] and was imaged by various FPM techniques[3,21,31,72,106]. Myosin is an important motor protein moving along actin. It exhibits interesting walking pattern with steps and rotation and is an extensively studied system[13,18,107-110]. Kinesin is another type of motor protein which is bound to microtubules. A highly mobile state and a rigid sate of kinesin were distinguished which may relate to ATP and ADP binding[26]. Other types of cytoskeleton are also studied using FPM, including microtubule[3] and setpin[27-30,72]. Biological filamentous structures measured by FPM includes also in vitro DNA filaments [3,111] and human amyloid fibrils.[112].

Currently SDOM has been successfully applied to imaging cytoskeleton in both fixed cells and live cells, including actin and septin. It shows an advantage over diffraction limited FPM techniques on resolving both subdiffraction structures and dipole orientations. Compared to polar-dSTORM, SDOM demonstrates its power on live cell imaging. SDOM has been used to image NPC in live yeast cells. However, complementary techniques are required to study the structures of the bio-macromolecules, which is not included in current work. SDOM in correlation with cryo-EM would be a powerful technique in resolving the structure of bio-macromolecules. SDOM has not been applied to studying the fluorescence anisotropy of lipid membrane yet. One problem is that the fluorescence polarization is usually isotropic in the x, y dimensions. This may be caused by the random distributed fluorescent dipoles or fast wobbling of the dipoles. SDOM in combination with polarized FRAP or imaging FCS could be a better way to study the lipid membrane.

5.3 FUTURE PLAN

Though its success in imaging various samples, SDOM is still in its infancy. A lot of future work is needed for further improvement.

Firstly, the imaging quality of SDOM depends on the samples, which performs better on samples with strong polarization modulation and inhomogeneous distribution. This requires the condition that the dipoles are labeled on the quasi-static biological structures, with a relative rigid linker between the fluorophore and the target molecule. To solve the problem, we aim at improving both the hardware setup and the sample preparation. For the hardware setup of SDOM, current polarization modulation is spatially invariant, which would fail on samples with a homogeneous distribution of dipoles. A spatially variant polarization modulation would solve the problem and maybe provide further super resolution. For the preparation of samples, we need to test the rigidity of the linkers among different fluorescent labeling techniques and find those which are most suitable for SDOM.

Secondly, several technical performances of SDOM requires improvement. SDOM currently uses the mechanical rotary HWP to modulation the laser polarization, which limits the imaging time above sub-second scale. Using electro-optic modulator would greatly increase the imaging speed, which allows for dynamic imaging and reduces the influence from the motion of dipoles. Besides, the imaging speed of 3D-SDOM is much slower due to the z-scanning. It could hardly be applied to samples in live cells due to its slow imaging speed and its reliability is harmed by photobleaching or movement of the sample. Simultaneous 3D imaging would greatly increase the imaging speed via multi-focus imaging, multi-plane imaging or light field imaging. In addition, 3D-SDOM could only measure the in-plane 2D dipole orientation. 'True 3D-SDOM' would include both 3D intensity imaging and 3D dipole orientation measurement.

Thirdly, we intend to extend the application of SDOM to solve various biological questions, which have already been studied by traditional FPM. These areas include but not limited to studying the structure and dynamics of bio-macromolecule assemblies, lipid membrane, or cytoskeleton. To solve the biological questions, SDOM needs to combine with complementary optical imaging techniques and biological techniques.

For example, SDOM in correlation with cryo-EM imaging on in vitro or in vivo biological systems may become a powerful technique to solve the structure of macromolecules. SDOM in combination of with polarized FRAP or imaging FCS is a potentially powerful technique to study the fluorescence anisotropy of lipid membrane.

APPENDIX A. RECONSTRUCTION SOFTWARE

A.1 Manual of the SDOM Reconstruction Software

A.1.1 Step-by-Step Instruction

- Install Matlab (http://www.mathworks.com/ , R2012b, 2013b and 2014a have been tested).
- Download and install Anoconda (http://www.continuum.io/downloads), choose python 2.7 version.
- Download and unzip supplementary software from https://github.com/KarlZhanghao/SDOM (no special characters or space in the file pathway).
- Open Matlab from startup menu and Open './Code/ OMrecon.m'.
- Set parameters in 'Type parameters' (Uncomment the DateSet needing process and comment other DataSets); parameter description is in Part D.
- Click on 'RUN' button or press 'F5' to run this code; the whole processing will last for several minutes.

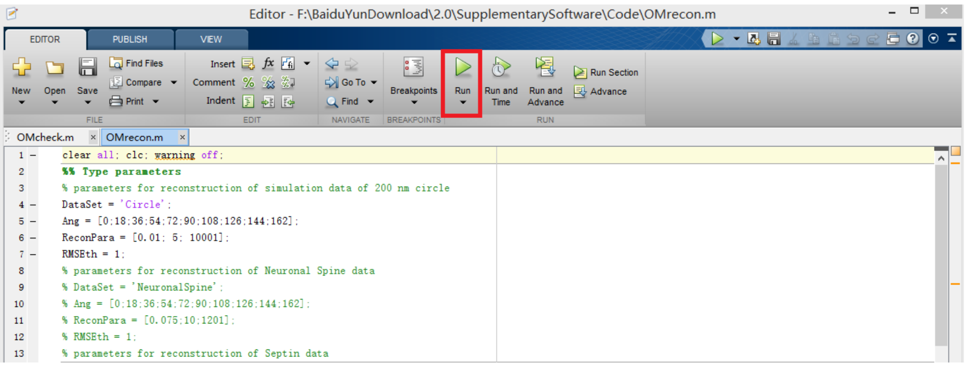

```
clear all; clc; warning off;
%% Type parameters
% parameters for reconstruction of simulation data of 200 nm circle
DataSet = 'Circle';
Ang = [0:18:36:54:72:90:108:126:144:162];
ReconPara = [0.01; 5; 10001];
RMSEth = 1;
% parameters for reconstruction of Neuronal Spine data
% DataSet = 'NeuronalSpine';
% Ang = [0:18:36:54:72:90:108:126:144:162];
% ReconPara = [0.075:10:1201];
% RMSEth = 1;
% parameters for reconstruction of Septin data
```

All the results are stored in './Data/DataSet/' and see "C. File Description" for details;

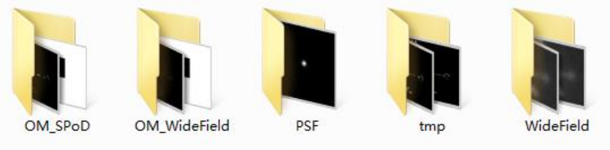

- 'OMcheck.m' can be used to check detailed fitting effects. Using Matlab open this file, this GUI would appear:

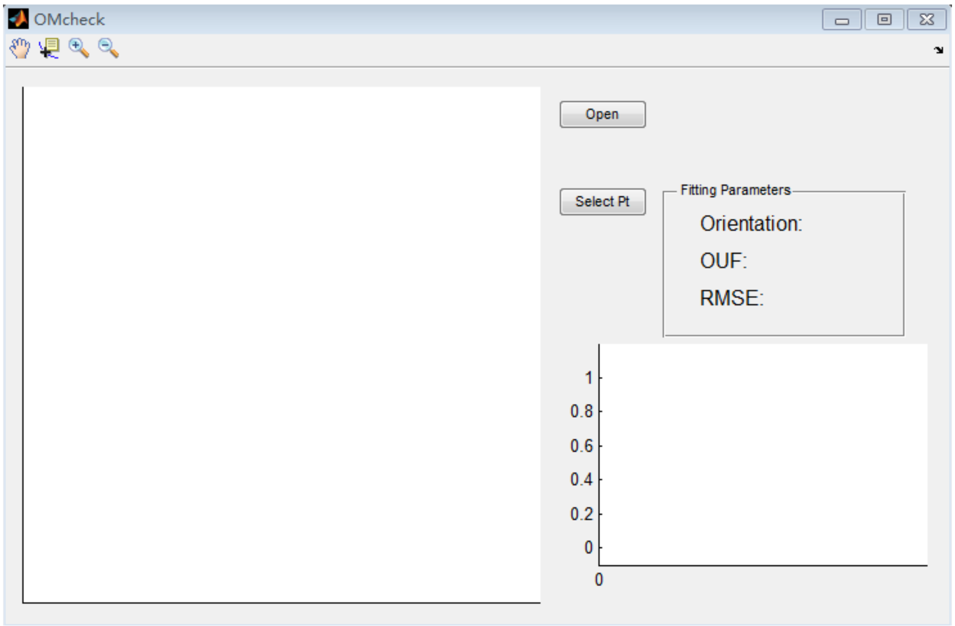

- Click ‘Open’ button, choose ‘./Data/DataSet/OM_SPoD/OM-SPoD_check.mat’

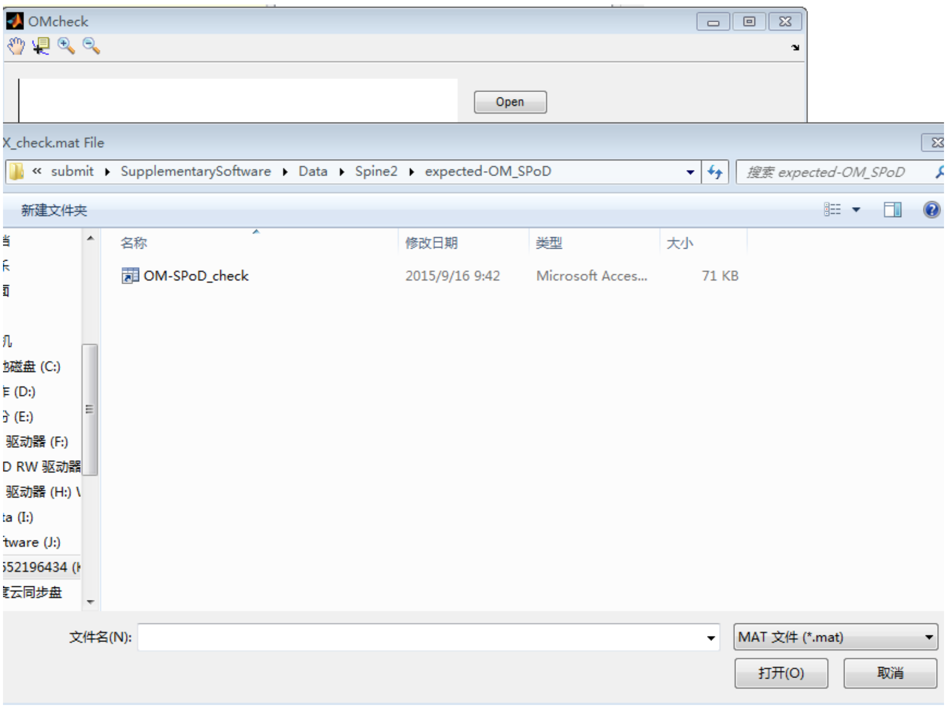

- Left-click ‘select pt’ button and RIGHT-CLICK on any point of the image, original modulation information and fitted curve would appear on the axes right

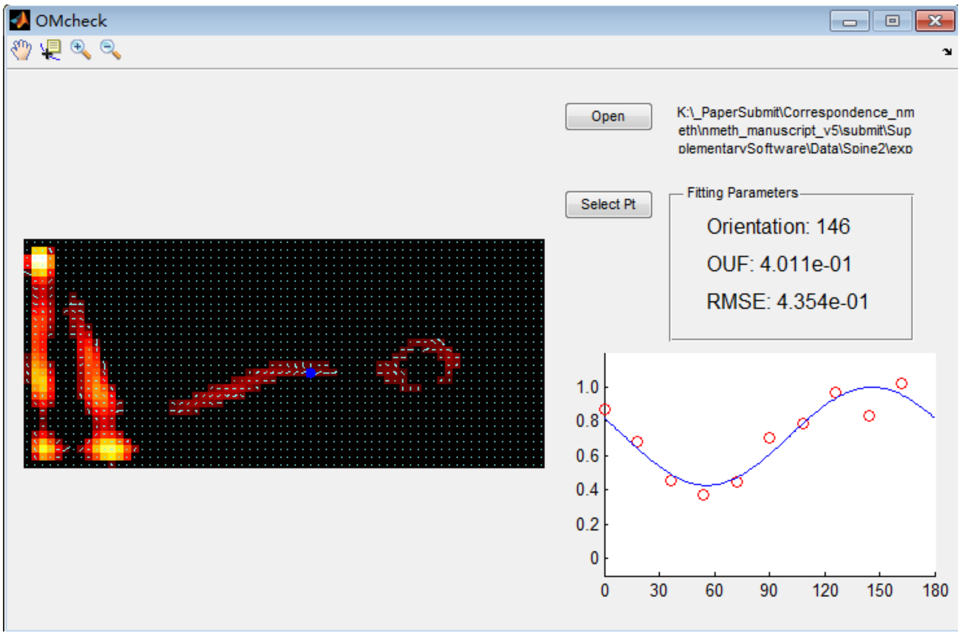

K:_PaperSubmit\Correspondence_nmeth\nmeth_manuscript_v5\submit\SupplementarySoftware\Data\Spine2\exp

Orientation: 146
OUF: 4.011e-01
RMSE: 4.354e-01

A.1.2 Installation

This software has been tested on Win 7 operating system with MATLAB (R2012b, 2013b and 2014a have been tested) and Python 2.7 with numpy, scipy, matplotlib installed. Matlab is a charged software, which, however, could be replaced by Octave (http://www.gnu.org/software/octave/, free software, NOT tested). Python is a free software which can be downloaded via internet. Here we choose Anaconda (http://www.continuum.io/downloads) for setting up the python distribution, which includes all the libraries needed to run our code.

A.1.3 File Description

- ‘./Data/DataSet/’:
    - ‘WideField’ and ‘PSF’ directory are data stored before running reconstruction program. They are original images captured by camera and point spread function of the system. All the images are in ‘.tiff’ format.

  - ‘OM_WideField’ directory stores orientation mapping results of original wide field images.
  - ‘OM_SPoD’ directory stores orientation mapping results of SPoD reconstructed images.
  - ’tmp’ directory is a run-time directory which can be ignored.
  - Five different data sets of sample data are provide to reproduce most figures in main text and supplementary information.
- ‘./Code/’:
  - ‘OMrecon.m’ is the main function to start the whole processing to obtain super resolution image and orientation mapping result.
  - ‘OMcheck.m’ and ‘OMcheck.fig’ are to visualize the orientation mapping analysis result.
  - ‘OM_SPoD.py’ is called in ‘OMrecon.m’ for OM-SPoD reconstruction.
  - ‘./Code/Util/’ contains function files to fit the reconstructed data and calculate orientations.

A.1.4 Parameter Description

- ‘DataSet’: this is a string, which is the same with the directory name in ‘./Data’.
- ‘Ang’: this is a vector, whose length is the same with the number of images. Each value means the polarization angle of incident laser when the image was acquired.
- ‘ReconPara’: this is 3*1 vector. First two parameters is regularization coefficients lambda1 and lambda2 in the optimization model. They are empirical parameters, set large lambda1 or small lambda2 to increase background level and vice versa. The third parameter is iteration number.
- ‘adjR2th’: threshold for adjusted R2.
- ‘vecZoom’: zoom factor for orientation mapping with wide-field image since their

OUFs are relatively small.

A.2 Key Codes for FISTA Algorithm

This part contains key codes for FISTA algorithm. FISTA is a powerful tool to solve optimization problem under sparsity constrains, which has been applied in SPoD and SDOM. The algorithm was first written in python code by Hafi et al.[31] . Since the SDOM program is written in MATLAB, here the algorithm is adopted in MATLAB code.

```
% initialize xk, yk, tk
g = zeros(g_shape);
b = zeros(img_shape);
b(1,1) = mean(img(:))*sqrt(img_shape(1)*img_shape(2));
xk = {g,b};
ykp1 = {g,b};
tkp1 = 1.0;
func0 = 0;
func1 = 0;
%% one iteration
for kk = 1 : n_iter
   xkm1 = xk;
   yk = ykp1;
   tk = tkp1;
   mu = forward(yk, psf, modulation, slice);
   grad = gradient(mu, img, psf, size(yk{1}), modulation);
   maxLikelihoodY = maximumLikelihood( mu, img);
```

```
    for jj = 0:1000
        ltest = lk*1.1^jj;
        xtest = step(yk, grad, ltest, lamb);
        new_mu = forward(xtest, psf, modulation, slice);
        newMaxlikelihood = maximumLikelihood(new_mu, img);
        quadratic = maxLikelihoodY + quadraticApprox(xtest, yk, grad, ltest);
        if newMaxlikelihood < quadratic
            xk = xtest;
            lk = ltest;
            break;
        end
    end
    tkp1 = 1+sqrt(1+4*tk*tk)/2;
    ykp1{1} = xk{1} + (tk-1)/tkp1*(xk{1}-xkm1{1});
    ykp1{2} = xk{2} + (tk-1)/tkp1*(xk{2}-xkm1{2});
    end
end
gtmp = xk{1};
figure
imshow(mean(gtmp,3), [])
stop = 1;

function xk = step( yk, grad, l_k, lamb)
tmp1 = max(yk{1}-grad{1}/l_k-lamb(1)/l_k, 0);
tmp2 = min(yk{1}-grad{1}/l_k+lamb(1)/l_k, 0);
xk{1} = max(tmp1+tmp2,0);
tmp3 = max(yk{2}-grad{2}/l_k-lamb(2)/l_k, 0);
```

```
tmp4 = min(yk{2}-grad{2}/l_k+lamb(2)/l_k, 0);
xk{2} = tmp3+tmp4;

function grad = gradient(mu, img, psf, xk_size, modulation)
tmp = 2*(mu-img);
grad = backward(tmp, psf, xk_size, modulation);

function grad = backward(h, psf, xk_size, modulation)
tmp1 = zeros(xk_size);
tmp2 = zeros(size(h,1), size(h,2));
for kk = 1 : size(h,3)
    tmp1(:,:,kk) = modulation(kk)*conv2(h(:,:,kk), psf, 'full');
    tmp2 = tmp2 + modulation(kk)*dct2(h(:,:,kk));
end
grad{1} = tmp1;
grad{2} = tmp2;

function mu = forward(yk, psf, modulation, slice)
g = yk{1};
b = yk{2};
b_ = idct2(b);
for kk = 1 : size(g,3)
    tmp(:,:,kk) = modulation(kk)*conv2(g(:,:,kk), psf, 'same');
    btmp(:,:,kk) = b_*modulation(kk);
end
mu = tmp(slice{1}, slice{2},:) + btmp;
mu = max(mu, 1e-6);
```

```
function maxLikelihood = maximumLikelihood( mu, img)
tmp = (mu-img).^2;
maxLikelihood = sum(tmp(:));

function quadratic = quadraticApprox( xk, yk, grad, lk)
delta1 = xk{1} - yk{1};
delta2 = xk{2} - yk{2};
tmp1 = delta1.*grad{1} + lk/2*delta1.*delta1;
tmp2 = delta2.*grad{2} + lk/2*delta2.*delta2;
quadratic = sum(tmp1(:)) + sum(tmp2(:));
```

A.3 Key Codes for SDOM Reconstruction

```
clear all; clc; warning off;
%% Type parameters
%
% parameters for reconstruction of 500 nm beads
% DataSet = 'Bead500nm';
% Ang = [42;26;10;174;158;142;126;110;94;78;62];
% ReconPara = [0.06; 10; 2001];
% adjR2th = 0.6;
% vecZoom = 2;
%
% parameters for reconstruction of Septin data
% DataSet = 'Septin1';
% Ang = [155;139;123;107;92;76;60;44;28;12;176;160;144;128;112;97;81;65;49;33;17;1];
```

```
% ReconPara = [0.075; 20; 201];
% adjR2th = 0.4;
% vecZoom = 2;
%
% parameters for reconstruction of Septin data
% DataSet = 'Septin2';
% Ang = [79;68;57;47;36;25;15;4;173;163;152];
% ReconPara = [0.075; 10; 201];
% adjR2th = 0.6;
% vecZoom = 3;
%
% parameters for reconstruction of Neuronal Spine data
DataSet = 'Spine1';
Ang = [0;18;36;54;72;90;108;126;144;162];
ReconPara = [0.05;10;351];
adjR2th = 0.4;
vecZoom = 3;
%
% parameters for reconstruction of Neuronal Spine data
% DataSet = 'Spine2';
% Ang = [0;18;36;54;72;90;108;126;144;162];
% ReconPara = [0.075;10;251];
% adjR2th = 0.4;
% vecZoom = 3;
%% Change Working Directory and Read Data
disp( ['Start Processing Dataset: ', DataSet])
disp( 'Reading Data ...')
```

```
% Change Working Directory
s = what;
curDir = [s.path, '/'];
cd( curDir);
addpath('./Util/');
% Read and Display Image Data
dataDir = strrep(fullfile(curDir, '../Data/', DataSet, '/'), '\', '/');
wfDir = [dataDir, 'WideField/'];
psfDir = [dataDir, 'PSF/'];
info = dir( wfDir);
for kk = 3 : length( info)
    img(:,:,kk-2) = imread( [wfDir, info(kk).name]);
end
img = double(img);
imgShow = sum( img, 3);
figure(1)
imshow( imgShow, [], 'InitialMagnification','fit');
title('Wide Field fluorescent image');
% Read and Display PSF data
info = dir( psfDir);
psf = imread( [psfDir, info(3).name]);
psf = double(psf);
psf = psf / sum(psf(:));
figure(2)
imshow( psf, [], 'InitialMagnification','fit');
title( 'Point Spread Funtion of the System');
%% Orientation Mapping of conventional wide field images
```

```
disp( 'Orientation Mapping of conventional wide field images ...')
% A cropped image of small area is recommended for orientation mapping
% imgFit = img(RectArea(3):RectArea(4), RectArea(1):RectArea(2), :);
imgFit = img;
% Create directory to store OM-WideField data
omWfDir = [dataDir, 'OM_WideField/'];
mkdir( omWfDir)
% OM-WideField calculation
[A, B, phy, datamat, fitmat] = omCal( imgFit, Ang);
% calculate normalized RMSE
for kk = 1 : size( datamat, 3)
    Arep(:,:,kk) = A;
    Brep(:,:,kk) = B;
end
normFit = (fitmat - Brep)./Arep; normFit( Arep==0) = 0;
normData = (datamat - Brep)./Arep; normData( Arep==0) = 0;
% normRMSE = sqrt( sum((normData-normFit).^2,3) / size( datamat,3));
normTV = sum( normData.^2, 3);
normEV = sum((normData-normFit).^2,3);
adjR2 = 1-normEV./normTV; adjR2(normTV==0) = 0;
mask = adjR2>adjR2th;
% mask = normRMSE<RMSEth;
% Display results
[x,y] = meshgrid( 1:size(datamat,2), 1:size(datamat, 1));
figure(3)
hold off
imshow( sum(imgFit,3), [], 'InitialMagnification','fit')
```

```
colormap('Hot')
hold on
OUF = A ./ B; OUF(OUF>1) = 1; OUF(mask==0) = 0;
maxOUF = max(OUF(:));
v1 = OUF.*cos(phy/180*pi); v1(mask==0) = 0;
u1 = OUF.*(sin(phy/180*pi)); u1(mask==0) = 0;
quiver(x,y,v1,u1,vecZoom*maxOUF, 'color', 'b', 'LineStyle', '-');
v2 = OUF.*cos((phy+180)/180*pi); v2(mask==0) = 0;
u2 = OUF.*(sin((phy+180)/180*pi)); u2(mask==0) = 0;
quiver(x,y,v2,u2,vecZoom*maxOUF, 'color', 'b', 'LineStyle', '-');
% save data
print( 3, '-dtiff', '-r800', [omWfDir, 'OM-WF.tif']);
imwrite( OUF, [omWfDir, 'OUF-WF.tif']);
save([omWfDir, 'OM-WF_check.mat'], 'A', 'B', 'Ang', 'datamat', 'fitmat', 'phy', 'OUF', 'u1', 'u2', 'v1', 'v2', 'adjR2');
%% super resolution reconstrution using OM-SPoD
% save data and parameters to run python reconstruction program
tmpDir = [dataDir, 'tmp/'];
mkdir( tmpDir)
data.ReconPara = ReconPara;
data.image = imgFit;
data.psf = psf;
save( [tmpDir, 'ReconData.mat'], 'data');
% run reconstrution
disp( 'Reconstructing super-resolved images ...')
omSpodDir = [dataDir, 'OM_SPoD/'];
mkdir( omSpodDir)
```

```
command = ['python ', 'OM_SPoD.py ', dataDir];
[status, cmdout] = system( command);
%
load( [tmpDir, 'ReconResult.mat']);
rmdir( tmpDir, 's');
img = data;
imgSave = sum( img, 3);
imgSave = uint16( imgSave / max(imgSave(:)) * 65535) ;
imwrite( imgSave, [omSpodDir, 'SR_SPoD.tif'])
%% Orientation Mapping of OM-SPoD images
disp( 'Orientation Mapping of OM-SPoD images ...')
% OM-WideField calculation
[A, B, phy, datamat, fitmat] = omCal( img, Ang);
% calculate normalized RMSE
for kk = 1 : size( datamat, 3)
    Arep(:,:,kk) = A;
    Brep(:,:,kk) = B;
end
normFit = (fitmat - Brep)./Arep; normFit( Arep==0) = 0;
normData = (datamat - Brep)./Arep; normData( Arep==0) = 0;
normTV = sum( normData.^2, 3);
normEV = sum((normData-normFit).^2,3);
adjR2 = 1-normEV./normTV; adjR2(normTV==0) = 0;
mask = adjR2>adjR2th;
% Display results
[x,y] = meshgrid( 1:size(datamat,2), 1:size(datamat, 1));
figure(4)
```

```
hold off
imshow( sum(img,3), [], 'InitialMagnification','fit')
colormap('Hot')
hold on
OUF = A ./ B; OUF(OUF>1) = 1; OUF(mask==0) = 0;
maxOUF = max(OUF(:));
v1 = OUF.*cos(phy/180*pi); v1(mask==0) = 0;
u1 = OUF.*(sin(phy/180*pi)); u1(mask==0) = 0;
quiver(x,y,v1,u1,maxOUF, 'color', 'b', 'LineStyle', '-');
v2 = OUF.*cos((phy+180)/180*pi); v2(mask==0) = 0;
u2 = OUF.*(sin((phy+180)/180*pi)); u2(mask==0) = 0;
quiver(x,y,v2,u2,maxOUF, 'color', 'b', 'LineStyle', '-');
% save data
print( 4, '-dtiff', '-r800', [omSpodDir, 'OM-SPoD.tif']);
imwrite( OUF, [omSpodDir, 'OUF-SPoD.tif']);
save([omSpodDir, 'OM-SPoD_check.mat'], 'A', 'B', 'Ang', 'datamat', 'fitmat', 'phy', 'OUF', 'u1', 'u2', 'v1', 'v2', 'adjR2');
```

REFERENCES

[1] Chen, S. Y. & Van Der Meer, B. W. Theory of two-photon induced fluorescence anisotropy decay in membranes. *Biophys J* **64**, 1567-1575, 1993.

[2] Callis, P. R. in *Topics in Fluorescence Spectroscopy: Volume 5: Nonlinear and Two-Photon-Induced Fluorescence* (ed Joseph R. Lakowicz) 1-42 (Springer US, 2002).

[3] Valades Cruz, C. A., Shaban, H. A., Kress, A. *et al.* Quantitative nanoscale imaging of orientational order in biological filaments by polarized superresolution microscopy. *Proceedings of the National Academy of Sciences* **113**, E820-E828, 2016.

[4] Ferrand, P., Gasecka, P., Kress, A. *et al.* Ultimate Use of Two-Photon Fluorescence Microscopy to Map Orientational Behavior of Fluorophores. *Biophysical Journal* **106**, 2330-2339, 2014.

[5] Lazar, J., Bondar, A., Timr, S. & Firestein, S. J. Two-photon polarization microscopy reveals protein structure and function. *Nat Meth* **8**, 684-690, 2011.

[6] Inoué, S., Shimomura, O., Goda, M., Shribak, M. & Tran, P. T. Fluorescence polarization of green fluorescence protein. *Proceedings of the National Academy of Sciences* **99**, 4272-4277, 2002.

[7] Kusba, J. & Lakowicz, J. R. Definition and properties of the emission anisotropy in the absence of cylindrical symmetry of the emission field: Application to the light quenching experiments. *Journal of Chemical Physics* **111**, 89-99, 1999.

[8] Lakowicz, J. R. in *Principles of Fluorescence Spectroscopy* 291-319 (Springer US, 1999).

[9] Jasny, J. & Sepiol, J. Single molecules observed by immersion mirror objective. A novel method of finding the orientation of a radiating dipole. *Chemical Physics Letters* **273**, 439-443, 1997.

[10] Bartko, A. P. & Dickson, R. M. Imaging three-dimensional single molecule orientations. *Journal of Physical Chemistry B* **103**, 11237-11241, 1999.

[11] Bohmer, M. & Enderlein, J. Orientation imaging of single molecules by wide-field epifluorescence microscopy. *Journal of the Optical Society of America B-Optical Physics* **20**, 554-559, 2003.

[12] Patra, D., Gregor, I. & Enderlein, J. Image analysis of defocused single-molecule images for three-dimensional molecule orientation studies. *Journal of Physical Chemistry A* **108**, 6836-6841, 2004.

[13] Toprak, E., Enderlein, J., Syed, S. *et al.* Defocused orientation and position imaging (DOPI) of myosin V. *Proceedings of the National Academy of Sciences* **103**, 6495-6499, 2006.

[14] Kinosita, K., Jr., Itoh, H., Ishiwata, S. *et al.* Dual-view microscopy with a single camera: real-time imaging of molecular orientations and calcium. *J Cell Biol* **115**, 67-73, 1991.

[15] Forkey, J. N., Quinlan, M. E. & Goldman, Y. E. Protein structural dynamics by single-molecule fluorescence polarization. *Prog Biophys Mol Biol* **74**, 1-35, 2000.

[16] Weber, G. Polarization of the fluorescence of macromolecules. I. Theory and experimental method. *Biochem J* **51**, 145-155, 1952.

[17] Axelrod, D. Carbocyanine dye orientation in red cell membrane studied by microscopic fluorescence polarization. *Biophys J* **26**, 557-573, 1979.

[18] Forkey, J. N., Quinlan, M. E., Shaw, M. A., Corrie, J. E. & Goldman, Y. E. Three-dimensional structural dynamics of myosin V by single-molecule fluorescence polarization. *Nature* **422**, 399-404, 2003.

[19] Fooksman, D. R., Edidin, M. & Barisas, B. G. Measuring rotational diffusion of MHC class I on live cells by polarized FPR. *Biophys Chem* **130**, 10-16, 2007.

[20] Ohmachi, M., Komori, Y., Iwane, A. H. *et al.* Fluorescence microscopy for simultaneous observation of 3D orientation and movement and its application to quantum rod-tagged myosin V. *Proc Natl Acad Sci U S A* **109**, 5294-5298, 2012.

[21] Mehta, S. B., McQuilken, M., La Riviere, P. J. *et al.* Dissection of molecular assembly dynamics by tracking orientation and position of single molecules in live cells. *Proceedings of the National Academy of Sciences* **113**, E6352-E6361, 2016.

[22] Oldenbourg, R. & Mei, G. New polarized light microscope with precision universal compensator. *Journal of Microscopy* **180**, 140-147, 1995.

[23] Oldenbourg, R. A new view on polarization microscopy. *Nature* **381**, 811-812, 1996.

[24] Adachi, K., Yasuda, R., Noji, H. *et al.* Stepping rotation of F-1-ATPase visualized through angle-resolved single-fluorophore imaging. *Proceedings of the National Academy of Sciences of the United States of America* **97**, 7243-7247, 2000.

[25] Schutz, G. J., Schindler, H. & Schmidt, T. Imaging single-molecule dichroism. *Optics Letters* **22**, 651-653, 1997.

[26] Sosa, H., Peterman, E. J. G., Moerner, W. E. & Goldstein, L. S. B. ADP-induced rocking of the kinesin motor domain revealed by single-molecule fluorescence polarization microscopy. *Nature Structural Biology* **8**, 540-544, 2001.

[27] Vrabioiu, A. M. & Mitchison, T. J. Structural insights into yeast septin organization from polarized fluorescence microscopy. *Nature* **443**, 466-469, 2006.

[28] Bs, D., X, B., L, H. *et al.* Septin filaments exhibit a dynamic, paired organization that is conserved from yeast to mammals., Septin filaments exhibit a dynamic, paired organization that is conserved from yeast to mammals. *The Journal of cell biology, The Journal of Cell Biology* **193, 193**, 1065, 1065-1081, 2011.

[29] DeMay, B. S., Noda, N., Gladfelter, A. S. & Oldenbourg, R. Rapid and quantitative imaging of excitation polarized fluorescence reveals ordered septin dynamics in live yeast. *Biophys J* **101**, 985-994, 2011.

[30] Abrahamsson, S., McQuilken, M., Mehta, S. B. *et al.* MultiFocus Polarization Microscope (MF-PolScope) for 3D polarization imaging of up to 25 focal planes simultaneously. *Opt Express* **23**, 7734-7754, 2015.

[31] Hafi, N., Grunwald, M., van den Heuvel, L. S. *et al.* Fluorescence nanoscopy by polarization modulation and polarization angle narrowing. *Nature Methods* **11**, 579-584, 2014.

[32] Benninger, R. K. P., Onfelt, B., Neil, M. A. A., Davis, D. M. & French, P. M. W. Fluorescence imaging of two-photon linear dichroism: Cholesterol depletion disrupts molecular orientation in cell membranes. *Biophysical Journal* **88**, 609-622, 2005.

[33] Gasecka, A., Han, T. J., Favard, C., Cho, B. R. & Brasselet, S. Quantitative Imaging of Molecular Order in Lipid Membranes Using Two-Photon Fluorescence Polarimetry. *Biophysical Journal* **97**, 2854-2862, 2009.

[34] Wang, X., Kress, A., Brasselet, S. & Ferrand, P. High frame-rate fluorescence confocal angle-resolved linear dichroism microscopy. *Rev Sci Instrum* **84**, 053708, 2013.

[35] Kress, A., Wang, X., Ranchon, H. *et al.* Mapping the Local Organization of Cell Membranes Using Excitation-Polarization-Resolved Confocal Fluorescence Microscopy. *Biophysical Journal* **105**, 127-136, 2013.

[36] Nishizaka, T., Oiwa, K., Noji, H. *et al.* Chemomechanical coupling in F1-ATPase revealed by simultaneous observation of nucleotide kinetics and rotation. *Nat Struct Mol Biol* **11**, 142-148, 2004.

[37] Sun, Y., Schroeder, H. W., 3rd, Beausang, J. F. *et al.* Myosin VI walks "wiggly" on actin with large and variable tilting. *Mol Cell* **28**, 954-964, 2007.

[38] Sun, Y., Sato, O., Ruhnow, F. *et al.* Single-molecule stepping and structural dynamics of myosin X. *Nat Struct Mol Biol* **17**, 485-491, 2010.

[39] Velez, M. & Axelrod, D. Polarized fluorescence photobleaching recovery for measuring rotational diffusion in solutions and membranes. *Biophys J* **53**, 575-591, 1988.

[40] Abbe, E. Beiträge zur theorie des mikroskopsageund der mikroskopischen Wahrnehmung. *Archiv fur Mikroskopische Anatomie*, 413-418, 1873.

[41] Moerner, W. E. & Kador, L. Optical detection and spectroscopy of single molecules in a solid. *Phys Rev Lett* **62**, 2535-2538, 1989.

[42] Hell, S. & Stelzer, E. H. K. Properties of a 4pi Confocal Fluorescence Microscope. *Journal of the Optical Society of America a-Optics Image Science and Vision* **9**, 2159-2166, 1992.

[43] Cogswell, C. J. Sevenfold improvement of axial resolution in 3D wide-field microscopy using two objective-lenses. *Proceedings of SPIE - The International Society for Optical Engineering* **2412**, 147-156, 1995.

[44] Hell, S. W. & Wichmann, J. Breaking the diffraction resolution limit by stimulated emission: stimulated-emission-depletion fluorescence microscopy. *Opt Lett* **19**, 780-782, 1994.

[45] Klar, T. A., Jakobs, S., Dyba, M., Egner, A. & Hell, S. W. Fluorescence microscopy with diffraction resolution barrier broken by stimulated emission. *Proc Natl Acad Sci U S A* **97**, 8206-8210, 2000.

[46] Betzig, E. Proposed method for molecular optical imaging. *Opt Lett* **20**, 237-239, 1995.

[47] Betzig, E., Patterson, G. H., Sougrat, R. *et al.* Imaging intracellular fluorescent proteins at nanometer resolution. *Science* **313**, 1642-1645, 2006.

[48] Rust, M. J., Bates, M. & Zhuang, X. W. Sub-diffraction-limit imaging by stochastic optical reconstruction microscopy (STORM). *Nature Methods* **3**, 793-795, 2006.

[49] van de Linde, S., Loschberger, A., Klein, T. *et al.* Direct stochastic optical reconstruction microscopy with standard fluorescent probes. *Nat Protoc* **6**, 991-1009, 2011.

[50] Deschout, H., Cella Zanacchi, F., Mlodzianoski, M. *et al.* Precisely and accurately localizing single emitters in fluorescence microscopy. *Nat Methods* **11**, 253-266, 2014.

[51] Backlund, M. P., Lew, M. D., Backer, A. S. *et al.* Simultaneous, accurate measurement of the 3D position and orientation of single molecules. *Proc Natl Acad Sci U S A* **109**, 19087-19092, 2012.

[52] Shroff, H., Galbraith, C. G., Galbraith, J. A. & Betzig, E. Live-cell photoactivated localization microscopy of nanoscale adhesion dynamics. *Nature Methods* **5**, 417-423, 2008.

[53] Holden, S. J., Uphoff, S. & Kapanidis, A. N. DAOSTORM: an algorithm for high- density super-resolution microscopy. *Nat Methods* **8**, 279-280, 2011.

[54] Quan, T. W., Zhu, H. Y., Liu, X. M. *et al.* High-density localization of active molecules using Structured Sparse Model and Bayesian Information Criterion. *Optics Express* **19**, 16963-16974, 2011.

[55] Huang, H.-C., Chang, B.-J., Chou, L.-J. & Chiang, S.-Y. Three-beam interference with circular polarization for structured illumination microscopy. *Optics Express* **21**, 23963-23977, 2013.

[56] Dertinger, T., Colyer, R., Iyer, G., Weiss, S. & Enderlein, J. Fast, background-free, 3D super-resolution optical fluctuation imaging (SOFI). *Proc Natl Acad Sci U S A* **106**, 22287-22292, 2009.

[57] Cox, S., Rosten, E., Monypenny, J. *et al.* Bayesian localization microscopy reveals nanoscale podosome dynamics. *Nature Methods* **9**, 195-200, 2012.

[58] Leutenegger, M., Eggeling, C. & Hell, S. W. Analytical description of STED microscopy performance. *Opt Express* **18**, 26417-26429, 2010.

[59] Chmyrov, A., Keller, J., Grotjohann, T. *et al.* Nanoscopy with more than 100,000 'doughnuts'. *Nature Methods* **10**, 737-+, 2013.

[60] Schneider, J., Zahn, J., Maglione, M. *et al.* Ultrafast, temporally stochastic STED nanoscopy of millisecond dynamics. *Nature Methods* **12**, 827-+, 2015.

[61] Rittweger, E., Han, K. Y., Irvine, S. E., Eggeling, C. & Hell, S. W. STED microscopy reveals crystal colour centres with nanometric resolution. *Nature Photonics* **3**, 144-147, 2009.

[62] Westphal, V., Rizzoli, S. O., Lauterbach, M. A. *et al.* Video-rate far-field optical nanoscopy dissects synaptic vesicle movement. *Science* **320**, 246-249, 2008.

[63] Hein, B., Willig, K. I. & Hell, S. W. Stimulated emission depletion (STED) nanoscopy of a fluorescent protein-labeled organelle inside a living cell. *Proceedings of the National Academy of Sciences of the United States of America* **105**, 14271-14276, 2008.

[64] Willig, K. I., Kellner, R. R., Medda, R. *et al.* Nanoscale resolution in GFP-based microscopy. *Nature Methods* **3**, 721-723, 2006.

[65] Willig, K. I., Harke, B., Medda, R. & Hell, S. W. STED microscopy with continuous wave beams. *Nat Methods* **4**, 915-918, 2007.

[66] Moneron, G., Medda, R., Hein, B. *et al.* Fast STED microscopy with continuous wave fiber lasers. *Opt Express* **18**, 1302-1309, 2010.

[67] Gustafsson, M. G. L. Surpassing the lateral resolution limit by a factor of two using structured illumination microscopy. *Journal of Microscopy-Oxford* **198**, 82-87, 2000.

[68] Gustafsson, M. G. Nonlinear structured-illumination microscopy: wide-field fluorescence imaging with theoretically unlimited resolution. *Proc Natl Acad Sci U S A* **102**, 13081-13086, 2005.

[69] Gur, A., Zalevsky, Z., Mico, V., Garcia, J. & Fixler, D. The limitations of nonlinear fluorescence effect in super resolution saturated structured illumination microscopy system. *J Fluoresc* **21**, 1075-1082, 2011.

[70] Nixon-Abell, J., Obara, C. J., Weigel, A. V. *et al.* Increased spatiotemporal resolution reveals highly dynamic dense tubular matrices in the peripheral ER. *Science* **354**, 2016.

[71] Li, D., Shao, L., Chen, B. C. *et al.* ADVANCED IMAGING. Extended-resolution structured illumination imaging of endocytic and cytoskeletal dynamics. *Science* **349**, aab3500, 2015.

[72] Zhanghao, K., Chen, L., Yang, X.-S. *et al.* Super-resolution dipole orientation mapping via polarization demodulation. *Light: Science & Applications* **5**, e16166, 2016.

[73] Hafi, N., Grunwald, M., van den Heuvel, L. S. *et al.* Reply to “Polarization modulation adds little additional information to super-resolution fluorescence microscopy”. *Nature Methods* **13**, 8-9, 2016.

[74] Mostowy, S. & Cossart, P. Septins: the fourth component of the cytoskeleton. *Nat Rev Mol Cell Biol* **13**, 183-194, 2012.

[75] Kampmann, M., Atkinson, C. E., Mattheyses, A. L. & Simon, S. M. Mapping the orientation of nuclear pore proteins in living cells with polarized fluorescence microscopy. *Nat Struct Mol Biol* **18**, 643-649, 2011.

[76] Frahm, L. & Keller, J. Polarization modulation adds little additional information to super-resolution fluorescence microscopy. *Nature Methods* **13**, 7-8, 2016.

[77] Marriott, G., Mao, S., Sakata, T. *et al.* Optical lock-in detection imaging microscopy for contrast-enhanced imaging in living cells. *Proceedings of the National Academy of Sciences* **105**, 17789-17794, 2008.

[78] Hafi, N., Grunwald, M., van den Heuvel, L. S. *et al.* Reply to "Polarization modulation adds little additional information to super-resolution fluorescence microscopy". *Nature Methods* **13**, 8-9, 2016.

[79] Geissbuehler, S., Sharipov, A., Godinat, A. *et al.* Live-cell multiplane three-dimensional super-resolution optical fluctuation imaging. *Nature Communications* **5**, 5830, 2014.

[80] Adelson, E. H. & Bergen, J. R. *Tertiary The plenoptic function and the elements of early vision* 3-20.

[81] Levoy, M. & Hanrahan, P. in *Proceedings of the 23rd annual conference on Computer graphics and interactive techniques* 31-42 ACM, 1996.

[82] Broxton, M., Grosenick, L., Yang, S. *et al.* Wave optics theory and 3-D deconvolution for the light field microscope. *Optics Express* **21**, 25418, 2013.

[83] Lee, B. & Kim, J. *Tertiary Real-time 3D capturing-visualization conversion for light field microscopy* 876908-876908-876906.

[84] Zheng, G., Horstmeyer, R. & Yang, C. Wide-field, high-resolution Fourier ptychographic microscopy. *Nature Photonics* **7**, 739-745, 2013.

[85] Shroff, S. A. & Berkner, K. Image formation analysis and high resolution image reconstruction for plenoptic imaging systems. *Applied Optics* **52**, D22, 2013.

[86] Orth, A. & Crozier, K. Microscopy with microlens arrays: high throughput, high resolution and light-field imaging. *Optics Express* **20**, 13522, 2012.

[87] Bishop, T. E. & Favaro, P. The Light Field Camera: Extended Depth of Field, Aliasing, and Superresolution. *IEEE Transactions on Pattern Analysis and Machine Intelligence* **34**, 972-986, 2012.

[88] Wang, Y., Ji, X. & Dai, Q. Key technologies of light field capture for 3D reconstruction in microscopic scene. *Science China Information Sciences* **53**, 1917-1930, 2010.

[89] Billy, M. L., Chen, B., Vaish, V., Horowitz, M. & Bolas, M. Synthetic Aperture Confocal Imaging. *ACM Trans. Graph* **23**, 825–834, 2004.

[90] Ng, R. *Tertiary Fourier slice photography* 735–744 (ACM).

[91] Levoy, M., Zhang, Z. & McDowall, I. Recording and controlling the 4D light field in a microscope using microlens arrays. *Journal of Microscopy* **235**, 144–162, 2009.

[92] Cohen, N., Yang, S., Andalman, A. *et al.* Enhancing the performance of the light field microscope using wavefront coding. *Optics Express* **22**, 24817, 2014.

[93] Prevedel, R., Yoon, Y.-G., Hoffmann, M. *et al.* Simultaneous whole-animal 3D imaging of neuronal activity using light-field microscopy. *Nature Methods* **11**, 727-730, 2014.

[94] Kim, J., Jung, J.-H., Jeong, Y., Hong, K. & Lee, B. Real-time integral imaging system for light field microscopy. *Optics Express* **22**, 10210-10220, 2014.

[95] Kwon, K.-C., Jeong, J.-S., Erdenebat, M.-U. *et al.* Resolution-enhancement for an orthographic-view image display in an integral imaging microscope system. *Biomedical Optics Express* **6**, 736, 2015.

[96] Tian, L. & Waller, L. 3D intensity and phase imaging from light field measurements in an LED array microscope. *Optica* **2**, 104, 2015.

[97] Orth, A. & Crozier, K. B. Light field moment imaging. *Optics Letters* **38**, 2666, 2013.

[98] Marc Levoy, R. N. Light field microscopy. *ACM Trans. Graph.* **25**, 924-934, 2006.

[99] Krieger, J. W., Singh, A. P., Bag, N. *et al.* Imaging fluorescence (cross-) correlation spectroscopy in live cells and organisms. *Nature Protocols* **10**, 1948-1974, 2015.

[100] Schwille, P., Haupts, U., Maiti, S. & Webb, W. W. Molecular dynamics in living cells observed by fluorescence correlation spectroscopy with one- and two-photon excitation. **77**, 2251-2265, 1999.

[101] Eggeling, C., Ringemann, C., Medda, R. *et al.* Direct observation of the nanoscale dynamics of membrane lipids in a living cell. *Nature* **457**, 1159-1162, 2009.

[102] Kang, M., Day, C. A., Kenworthy, A. K. & DiBenedetto, E. Simplified equation to extract diffusion coefficients from confocal FRAP data. *Traffic* **13**, 1589-1600, 2012.

[103] Ong, K., Wloka, C., Okada, S., Svitkina, T. & Bi, E. Architecture and dynamic remodelling of the septin cytoskeleton during the cell cycle. *Nat Commun* **5**, 5698, 2014.

[104] Sabbert, D., Engelbrecht, S. & Junge, W. Intersubunit rotation in active F-ATPase. *Nature* **381**, 623-625, 1996.

[105] Lesoine, J. F., Lee, J. Y., Krogmeier, J. R. *et al.* Quantitative scheme for full-field polarization rotating fluorescence microscopy using a liquid crystal variable retarder. *Review of Scientific Instruments* **83**, 053705, 2012.

[106] Betzig, E. & Chichester, R. J. Single Molecules Observed by near-Field Scanning Optical Microscopy (Nsom). *Biophysical Journal* **66**, A277-A277, 1994.

[107] Irving, M., St Claire Allen, T., Sabido-David, C. *et al.* Tilting of the light-chain region of myosin during step length changes and active force generation in skeletal muscle. *Nature* **375**, 688-691, 1995.

[108] Sase, I., Miyata, H., Ishiwata, S. & Kinosita, K. Axial rotation of sliding actin filaments revealed by single-fluorophore imaging. *Proceedings of the National Academy of Sciences of the United States of America* **94**, 5646-5650, 1997.

[109] Sabido-David, C., Hopkins, S. C., Saraswat, L. D. *et al.* Orientation changes of fluorescent probes at five sites on the myosin regulatory light chain during contraction of single skeletal muscle fibres. *Journal of Molecular Biology* **279**, 387-402, 1998.

[110] Warshaw, D. M., Hayes, E., Gaffney, D. *et al.* Myosin conformational states determined by single fluorophore polarization. *Proceedings of the National Academy of Sciences of the United States of America* **95**, 8034-8039, 1998.

[111] Ha, T., Enderle, T., Chemla, S., Selvin, R. & Weiss, S. Single Molecule Dynamics Studied by Polarization Modulation. *Phys Rev Lett* **77**, 3979-3982, 1996.

[112] Steinbach, G., Pomozi, I., Jánosa, D. P., Makovitzky, J. & Garab, G. Confocal Fluorescence Detected Linear Dichroism Imaging of Isolated Human Amyloid Fibrils. Role of Supercoiling. *Journal of Fluorescence* **21**, 983-989, 2011.